OBSERVATIONS OF DISINTEGRATING, EVAPORATING AND HOT PLANET ATMOSPHERES WITH TRANSMISSION SPECTRA

A Dissertation

Presented to the Faculty of the Graduate School

of Cornell University

in Partial Fulfillment of the Requirements for the Degree of

Doctor of Philosophy

by

Everett A. Schlawin

August 2015

© 2015 Everett A. Schlawin

ALL RIGHTS RESERVED

OBSERVATIONS OF DISINTEGRATING, EVAPORATING AND HOT PLANET ATMOSPHERES WITH TRANSMISSION SPECTRA

Everett A. Schlawin, Ph.D.

Cornell University 2015

Hot exoplanets with semi-major axes smaller than 0.05 AU can go considerable alteration from the high energy radiation of their host stars radiation from driving winds to altering the thermal profiles to disintegrating nearby planets. A variety of exoplanets are studied in this high irradiation environment with different consequences on their atmospheres. The escaping winds from the transiting hot Jupiter HD 209458b are measured with a novel limb brightened transit model for ultraviolet wavelengths. The hot exoplanet CoRoT-1b is used as a test case for the hypothesis that TiO and VO molecules (which can exist in equilibrium at high temperatures) can create a temperature inversion in the planet by absorbing stellar ultraviolet radiation. Finally, the escaping debris from the disintegrating planet candidate KIC 12557548b are characterized with spectroscopy to constrain the size of dust particless in its escaping winds.

BIOGRAPHICAL SKETCH

Everett grew up in West Windsor, NJ where he received an excellent math and science education from the public schools. After looking through a telescope at the cloud bands of Jupiter, he developed an interest in astronomy so he elected to study math, physics and some self-taught programming. He went to West Windsor-Plainsboro High School South, where he continued studying the sciences and ran cross country graduating in 2005. At Oberlin College, he continued running while studying physics, earning him the Norm Craig student athlete award and he earned high honors and Phi Beta Kappa membership in 2009. Everett went directly to graduate school at Cornell University, where he got bit by the "exoplanets" bug. His main research interests are the observations of exoplanets and the instrumentation needed to observe them. He spent about a third of his time doing design and fabrication work for the TripleSpec 4 spectrograph, while spending the rest of his time on transiting exoplanets under the advisor-ship of Professors Terry L. Herter and James P. Lloyd.

This document is dedicated to the author's late grandparents Jack and Gloria Dube.

ACKNOWLEDGEMENTS

The author also like to acknowledge all of detailed technical and big picture guidance from his advisor Terry Herter, witty advice from his committee member Jamie Lloyd, back-of-the-envelope astrophysics theory instruction from Dong Lai, and atmospheric dynamics introduction from his minor advisor Gang Chen. He would like to acknowledge the unabated love and encouragement from his partner in life Jung Mee Park, who also provided endless tasty snacks and meals to fuel the thesis research. Ming Zhao and Johanna Teske provided invaluable data, expertise and feedback for all of the Infrared Telescope Facility (IRTF) observations and proposal. He would also like to acknowledge the deep support from his parents Ilene Dube and Mark Schlawin from his very first look through a telescope, to sending him off to college and graduate school even when they wanted him to stay home. Chuck Henderson taught the author extensive engineering Macgyver skills and strategies from folding a band saw blade to hand-winding a fiber-glass strap. Thanks to Saul Rappaport, Kevin Covey, Eric Agol, Lucianne Walkowicz, Phil Muirhead, Barbara Rojas, Nate Ellis, Saramoria Shields, Carl Ferkinhoff, Ryan Lau, Amit Vishwas, Riccardo Pavesi for their contributions, lessons, useful feedback and discussion.

TABLE OF CONTENTS

CHAPTER 1

INTRODUCTION

1.1 Hot Jupiters

Hot Jupiters have been a big boon for exoplanet science because they enabled the early detection of planets outside the Solar System and the early detection of detailed atmospheric and orbital parameters to model and study comparatively. Our giant planets all take more than 11 years to orbit the Sun, whereas hot Jupiters are bodies with masses comparable to Jupiter and very short periods under a week, thus orbiting their host stars far closer than Mercury orbits the Sun. We adopt the definition from Winn & Fabrycky (2014) that hot Jupiters have masses, $M_p, \gtrsim 0.3 M_{\rm Jup}$, where $M_{\rm Jup}$ is Jupiter's mass and orbit their stars in less than 7 days. Since they had no precedent in the Solar System, the first hot Jupiter radial velocity discoveries (600 m/s Latham et al., 1989) and (56 m/s Mayor & Queloz, 1995) were lucky finds with velocity amplitudes far above Jupiter's 13 m/s, which was at the limit of state-of-the-art spectroscopy at the time. These discoveries, along with the first planet detected around a pulsar (Wolszczan & Frail, 1992) opened up the field of exoplanet discovery and characterization that led to the thousands-of-planets Kepler era. The large number of planets now known, combined with models of the selection effects, constrains the occurrence rates of hot Jupiters around sun-like stars to be 1.2%±0.4% (Wright et al., 2012).

Hot jupiters' proximity to their host stars makes them ideal targets for characterization in addition to being comparatively easy to discover. Beginning with the first Na I detection in HD 209458b (Charbonneau et al., 2002), atmo-

spheric constituents have been detected by their increased absorption of stellar light as compared to wavelengths where the atmosphere is relatively transparent, to be discussed in Section 1.2.1. The first phase curves obtained for HD 189733b showed that the hottest part of a planet is offset from the substellar point by advection from winds (Knutson et al., 2009). These results led the way to high precision space-based spectroscopy during the full phase curve of the hot Jupiter WASP-43b, which simultaneously revealed the water abundance to an order of magnitude (Kreidberg et al., 2014) while resolving azimuthal thermal structure as a function of altitude (Stevenson et al., 2014). Measurements of the Rossiter-Mclaughlin effect (Rossiter, 1924; McLaughlin, 1924) in hot Jupiters (e.g. Winn et al., 2009) have also revealed that hot Jupiters orbits are misaligned with the spins of their host stars, a possible explanation of which is Kozai-Lidov oscillations (Kozai, 1962; Lidov, 1962) from a stellar companion (e.g. Storch et al., 2014).

1.2 Planetary Transits as Means to Characterize Atmospheres

Transiting exoplanets have favorable alignments to Earth's line of sight so that they cross in front of their host stars. When they cross in front of their host stars and block stellar light, it is called primary transit, shown in Figure 1.1. Additionally, for most orbits, save high eccentricity, misaligned cases, transiting planets also cross behind their host stars. When they cross behind, during secondary eclipse, the star occults the light from the planet. Planetary transits and eclipses offer an opportunity not only to determine a planet's size but also the composition and structure of its atmosphere.

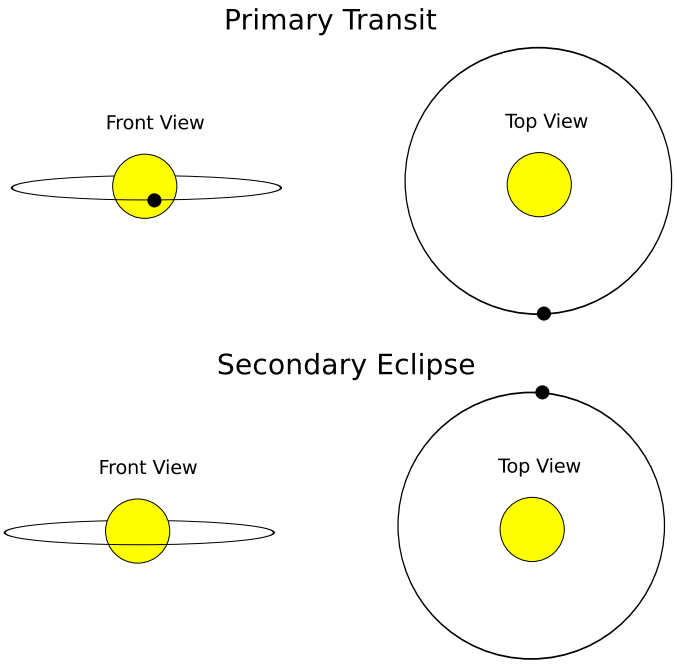

Figure 1.1: *Top:* Primary transit. When a planet crosses in front of its host star, the atmosphere absorbs and scatters light from its host star. *Bottom* During secondary eclipse, the planet's light is occulted by its host star.

1.2.1 Differential Transit Depth

Detecting the transit of a planet is relatively easy compared to detecting the atmosphere. For a uniformly illuminating star, the transit depth is the relative blockage of the planet area compared to the stellar area (as shown in Figure 1.2):

$$\delta = \frac{\pi R_p^2}{\pi R_*^2} = 1.06\% \left(\frac{R_p / R_{\rm Jup}}{R_* / R_\odot} \right)^2 \tag{1.1}$$

where δ is the transit depth, R_p is the radius of the planet, R_* is the radius of the star, $R_{\rm Jup}$ is the radius of Jupiter and $R_\odot$ is the radius of the sun (e.g. Winn, 2010). A planetary atmosphere introduces a wavelength dependence to the transit depth, but at a smaller magnitude. Consider the transit depth difference between two wavelengths, which get absorbed at different altitudes separated by

L (shown in Figure 1.2). The difference in transit depth is

$$\Delta\delta = \frac{2\pi L R_p}{\pi R_*^2} = 2\left(\frac{R_p}{R_*}\right)^2 \frac{L}{R_*} = 2\delta\frac{L}{R_p}. \tag{1.2}$$

The difference in altitudes between the two wavelengths, L, is proportional to the atmospheric scale height, which we derive from hydrostatic equilibrium and the ideal gas law. Considering a parcel of gas with an area, A and height dx, the upward pressure and downward gravitational forces will be equal in magnitude:

$$F_{\text{down}} = \rho g A dx = F_{\text{up}} = -A dP, \tag{1.3}$$

where n is the number density, A is the area of a parcel, g is the local gravitational acceleration and dP is the differential pressure from the top minus the bottom of the parcel. Assuming the fluid obeys the ideal gas law, the hydrostatic balance gives

$$\frac{dP}{dx} = \frac{d\left(\frac{\rho kT}{\mu m_a}\right)}{dx} = -\rho g, \tag{1.4}$$

where T is the kinetic gas temperature, k is Boltzmann's constant, μ is the mean molecular weight, m_a is 1 amu. If g, μ and T are all independent of altitude, then the differential equation can be solved to reveal an exponential density profile:

$$\rho(x) = \rho_0 e^{-x/H}, \tag{1.5}$$

where ρ_0 is a reference density at a reference height (x=0) and H is the atmospheric scale height,

$$H = \frac{kT}{\mu m_a g} = 280\text{km}\left(\frac{T}{2000K}\right)\left(\frac{R_p}{R_{\text{Jup}}}\right)^2 \frac{2.3}{\mu}\left(\frac{M_{\text{Jup}}}{M_p}\right). \tag{1.6}$$

When an atmosphere has an isothermal temperature profile (no dependence on temperature), it generally obeys the exponential density profile, but in most real cases an atmosphere has the temperature profile decreasing with altitude

or a temperature inversion (increasing with altitude). For typical gases in exoplanet atmospheres, the altitude variation between wavelengths that are relatively opaque and transparent is about L ≈ 5 H Burrows & Orton (2009). Plugging this into equation 1.2, the change in transit depth with wavelength across a spectrum is

$$\Delta\delta \approx 0.04\% \left(\frac{T}{2000K}\right) \frac{2.3}{\mu} \left(\frac{R_p}{R_{\rm Jup}}\right)^3 \left(\frac{M_{\rm Jup}}{M_p}\right) \left(\frac{R_\odot}{R_*}\right)^2, \tag{1.7}$$

hence photometric precisions of better than ~100 ppm are needed to characterize Jupiter-mass, Jupiter-size planets orbiting sun-like stars. Inflated hot Jupiters can have a factor of a few larger $\Delta\delta$.

The above calculation is the ideal case of a haze-free, cloud-free atmosphere. In many planets, hazes and clouds smooth out spectral features. For HD 209458b, for example, the above formula gives $\Delta\delta \approx 0.06\%$, whereas the measured water vapor features have $\Delta\delta \approx 0.025\%$, the small number being attributed to a broad haze or dust layer (Deming et al., 2013).

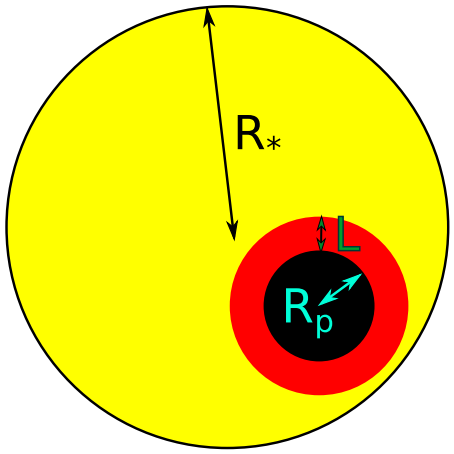

Figure 1.2: Exaggerated illustration of a planet atmosphere's scattering and absorption of star light ~ $2LR_p/R_*^2$ compared to the transit depth ~ $\left(R_p/R_*\right)^2$.

1.3 Challenges in Precision Spectroscopy

As described in section 1.2, it is desirable to achieve better than ~100 ppm precision to measure atmospheric features in the transmission spectrum of a hot Jupiter. Great care must be taken in designing an observational campaign so as to achieve that precision. Indeed, a recent compilation by Bailey (2014) shows that only 6 total exoplanets at the time had reported detections of molecular features in the transmission spectra. In this section we describe the challenges in achieving precision with a spectrograph.

1.3.1 Spectra versus Photometry

There are two approaches for measuring the presence of atmospheric features in an exoplanet: photometry, where one takes an image of the source but restricts the wavelengths with a broadband or narrowband filter, and spectroscopy, where one images the source but disperses the image as a function of wavelength with a prism or grating. These extra optics introduce issues and noise to a system, the first being slit loss described in section 1.3.3. Generally, the field of view of spectrographs is smaller than imagers, so the number of reference stars (described in Section 1.3.4) is often limited to 1, whereas an imager with a field of view of many arc minutes can have tens of reference stars for calibration (eg., 22 reference stars for a WASP-12b secondary eclipse in the *J* band Croll et al., 2011). On the other hand, spectroscopy does have a few advantages over photometry. By dispersing the image of a star over a large area, pixel-to-pixel and intra-pixel flat field considerations (described in Section 1.3.5) are usually smaller. A stellar Point Spread Function (PSF) is usually a slow func-

tion of wavelength, so one can fit the PSF with a lower order polynomial in the dispersion direction and use it to optimally sum the pixels' counts (described in section 1.3.2). Also, spectra are obtained simultaneously with the same instrument and telescope, which makes direct comparison of the transit depth at one wavelength to another much more straightforward and less susceptible to things like nonlinearity, described in Section 1.3.5.

1.3.2 Signal To Noise

As a minimum requirement for exoplanet spectroscopic observations, it is necessary to have enough photons so that counting statics (for Poisson arrivals of photons) fall below the specified noise threshold (e.g. 100 ppm). The signal to noise ratio on an individual source can be calculated as

$$\frac{S}{N} = \frac{N_{\rm sig}}{\sqrt{N_{\rm sig} + b_{\rm back} N_{\rm pix} + N_{\rm pix} R^2 N_{\rm coadds}}} \tag{1.8}$$

where $N_{\rm sig}$ is the number of photo-electrons summed in the image or images, b_ν is the background emission per pixel (including the sky, telescope and instrument), $N_{\rm pix}$ is the number of pixels extracted and R is the read noise per pixel and $N_{\rm coadds}$ is the number of coadded frames.

Optimal Extraction

With spectrographic exposures, it is necessary to sum the flux along the spatial direction to obtain the total flux for a given wavelength, as shown in Figure 1.3. One can simply add the values along all the spectral pixels,

$$S_{\rm sum} = \sum_i d_i, \tag{1.9}$$

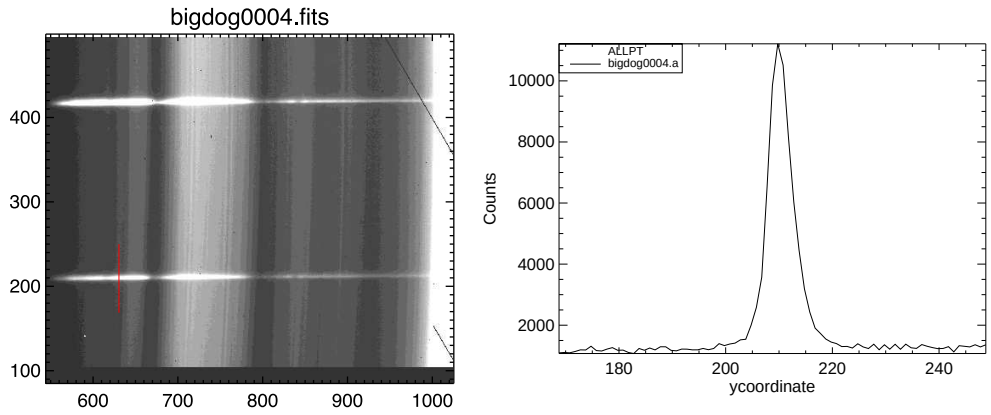

Figure 1.3: *Left* An example spectrograph image for the low resolution mode of the SpeX spectrograph on the IRTF. The spectral direction is left-right whereas the spatial direction is up-down. The red line denotes a column that is plotted. *Right* A plot of the counts in the left image as a function of Y coordinate (spatial pixel) which shows the stellar profile in this image. One can do a sum extraction or optimal extraction along this profile to get the total flux.

where S is the sum of the pixels, indexed i each having counts d_i.

However, the signal to noise is maximized if one weights the individual pixels by a weighting function A_i (Horne, 1986),

$$S_{\rm opt} = \sum_i A_i d_i = \frac{\sum_i d_i P_i/\sigma_i}{\sum_i P_i^2/\sigma_i^2}. \tag{1.10}$$

where P_i is the true stellar profile and σ_i are the true uncertainties in the stellar profile. Practically, one can estimate P_i by fitting lower order polynomial to the profile along the spectral direction since the PSF is a slow function of wavelength and the uncertainty, σ_i, can be estimated from Equation 1.8. This technique allows for very robust extraction of the spectrum and automated handling of bad pixels. However, it provides no insight or corrections into removal of the background or spectrally correlated noise effects.

1.3.3 Slit Loss

Most spectrographs include a physical slit, which allows an astronomical source's light through it, but blocks light from the surrounding field from entering the dispersing elements of the spectrograph. The slit serves two purposes this way: (1) to reduce the amount of background emission and increase the signal to noise (c.f. Equation 1.8) and (2) to keep other sources from overlapping the target source if they are aligned along the dispersion direction. The tradeoff for the improvement in signal to noise, however, is that some light from astronomical sources does not make it down the slit. Figure 1.4 shows two example slits with both a target and reference star on each slit. The wider the slit, the larger the fraction of light that the slit admits.

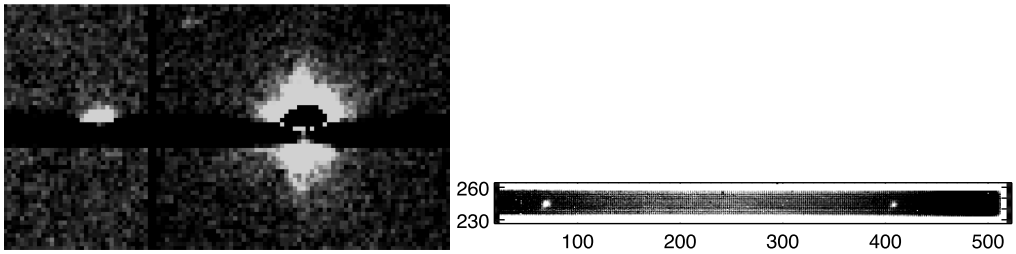

Figure 1.4: *Left* An exoplanet host star, HD 189733A with a simultaneous reference star as imaged by the slit viewer on the Palomar TripleSpec spectrograph. The light from the stars spill outside the slit (black rectangle) because it is 1×30 arcseconds and the stellar PSFs have a FWHM larger than 1 arcsecond for this night. *Right* A slit viewer image of a target (KIC 12557548) and reference star in the middle of the 3×60 arcsec slit. There is much less spillover on this wider slit, but the stars can be seen dimly from this reflective slit.

In order to calculate the slit loss quantitatively, it is useful to assume an integrated profile function for the star. We adopt a Voigt profile, which fits well the PSF as determined from the cross-dispersion profile of the IRTF SpeX data we

will be analyzing. We use the approximate (and easily integrable) Voigt function from Liu et al. (2001):

$$g(a,\sigma,y') = c_L(a)\frac{1}{\pi}\frac{\sigma_V}{y'^2+\sigma_V^2} + c_G(a)\frac{\sqrt{\ln(2)}}{\sqrt{\pi}\sigma_V}\exp\left(\frac{-\ln(2)(y'^2)}{\sigma_V^2}\right), \tag{1.11}$$

where $c_L(a)$ and $c_G(a)$ are third order polynomials,

$$c_L(d) = 0.68188 + 0.61293d - 0.18384d^2 - 0.11568d^3 \tag{1.12}$$

$$c_G(d) = 0.32460 - 0.61825d + 0.17681d^2 + 0.12109d^3 \tag{1.13}$$

where $d = (a-1)/(a+1)$, y is the vertical coordinate, a is the Voigt damping parameter and σ_V is the half width at half maximum of the Voigt function. It can be approximated as

$$\sigma_V \approx 0.5346 f_L + \sqrt{0.2166 f_L^2 + f_G^2}, \tag{1.14}$$

where $f_G = \sqrt{2\ln(2)}\sigma$ is the Gaussian half width at half maximum and $f_L = a f_G$ is the Lorentzian half width at half maximum.

This approximate Voigt profile is the same as a Gaussian profile when the Voigt damping parameter a is zero. The amount of light passing through a rectangular slit, F, for a slit half width H is

$$F(d) = \int_{-H-d}^{H-d} g(y')dy', \tag{1.15}$$

where y' is the coordinate in the star's reference frame (see Figure 1.5) and d is the displacement of the star from slit center.

This simplifies to

$$\begin{aligned} F(d) = c_L(a)\frac{1}{\pi}\left(\arctan\left(\frac{d-H}{\sigma_V}\right) - \arctan\left(\frac{d+H}{\sigma_V}\right)\right) \\ +c_G(a)\frac{1}{2}\left(\mathrm{erf}\left(\frac{\sqrt{\ln 2}(d-H)}{\sigma_V}\right) - \mathrm{erf}\left(\frac{\sqrt{\ln 2}(d+H)}{\sigma_V}\right)\right), \end{aligned} \tag{1.16}$$

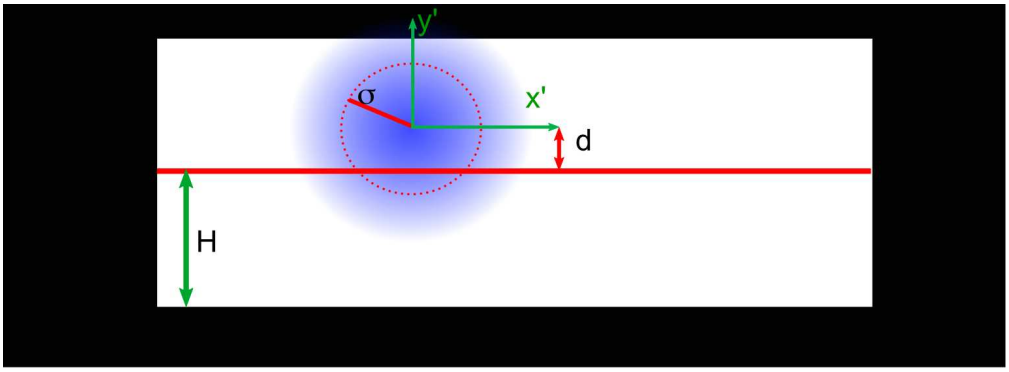

Figure 1.5: The geometry of a star with a standard deviation σ placed on a slit with half width H and displacement d from slit center.

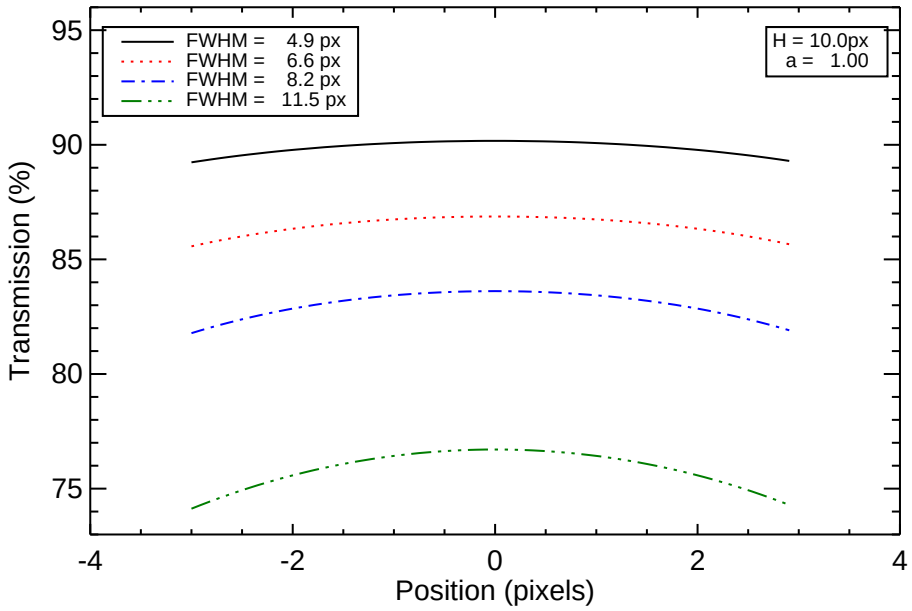

Figure 1.6: Slit loss of a star as a function of FWHM and position in the spectral direction. Here, we consider a slit that is 20 pixels wide, which is about the size for the 3 arcsecond slit in the SpeX spectrograph with the pre-2014 Aladdin InSb detector.

which is plotted in Figure 1.6.

For the nights we observed KIC 12557548, CoRoT-2 and CoRoT-1 with the

SpeX spectrograph on IRTF, the σ_V (Voigt FWHM) ranges from 0.7 arcseconds to 1.6 arcseconds (5 to 12 pixels at 0.15″/px), and guiding errors are within +/- 0.3 arc seconds (at 0.15″/px). The Voigt parameter has some correlation with σ_V, but we choose a fiducial value of $a = 1$ to show the dependency on other parameters in Figure 1.6.

Differential Slit Loss

Ground-based exoplanet observations almost always include a reference star (described in section 1.3.4) and the target star's flux is divided by the reference, so it is the differential slit loss between the two stars that is more important. Figure 1.7 shows the geometry of the setup for two stars with slit loss. In Figure 1.8, we calculate the differential slit loss for two stars separated by Δy pixels (0.15″' for the Aladdin InSb on the SpeX spectrograph) and the resulting effect of slit motions. This is assuming that the two star's PSF's are the same because they are close (within 1 arcminute on the sky) so seeing should be similar between the two sources. If the stars are displaced minimally in the slit (reducing Δy) and the slit is many times the PSF's FWHM, the differential slit losses are minimized.

1.3.4 Telluric Absorption

When observing exoplanet targets from the ground, a major concern is telluric absorption, which is light that is absorbed by Earth's atmosphere. Telluric absorption is proportional to the path length that a source goes through the Earth's atmosphere, which is quantified by the airmass,

$$z = \frac{1}{\cos\theta}, \tag{1.17}$$

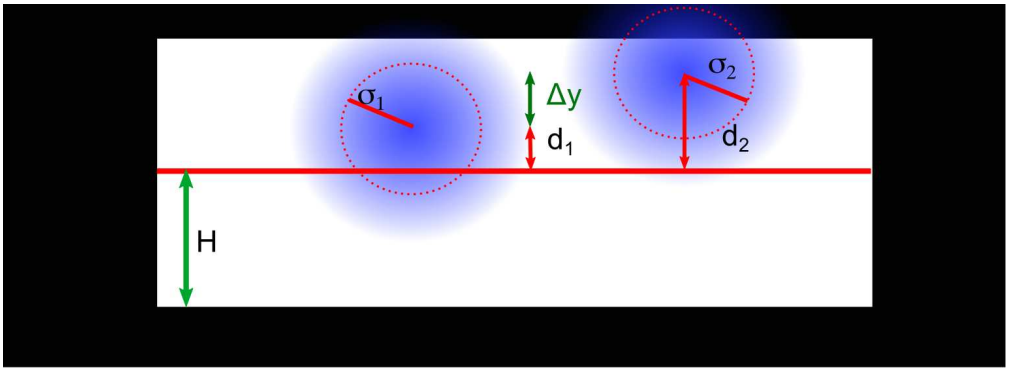

Figure 1.7: The geometry of two stars with a standard deviations σ_1 and σ_2 placed on a slit with half width H and displacements d_1 and d_2 from slit center.

where θ is the angle from zenith. In a plane parallel atmosphere (and the curvature of the Earth's atmosphere is negligible), the path length is proportional to airmass. On top of this first order estimate, however, there are variations in the amount of telluric absorption with time. Water vapor, for example, causes the majority of the absorption bands seen in the near infrared from 0.8μm to 2.4μm. The amount of water vapor changes with weather so it is unpredictable through the night. To combat these changes, ground-based exoplanet spectra campaigns use reference stars in so-called Multi-Object Spectroscopy (MOS) (e.g. Bean et al., 2010; Sing et al., 2012; Gibson et al., 2013; Bean et al., 2013). The target star spectra are divided by one or more of these reference stars to correct for the telluric absorption and also variable response of the instrument. It is preferable to have a reference star slightly brighter than the target star (when available), so that the additional counting noise (Equation 1.8) does not significantly lower the Signal-to-Noise ratio of the target divided by the reference,

$$\left(\frac{S}{N}\right)_{\text{ratio}} = \frac{1}{\sqrt{\left(\frac{N}{S}\right)^2_{\text{targ}} + \left(\frac{N}{S}\right)^2_{\text{ref}}}}, \tag{1.18}$$

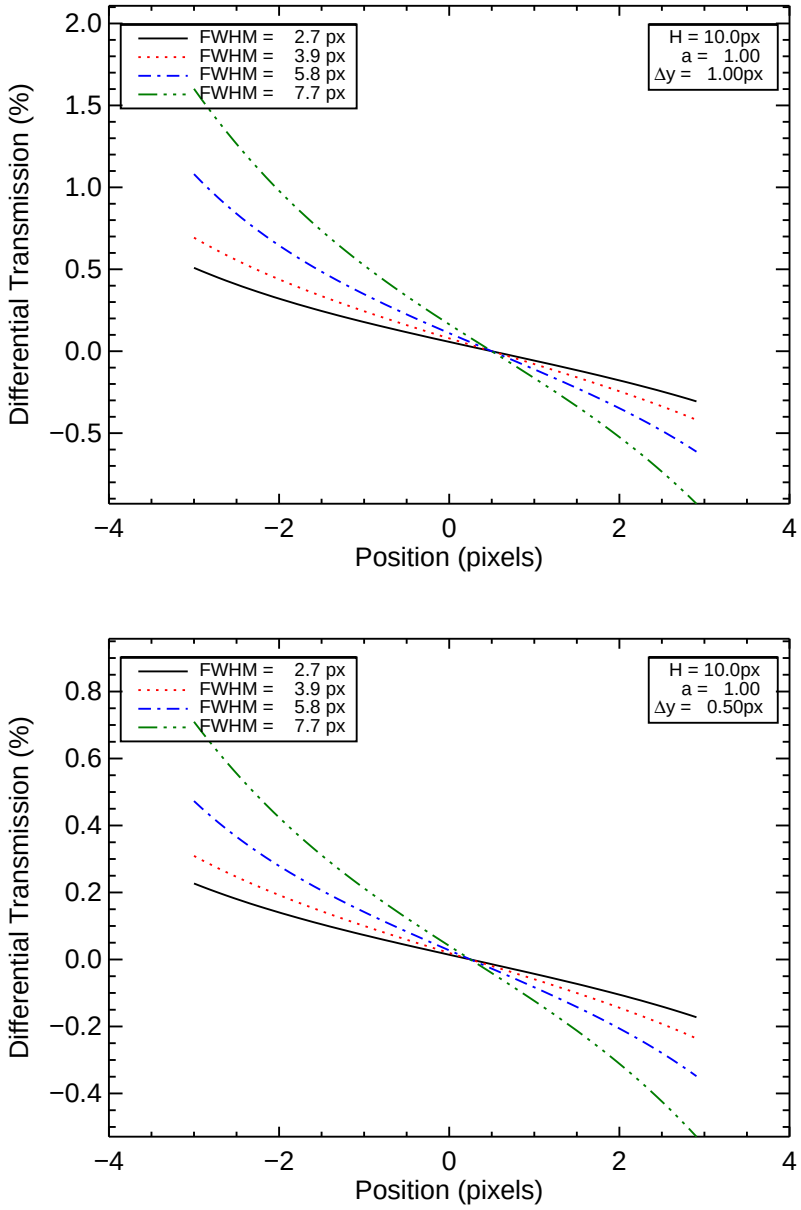

Figure 1.8: *Top* Differential slit loss as a function of target star position and FWHM for a reference star located 1 pixel away and for a slit full width of 20 pixels. *Bottom* Differential Slit Loss for a star separation of 0.5 pixels.

where $\left(\frac{N}{S}\right)_{\text{targ}}$ and $\left(\frac{N}{S}\right)_{\text{ref}}$ are the noise over signal ratios of the target star and reference star respectively.

1.3.5 Flat Fielding

An important step of any data reduction pipeline (and especially exoplanet spectra) is the flat field. The flat field accounts for the responsiveness variations across the pixels of the array. The flat field takes care of both the pixels in the detector that have different quantum efficiencies and gains while also correcting for uneven optical responsiveness of an instrument, such as out-of-focus dust particles that absorb light in some parts of the array. Generally, they are corrected together with a single flat field, but the optical responsiveness can shift around if there is flexure between the optical components that absorb light and the detector. Figure 1.9 shows the pixel versus optical flat fields for the SpeX instrument on IRTF. For observations where there the point spread function covers a small number of pixels, intra-pixel becomes important part of the flat fielding process. Spitzer photometry of secondary eclipses, for example, cannot be flat-fielded with a single frame and interpolations between pixels become important (e.g. Deming et al., 2015).

Detector Linearity

An ideal detector has a linear response so that the measured counts (Data numbers (DN)) are proportional to the input energy (flux times time) on a detector. In reality, the proportionality constant changes as a function of illumination, shown in Figure 1.10. This correction becomes especially important when trying to combine data sets from multiple observatories, which each have different non-linearities, to build up a multi-wavelength (ultraviolet to infrared) transmission or emission spectrum of a planet (e.g. Pont et al., 2013). It can also affect the precision of exoplanet observations if the source's PSF is changing or

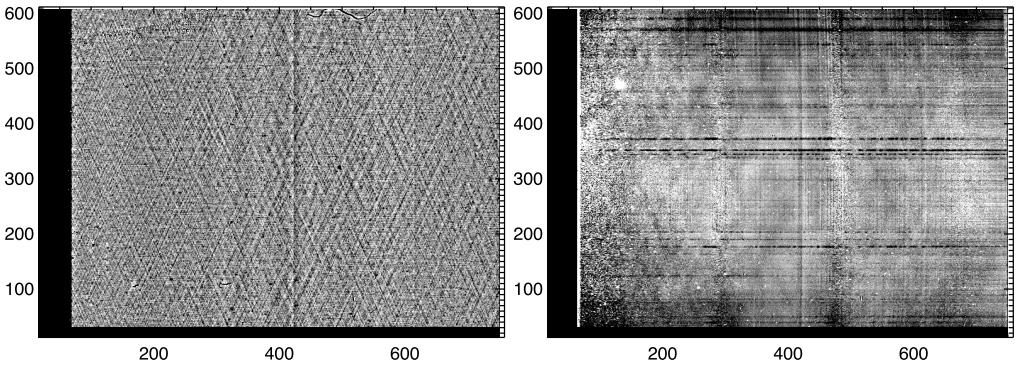

Figure 1.9: *Left* The detector response for the IRTF Hawaii-II RG detector on the SpeX spectrograph which highlights the pixel-to-pixel response variations and the patterns on the array. Broad trends are removed to show the high frequency response variations. *Right* Removing these features from a sky flat reveals the optical responsiveness variations of the instrument. The latter features can move with instrument flexure, whereas the pixel-to-pixel response stays fixed to the detector.

shifting so that the relative response of the PSF's peak versus wing is different.

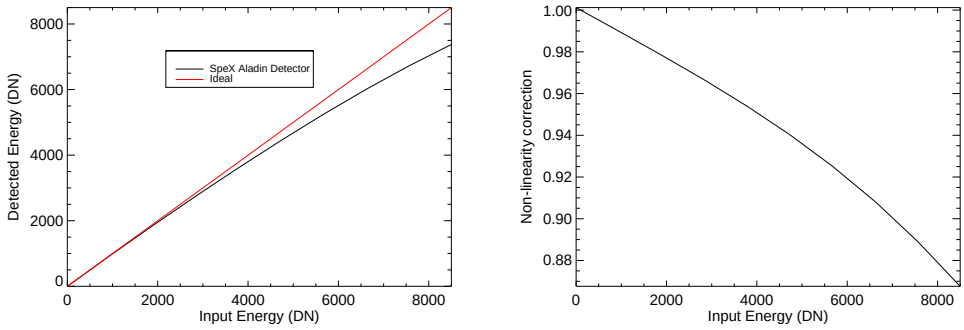

Figure 1.10: *Left* The median response of the SpeX Aladin detector as a function of illumination deviates from linear for large fractions of its full well depth. *Right* The measured detector response can be divided by a non-linearity correction, plotted here, to get an estimate of the true input flux.

1.3.6 Detector Persistence and Ramps

Detectors, and especially, near Infrared Hawaii II RG suffer from "persistence", which is when electrons become "trapped" in a detector after illumination from a bright source. The flip side of this problem, is that when you first place a source on the detector, there is a "ramp up" as the flux increases to a plateau for similar reasons. The ramp-up is often fit as an exponential (Agol et al., 2010), or the data during the ramp up is discarded (Kreidberg et al., 2014). Ramp-up is less noticeable for ground-based infrared data with large backgrounds because the source causes a smaller increase to the well depth of a detector.

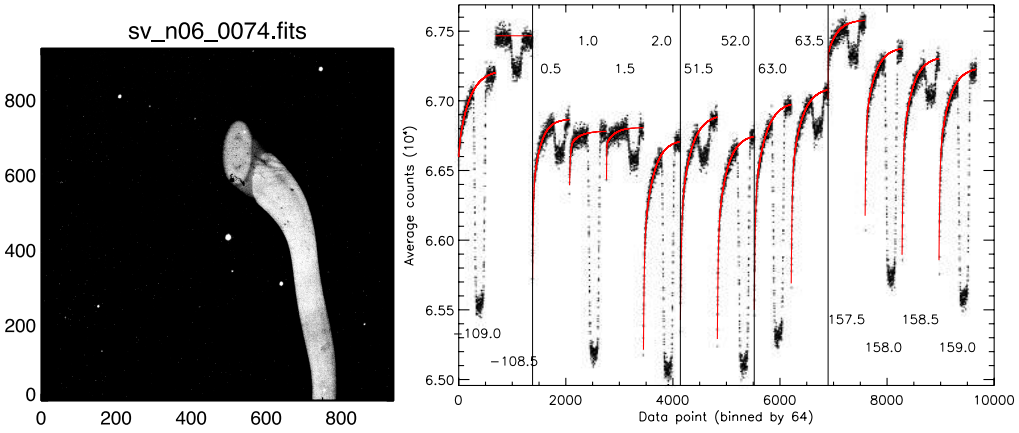

Figure 1.11: *Left* An image from the slit viewer camera of the TripleSpec 4 instrument (described in Chapter A) after a few minutes of illumination of the detector by Saturn around (550,650) and then the telescope is moved so that Saturn make as streak to the lower right. Despite the fact that Saturn did not illuminate the detector at all during this exposure, it is still visible because of detector persistence. *Right* The Spitzer detector shows ramping up as a function of time due to charge trapping (Agol et al., 2010).

1.3.7 Stellar Variability

Exoplanet host stars' fluxes vary when they emit flares and develop spots, both of which are due to magnetic activity of their host stars. The amount of variability is a strong function of wavelength. The largest variations occurs for short wavelengths, with X-Rays inducing changes of ~100% on light curves as a function of stellar rotation period (e.g. Poppenhaeger et al., 2011). The effect of stellar spots on a light curve decreases as a function of wavelength because, for a fixed temperature contrast between star spots and the surrounding photosphere, the difference in the Planck function (Rybicki & Lightman, 1986) decreases with wavelength, shown in Figure 1.12. Spots lifetimes are generally many rotation periods, which are between ~1 and ~70 days for most Kepler stars (McQuillan et al., 2014), as compared to hour-long transit durations, so the time variability of spot modulations on light curves can be greatly reduced by fitting baseline trends. Spots do affect the transit depth both by reducing the effective area of the star (enhancing transit depths) and decreasing the amount of stellar light absorbed by a planet when it crosses star spots (decreasing transit depths) (Czesla et al., 2009). To combat these effects, it is preferable to average transit measurements over many independent transit events and also to take spectra (or multiple photometric bands) simultaneously so that they are not affected by stellar activity differentially.

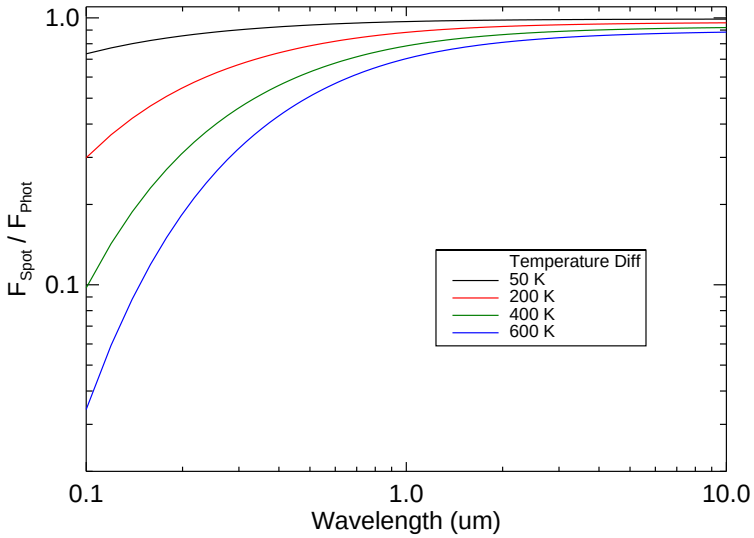

Figure 1.12: The flux ratio of a star spot to the surrounding photosphere for a given temperature difference assuming Planck emission. The drop in overall brightness by the spot will be this flux contrast times the fractional areal spot coverage.

BIBLIOGRAPHY

Agol, E., Cowan, N. B., Knutson, H. A., Deming, D., Steffen, J. H., Henry, G. W., & Charbonneau, D. 2010, ApJ, 721, 1861, 1007.4378

Bailey, J. 2014, PASA, 31, 43, 1409.6821

Bean, J. L., Désert, J.-M., Seifahrt, A., Madhusudhan, N., Chilingarian, I., Homeier, D., & Szentgyorgyi, A. 2013, ApJ, 771, 108, 1303.1094

Bean, J. L., Miller-Ricci Kempton, E., & Homeier, D. 2010, Nature , 468, 669, 1012.0331

Burrows, A., & Orton, G. 2009, ArXiv e-prints, 0910.0248

Charbonneau, D., Brown, T. M., Noyes, R. W., & Gilliland, R. L. 2002, ApJ, 568, 377, arXiv:astro-ph/0111544

Croll, B., Lafreniere, D., Albert, L., Jayawardhana, R., Fortney, J. J., & Murray, N. 2011, AJ, 141, 30, 1009.0071

Czesla, S., Huber, K. F., Wolter, U., Schröter, S., & Schmitt, J. H. M. M. 2009, A&A , 505, 1277, 0906.3604

Deming, D. et al. 2015, ApJ, 805, 132, 1411.7404

——. 2013, ApJ, 774, 95, 1302.1141

Gibson, N. P., Aigrain, S., Barstow, J. K., Evans, T. M., Fletcher, L. N., & Irwin, P. G. J. 2013, MNRAS , 428, 3680, 1210.7798

Horne, K. 1986, PASP , 98, 609

Knutson, H. A. et al. 2009, ApJ, 690, 822, 0802.1705

Kozai, Y. 1962, AJ, 67, 591

Kreidberg, L. et al. 2014, ApJ, 793, L27, 1410.2255

Latham, D. W., Stefanik, R. P., Mazeh, T., Mayor, M., & Burki, G. 1989, Nature , 339, 38

Lidov, M. L. 1962, Planet. Space Sci. , 9, 719

Liu, Y., Lin, J., Huang, G., Guo, Y., & Duan, C. 2001, Journal of the Optical Society of America B Optical Physics, 18, 666

Mayor, M., & Queloz, D. 1995, Nature , 378, 355

McLaughlin, D. B. 1924, ApJ, 60, 22

McQuillan, A., Mazeh, T., & Aigrain, S. 2014, ApJS, 211, 24, 1402.5694

Pont, F., Sing, D. K., Gibson, N. P., Aigrain, S., Henry, G., & Husnoo, N. 2013, MNRAS , 432, 2917, 1210.4163

Poppenhaeger, K., Lenz, L. F., Reiners, A., Schmitt, J. H. M. M., & Shkolnik, E. 2011, A&A , 528, A58, 1010.5632

Rossiter, R. A. 1924, ApJ, 60, 15

Rybicki, G. B., & Lightman, A. P. 1986, Radiative Processes in Astrophysics (Wiley-VCH)

Sing, D. K. et al. 2012, MNRAS , 426, 1663, 1208.4982

Stevenson, K. B. et al. 2014, Science, 346, 838, 1410.2241

Storch, N. I., Anderson, K. R., & Lai, D. 2014, Science, 345, 1317, 1409.3247

Winn, J. N. 2010, ArXiv e-prints, 1001.2010

Winn, J. N., & Fabrycky, D. C. 2014, ArXiv e-prints, 1410.4199

Winn, J. N., Johnson, J. A., Albrecht, S., Howard, A. W., Marcy, G. W., Crossfield, I. J., & Holman, M. J. 2009, ApJ, 703, L99, 0908.1672

Wolszczan, A., & Frail, D. A. 1992, Nature , 355, 145

Wright, J. T., Marcy, G. W., Howard, A. W., Johnson, J. A., Morton, T. D., & Fischer, D. A. 2012, ApJ, 753, 160, 1205.2273

CHAPTER 2

EXO-PLANETARY TRANSITS OF LIMB BRIGHTENED LINES TENTATIVE SI IV ABSORPTION BY HD209458B [1]

Transit light curves for stellar continua have only one minimum and a "U" shape. By contrast, transit curves for optically thin chromospheric emission lines can have a "W" shape because of stellar limb-brightening. We calculate light curves for an optically thin shell of emission and fit these models to time-resolved observations of Si IV absorption by the planet HD209458b. We find that the best fit Si IV absorption model has $R_{p,\mathrm{Si\,IV}}/R_* = 0.34^{+0.07}_{-0.12}$, similar to the Roche lobe of the planet. While the large radius is only at the limit of statistical significance, we develop formulae applicable to transits of all optically thin chromospheric emission lines.

2.1 Introduction

Since the first observation of a transiting exoplanet (Charbonneau et al., 2000; Henry et al., 2000), knowledge of exoplanetary radii, composition and atmospheres has grown explosively. In-transit and out-of-transit spectroscopy and photometry have revealed water absorption in HD 189733b (Beaulieu et al., 2008), atmospheric emission in TrES-1 (Charbonneau et al., 2005), a surprising number of anomalously large planets (Baraffe et al., 2010), and constraints on exoplanetary composition (Rogers & Seager, 2010). Accurate transit timing can also indicate the presence of additional bodies in the system through perturbations to the transiting planet's orbit (Agol et al., 2005; Holman & Murray, 2005).

[1] THIS CHAPTER IS PUBLISHED AS Schlawin et al. (2010)

When transits are observed in stellar Lyman-α, C II, Si III, Mg II and O I emission, they show much deeper minima than for visible wavelengths, revealing escaping atmospheres extending far beyond the geometric radii[2] of planets (Vidal-Madjar et al., 2004; Ben-Jaffel, 2007; Murray-Clay et al., 2009; Lecavelier des Etangs et al., 2010; Fossati et al., 2010). These light curves also constrain atmospheric conditions and mass escape from the planet's Roche lobe (Knutson et al., 2007; García Muñoz, 2007; Linsky et al., 2010).

Transit searches have been largely in the optical and near-infrared continuum, where the star is optically thick and limb darkened due to the temperature profile at the $\tau \approx 1$ surface of the star. For limb darkened wavelengths, the flux from the transiting system is at a minimum when the planet crosses the sub-earth longitude of the star (phase = 0.0) because the stellar disk is brightest at its center.

By contrast, emission lines from stellar chromospheres and transition regions can be limb *brightened* such as in Figure 2.1. For optically thick emission, limb brightening occurs when the source function increases with stellar altitude. For optically thin emission, strong limb brightening occurs because the chromospheric and transition region gas has its largest column density at the edges. Assef et al. (2009) showed that transit observations of chromospheric emission lines decrease sharply to a minimum at the first limb, increases to a local maximum mid-transit and then reverses the process as the planet exits the stellar disk. As a consequence, such a transit curve will be "W"-shaped.

Assef et al. (2009) point out that limb brightening could be useful for detecting exoplanetary transits of giant stars. Light curves of limb brightened

[2]In this paper, we define the geometric radius as the radius derived from broadband visible wavelength transit depths.

wavelengths have deeper minima than for both limb darkened and uniform disk emission. The star emits over a smaller effective area–a ring instead of a disk–so the planet covers a larger amount of the stellar flux. This is important for transits of giant stars where broadband transit depths can be below 0.01% for Jupiter-sized planets. Also, the planet covers its host's limb for a small fraction of the transit, allowing for feasible detection of giant star transits with ground based telescopes, which suffer from systematic photometric errors over timescales longer than one night. The exoplanets 4UMa b, HD 122430b, HD 13189b, and HIP75458 b all have transit probabilities greater than 10% and may be useful targets for future studies (Assef et al., 2009).

Assef et al. (2009) approximate the limb brightened star as a central disk of emission surrounded by a circularly symmetric ring with ~30 times the intensity. With this ring approximation, the maximum depth of the transit is proportional to the ratio of the planet radius to stellar radius, R_p/R_* if the emission from the central disk is negligible, instead of $(R_p/R_*)^2$, as expected for a uniform disk. This is because the planet covers ~2R_p out of a circle of emission whose total circumference is $2\pi R_*$.

In this paper, we present a transit light curve calculation for an optically-thin and geometrically-thin shell of emission. The calculated maximum transit depth scales as $(R_p/R_*)^{3/2}$, instead of R_p/R_*. In §2.2 we calculate the expected limb brightened light curve for an optically thin emission line. We consider optically thin emission because it shows at least 8 times the limb brightening of optically thick emission (Kastner & Bhatia, 1992). We fit this model light curve to Si IV emission from HD209458 in §2.3 and discuss the implications for HD209458b's thermosphere in §2.4.1.

2.2 A Limb Brightened Curve Under The Thin-Shell Approximation

We make the approximation that the thickness of the chromosphere, h, is much smaller than the size of the planet (R_p) and star (R_*). Under this geometrically thin approximation, the total flux from the star is proportional to the surface area of the hemisphere facing the Earth (as pictured in Figure 2.1c), times its thickness h, because the total flux for an optically thin emission line is proportional to the total number of emitting ions. Neglecting any photospheric contribution, the amount of emission that the planet blocks is then simply the amount of the stellar surface that the planet covers times h. In this geometrical limit, therefore, the thickness of the chromosphere, h, cancels out.

We compute the light curve for zero thickness ($h = 0$) by finding the area of the planet's shadow and dividing this by the surface area of a hemisphere with radius R_*. The volume of the intersection of a cylinder with a sphere is given by Lamarche & Leroy (1990) and we find the surface area of the intersection by taking a partial derivative with respect to the radius of the sphere. The result can be expressed analytically in terms of elliptic integrals. Let x be the distance, in units of stellar radii, R_*, from the center of the planet to the center of the star projected onto a plane perpendicular to the observer. Let p be the planet/star radius ratio, $\mathrm{R}_p/\mathrm{R}_*$. To calculate the light curve for a planet that does not pass through the center of the star, one can simply write $x(t)$ as $\sqrt{d^2 + b^2}$, where d is the distance to the closest approach point in stellar radii R_* and b is the impact parameter in stellar radii R_*.

The transit depth, $\delta(x)$ is a piecewise function with three different regimes:

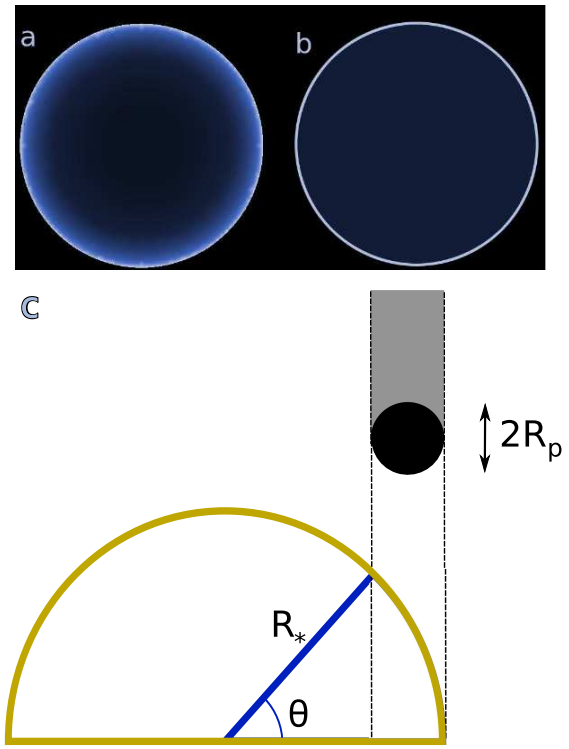

Figure 2.1: Model Limb Brightening. (a) A model of spherically symmetric optically thin emission varies continuously from limb to center. (b) An approximate model where most of the emission is from the stellar limb surrounding a uniformly emitting circle. We employ the model shown in (a) for Si IV emission, whose transit light curve is given by Equation 2.1. (c) Edge-on view of area of stellar emission and the amount blocked by a planet. This blocked surface area is the same as the area of a shadow cast by a sphere onto a hemisphere.

(1) when the planet is fully contained in the stellar disk (2) when the planet is at egress/ingress and (3) when the planet is beyond the stellar disk. We also include the case that the planet's absorption profile is larger than the star. In this case, the same formulae apply–see Table 2.1. A small figure for each regime is included in the equations, where an open circle represents the star and a filled circle represents the planet.

			
$p < 1$	$0 < x < 1 - p$	$1 - p < x < 1 + p$	$1 + p < x$
			 or
$p > 1$		$p - 1 < x < 1 + p$	$0 < x < p - 1$ or $x > p + 1$
a_0	$\sqrt{m}$	1	0
a_1	$\frac{1}{m}$	1	
a_2	$x^2 - p^2$	$1 - 2p(x + p)$	
m	$\frac{4xp}{1-(x-p)^2}$	$\frac{1-(x-p)^2}{4xp}$	
n	$-4xp/(x - p)^2$	$1 - (x - p)^{-2}$	

Table 2.1: Variable Definitions

$$\delta(x) = \Theta(p - x) + \frac{a_0}{2\pi\sqrt{xp}} \times \left[\frac{x + p}{x - p}\Pi(n, m) - 4xpa_1E(m) - a_2K(m)\right] \tag{2.1}$$

where $K(m)$, $E(m)$, and $\Pi(n, m)$ are the complete Legendre elliptic integrals of the first, second, and third kinds, and $\Theta(x)$ is the Heaviside step function. For the elliptic integrals, we use the conventions of Abramowitz & Stegun (1972) where $\Pi(n, m) = \Pi(n; K(m)|m)$ for the third elliptic integral. [3]

These formulae are difficult to evaluate numerically at $x = 0$, $x = p$ and $x = 1 \pm p$ due to the formal divergence of different terms in equation 2.1 and Table 2.1; the divergences cancel out analytically, but routines that evaluate the elliptic integrals diverge. However, these locations are a set of measure zero, and thus are tractable when modeling data.

[3] An IDL procedure for the transit depth $\delta(x)$ is located at `http://www.astro.washington.edu/agol/`.

2.2.1 Analytical Transit Depth Estimation

The transit is deepest slightly before second contact, so we can estimate the maximum transit depth as follows fromFigure 2.1c by comparing the total emitting area of the star to the total stellar surface area blocked by the planet. The blocked surface is the same as the shadow produced by a sphere of radius R_p onto a hemisphere of radius R_*. When the planet occults the edge of the star (second contact), then the length of the arc of the long axis of the shadow is $R_*\theta$. The diameter of the planet is $2R_p \approx R_*(1-\cos\theta) \approx \frac{1}{2}R_*\theta^2$, where the latter approximation is valid for $\theta \ll 1$. We can approximate the shadow as an ellipse with a semi-minor axis of R_p and a semi-major axis of $\frac{1}{2}R_*\theta$, so the area of the shadow is $A_t = \pi\sqrt{R_pR_*}R_p$. Thus, the maximum depth of transit is given by

$$\delta_{\max} \approx \frac{A_t}{2\pi R_*^2} = \frac{1}{2}\left(\frac{R_p}{R_*}\right)^{3/2} \tag{2.2}$$

which is accurate to within 5% for $R_p/R_* < 0.23$. Note that this is a different scaling for maximum transit depth than that given in Assef et al. (2009) who assume that most of the stellar emission is from a thin ring. For $R_p/R_* = 1-\sqrt{3}/2$, half of the stellar emission is within R_p of the stellar radius R_*, so for $R_p/R_* \gtrsim 0.13$, the ring approximation is valid, but the scaling of transit depth assumes negligible limb curvature at the scale of the planet ($R_p/R_* \ll 1$).

The remarkable consequence of Equation 2.2 is that the depth of a chromospheric transit does not decline as much with the radius of the planet as a transit of a uniform disk. A chromospheric transit has a maximum depth that is $\approx \frac{1}{2}\left(\frac{R_*}{R_p}\right)^{1/2}$ times deeper than the maximum transit depth of a uniform disk; thus smaller planets have an advantage to be observed at chromospheric wavelengths, as emphasized by Assef et al. (2009). It should also be noted that at mid-transit, the Double-U curve has a smaller transit depth than for a uniform

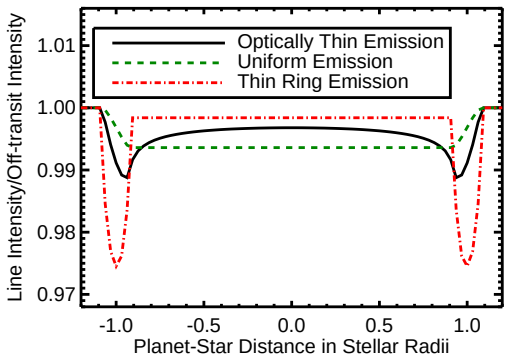

Figure 2.2: Transit light curve for $R_p/R_* = 0.08$, using a family of 3 different models. The solid line is for a transit of an optically thin shell using equation 2.1 where the emission looks like Figure 2.1 a. The "Uniform Emission" (Mandel & Agol, 2002, dashed green line) is one for which the emission is assumed to be constant across the stellar disk. The "Thin Ring Emission" model (dot-dash red line) is a model where the emission is assumed to be mostly from a thin ring as pictured in Figure 2.1 b. Note that the "Thin Ring" and "Optically Thin Emission" models' minima are deeper than the uniform emission model and that these minima occur near the stellar limbs.

disk, because the planet covers only πR_p^2 out of a hemisphere of area $2\pi R_*^2$.

Figure 2 (solid curve) shows the transit light curve, 1-$\delta(x)$, for a planet that has R_p/R_*=0.08. The estimate given by equation 2.2 and the more detailed equation 2.1 agree well, predicting maximum chromospheric depths to be 1.8 times deeper than for uniform disk brightness. (For a uniform disk emission $\delta_{\max}=\pi R_p^2/(\pi R_*^2)$). We also include a light curve for the thin circle of emission shown in Figure 2.1 b for comparison.

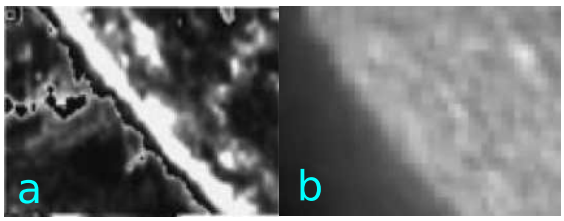

Figure 2.3: (a) Si IV emission from the Solar limb as observed by SUMER (Solar Ultraviolet Measurement of Emitted Radiation) (Wiik et al., 1997) is strongly limb-brightened, indicating that a transit of this emission line should have a Double-U light curve. (b) He II 304 image of the solar limb, taken by the Extreme-ultraviolet Imaging Telescope (Feldman et al., 2000) is, by contrast, not limb brightened because it is optically thick in the chromosphere and thus the additional column density at the limb does not contribute any more flux than the central disk.

2.3 Si IV Absorption by HD 209458b

Vidal-Madjar et al. (2003, 2004) observed the exoplanet host HD 209458 with the Hubble Space Telescope Imaging Spectrograph (STIS) instrument and found an extended hydrogen, oxygen and carbon atmosphere around the planet by fitting the light curves to the H I, O I and C II lines during a transit. Vidal-Madjar et al. (2004) found no Si IV absorption when fitting the light curve to a model of a spherical planet occulting a *uniform* stellar disk.

We fit their Si IV 1394 data (Vidal-Madjar et al. (2004), Figure 3) with a Double-U model given by equation 2.1. This model is appropriate for the Si IV emission, as evident in the Solar image in Figure 2.3 (a) where strong limb-brightening is apparent. France et al. (2010) found that the Si IV 1394 / Si IV 1403 ratio is 2:1 within the errors, indicating that the Si IV 1394 emission is optically thin (Bloomfield et al., 2002; Christian et al., 2006). We investigated the transit

of the Si IV line because it the strongest optically thin line in HD209458b's STIS spectrum. While other limb brightened emission lines do exist, we focus on the optically thin ones because they should be the most limb brightened.

The model has two free parameters: the planet/star radius ratio R_p/R_* and an overall constant that sets the off-transit flux. The second parameter is necessary since the off-transit Si IV 1394 STIS flux is poorly constrained. The impact parameter is fixed with a value of $b = 0.50R_*$, using an inclination of 86.7° and a semi-major axis $a = 8.76R_*$ (Torres et al., 2008).

Figure 2.4 shows the light curve for the Vidal-Madjar et al. (2004) data and the best fit model. In addition to the best fit model, we show two more limb brightened models where R_p/R_* is a fixed parameter for comparison. These have R_p/R_* equal to 0 and 0.12, representing no Si IV absorption and the geometric planet radius (Knutson et al., 2007), respectively.

Using a Levenberg-Marquardt fitting algorithm (Markwardt, 2009) and the points at which the $\chi^2 - \chi^2_{min} = 1$ to calculate uncertainties, we find that $R_p/R_* = 0.34^{+0.07}_{-0.12}$, close to the size of the Roche Lobe. The Double-U model has a total χ^2 of 10.4 with 12 data points and two parameters, which is 3.1 less than fitting the data to a constant flux line (representing no detection) with one parameter. Since these models are nested, we can use the maximum likelihood ratio test. The P-value for the difference in χ^2 is 0.05, so the data favor the Double-U model with 95% confidence, assuming normally distributed data. The same test favors the R_p/R_* =0.34 model over the $R_p/R_* = 0.12$ model with 91% confidence.

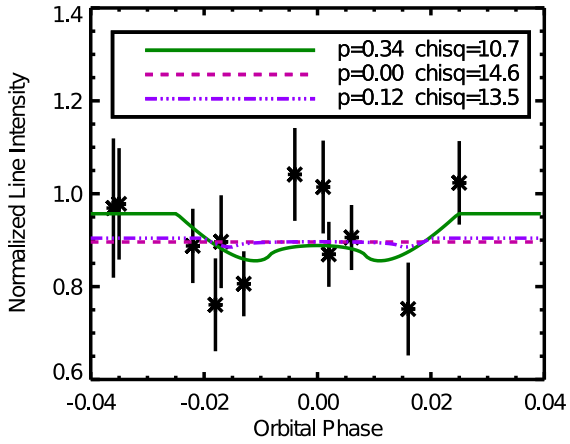

Figure 2.4: The light curve of the limb-brightened transition region line Si IV during the transit of HD209458b, as taken by Vidal-Madjar et al. (2004) for a wavelength range of [1391 ,1397]. Fluxes are normalized so that the weighted average of the points when the planet is not occulting the star is 1.0. The solid line is a best fit model, using equation 2.1 where the radius is a free parameter. For reference, two different best-fit models are shown where the planet size is a fixed parameter: the dashed curve is a horizontal line, corresponding to $R_p/R_* = 0$ or a non-detection of Si IV absorption. The dash triple-dotted line is a model with the geometric radius, $R_p/R_* = 0.12$. The best-fit radius, R_p/R_*=0.34 (normalized $\chi^2 = 1.07$), indicates Si IV absorption from a Roche lobe-sized cloud.

2.4 Conclusion

As indicated by the Solar image of Si IV in Figure 2.3, a limb brightened model should be used for Si IV emission. The Double-U model for the Si IV transit fits the data better than a non-detection, even when accounting for the additional parameters in the model. The best fit absorption radius $R_p/R_*=0.34^{+0.07}_{-0.12}$, if the absorption is entirely optically thick. This radius favors planetary atmosphere models with mass flow beyond the planet's Roche lobe.

The best time to observe transits in optically thin stellar emission lines is

when a planet crosses its host's limb and not at a phase of 0, since the Double-U curve is deepest at the stellar limb. Observations at the limb have a depth of ~0.5 $(R_p/R_*)^{3/2}$ whereas at the center of the star they have a transit depth of ~0.5 $(R_p/R_*)^2$, only half the depth of a uniform brightness transit.

2.4.1 Discussion

The Si IV transit depth is comparable to the O I transit depth calculated by Vidal-Madjar et al. (2004) and larger than the H I transit depth calculated by Ben-Jaffel (2007). As Koskinen et al. (2010) point out, a hard sphere, which we assume in equation 2.1, is a poor approximation to planetary atmospheric absorption. The Si IV absorption profile, instead of having a sharp transition from opaque to transparent, should change smoothly from optically thick to optically thin absorption in a more accurate model. In order to explain the large transit depth, this smooth model would have to have a radius extending beyond the planet's Roche lobe to explain the observed transit depth. $R_{\rm Roche}/R_*$ varies from 0.35 to 0.48 (Ben-Jaffel & Sona Hosseini, 2010) .

The best-fit transit depth supports models with high concentrations of metallic ions in the atmosphere because the radius of Si IV absorption is as large as for H I absorption. Koskinen et al. (2010) point out that if the metallicity is high, the temperature must also be elevated. The ~10,000 K temperature suggested by García Muñoz (2007), Murray-Clay et al. (2009), and Koskinen et al. (2010) for the thermosphere may not explain the large abundances of Si^{3+} needed for the observed absorption. The ionization energy, $\Delta E/k$ for $Si^{2+} \rightarrow Si^{3+} = 3.9 \times 10^5$K, suggests that the Si^{3+} may be produced in a shock between the stellar and plan-

etary winds.

Linsky et al. (2010) find no significant Si IV absorption by HD209458b. Our best fit to the STIS data predicts the average transit depth to be 9^{+4}_{-5}% for the same phases as their observations, but Linsky et al. (2010), with the Cosmic Origins Spectrograph (COS), found 0.2 ± 1.4%. These results disagree at the ~1.7σ level and variability in the planet's atmosphere may account for the discrepancy. Linsky et al. (2010) did observe some weak Si IV absorption features found at +20 and +40km/s in their spectrum, which indicates that some Si^{3+} ions remain in the planet's atmosphere or winds.

Linsky et al. (2010) suggest that the amount of another Silicon ion, Si^{2+}, may vary appreciably over short timescales because of changes in stellar wind speed, planetary mass-loss rate or temperature fluctuations. Conversely to Si IV, for which 2003 STIS observations indicate strong absorption and 2009 COS observations indicate weak absorption, the Si III absorption is seen strongly in absorption in the 2009 COS data and weakly in the 2003 STIS data.

Additional observations will help confirm or refute the detection of Si^{3+} in the thermosphere of HD209458b. The Cosmic Origins Spectrograph (COS) is an ideal instrument with 2 to 10 times the sensitivity of previous ultraviolet spectrographs (Froning & Green, 2009). COS was used by Linsky et al. (2010), but only when HD209458b was close to a phase of 0.0, 0.25, 0.5 and 0.75 and once when the planet was at the stellar limb. Additional observation at the host's limb would be optimal for Si IV and other optically thin emission lines. With enough signal to noise, the light curve may reveal asymmetries in the transit having to do with an asymmetric spatial distribution of the UV-absorbing cloud. The advantage of the limb brightened emission lines is that they come from a

smaller spatial area of the star and therefore probe the spatial distribution of the planetary atmosphere better than optically thick emission. Accurate time resolved transit data may also reveal small differences in *thermal* properties of the leading and trailing sides of the planet as predicted by Fortney et al. (2010) and Burrows et al. (2010).

E. Schlawin was supported by the NASA Space Grant Fellowship. E. Agol was supported in part by the NSF under Grant No. PHY05-51164 during a visit to the Kavli Institute for Theoretical Physics, and by NSF CAREER Grant No. 0645416. Support for Kevin Covey was provided by NASA through Hubble Fellowship grant #HST-HF-51253.01-A awarded by the Space Telescope Science Institute, which is operated by the Association of Universities for Research in Astronomy, Inc., for NASA, under contract NAS 5-26555. Lucianne Walkowicz is grateful for the support of the Kepler Fellowship for the Study of Planet-Bearing Stars.

BIBLIOGRAPHY

Abramowitz, M., & Stegun, I. A. 1972, Handbook of Mathematical Functions (Dover Publications)

Agol, E., Steffen, J., Sari, R., & Clarkson, W. 2005, MNRAS , 359, 567, astro-ph/0412032

Assef, R. J., Gaudi, B. S., & Stanek, K. Z. 2009, ApJ, 701, 1616, 0902.4237

Baraffe, I., Chabrier, G., & Barman, T. 2010, Reports on Progress in Physics, 73, 016901, 1001.3577

Beaulieu, J. P., Carey, S., Ribas, I., & Tinetti, G. 2008, ApJ, 677, 1343, 0711.2142

Ben-Jaffel, L. 2007, ApJ, 671, L61, 0711.1432

Ben-Jaffel, L., & Sona Hosseini, S. 2010, ApJ, 709, 1284, 0912.1409

Bloomfield, D. S., Mathioudakis, M., Christian, D. J., Keenan, F. P., & Linsky, J. L. 2002, A&A , 390, 219

Burrows, A., Rauscher, E., Spiegel, D. S., & Menou, K. 2010, ApJ, 719, 341, 1005.0346

Charbonneau, D. et al. 2005, ApJ, 626, 523, arXiv:astro-ph/0503457

Charbonneau, D., Brown, T. M., Latham, D. W., & Mayor, M. 2000, ApJ, 529, L45, arXiv:astro-ph/9911436

Christian, D. J., Mathioudakis, M., Bloomfield, D. S., Dupuis, J., Keenan, F. P., Pollacco, D. L., & Malina, R. F. 2006, A&A , 454, 889, arXiv:astro-ph/0602447

Feldman, U., Dammasch, I. E., & Wilhelm, K. 2000, Space Science Reviews, 93, 411

Fortney, J. J., Shabram, M., Showman, A. P., Lian, Y., Freedman, R. S., Marley, M. S., & Lewis, N. K. 2010, ApJ, 709, 1396, 0912.2350

Fossati, L. et al. 2010, ApJ, 714, L222, 1005.3656

France, K., Stocke, J. T., Yang, H., Linsky, J. L., Wolven, B. C., Froning, C. S., Green, J. C., & Osterman, S. N. 2010, ApJ, 712, 1277, 1002.3218

Froning, C. S., & Green, J. C. 2009, Ap&SS , 320, 181

García Muñoz, A. 2007, Planet. Space Sci. , 55, 1426

Henry, G. W., Marcy, G. W., Butler, R. P., & Vogt, S. S. 2000, ApJ, 529, L41

Holman, M. J., & Murray, N. W. 2005, Science, 307, 1288

Kastner, S. O., & Bhatia, A. K. 1992, ApJ, 401, 416

Knutson, H. A., Charbonneau, D., Noyes, R. W., Brown, T. M., & Gilliland, R. L. 2007, ApJ, 655, 564, arXiv:astro-ph/0603542

Koskinen, T. T., Yelle, R. V., Lavvas, P., & Lewis, N. K. 2010, ApJ, 723, 116, 1004.1396

Lamarche, F., & Leroy, C. 1990, Computer Physics Communications, 59, 359

Lecavelier des Etangs, A. et al. 2010, ArXiv e-prints, 1003.2206

Linsky, J. L., Yang, H., France, K., Froning, C. S., Green, J. C., Stocke, J. T., & Osterman, S. N. 2010, ApJ, 717, 1291, 1005.1633

Mandel, K., & Agol, E. 2002, ApJ, 580, L171, arXiv:astro-ph/0210099

Markwardt, C. B. 2009, in Astronomical Society of the Pacific Conference Series, Vol. 411, Astronomical Society of the Pacific Conference Series, ed. D. A. Bohlender, D. Durand, & P. Dowler, 251–+

Murray-Clay, R. A., Chiang, E. I., & Murray, N. 2009, ApJ, 693, 23, 0811.0006

Rogers, L. A., & Seager, S. 2010, ApJ, 712, 974, 0912.3288

Schlawin, E., Agol, E., Walkowicz, L. M., Covey, K., & Lloyd, J. P. 2010, ApJ, 722, L75, 1008.1073

Torres, G., Winn, J. N., & Holman, M. J. 2008, ApJ, 677, 1324, 0801.1841

Vidal-Madjar, A. et al. 2004, ApJ, 604, L69, arXiv:astro-ph/0401457

Vidal-Madjar, A., Lecavelier des Etangs, A., Désert, J., Ballester, G. E., Ferlet, R., Hébrard, G., & Mayor, M. 2003, Nature , 422, 143

Wiik, J. E., Schmieder, B., Kucera, T., Poland, A., Brekke, P., & Simnett, G. 1997, Sol. Phys. , 175, 411

CHAPTER 3

A 0.8-2.4 MICRON TRANSMISSION SPECTRUM OF THE HOT JUPITER COROT-1B [1]

Hot Jupiters with brightness temperatures $\gtrsim$2000K can have TiO and VO molecules as gaseous species in their atmospheres. The TiO and VO molecules can potentially induce temperature inversions in hot Jupiter atmospheres and also have an observable signature of large optical to infrared transit depth ratios. Previous transmission spectra of very hot Jupiters have shown a lack of TiO and VO, but only in planets that also appear to lack temperature inversions. We measure the transmission spectrum of CoRoT-1b, a hot Jupiter that was predicted to have a temperature inversion potentially due to significant TiO and VO in its atmosphere. We employ the Multi-Object Spectroscopy (MOS) method using the SpeX and MORIS instruments on the Infrared Telescope Facility (IRTF) and the Gaussian Process method to model red noise. By using a simultaneous reference star on the slit for calibration and a wide slit to minimize slit losses, we achieve transit depth precision of 0.03% to 0.09%, comparable to the atmospheric scale height but detect no statistically significant molecular features. We combine our IRTF data with optical CoRoT transmission measurements to search for differences in the optical and near infrared absorption that would arise from TiO/VO. Our IRTF spectrum and the CoRoT photometry disfavor a TiO/VO-rich spectrum for CoRoT-1b, suggesting that the atmosphere has another absorber that could create a temperature inversion or that the blackbody-like emission from the planet is due to a spectroscopically flat cloud, dust or haze layer that smoothes out molecular features in both CoRoT-1b's emission and transmission spectra. This system represents the faintest

[1] THIS CHAPTER IS PUBLISHED AS Schlawin et al. (2014)

planet hosting star (K=12.2) with a measured planetary transmission spectrum.

3.1 Introduction

Transiting hot Jupiters are among the most observationally favorable sources for measuring atmospheric composition, global winds, temperature inversions and disequilibrium chemistry (e.g., Pont et al., 2013; Snellen et al., 2010; Rogers et al., 2009; Moses et al., 2011). Their large physical radii, frequent transits, high temperatures and large radial velocity amplitudes permit both the measurement of physical parameters (mass, radius, orbital elements) and the ability to test atmospheric models. The primary transit, when the planet goes in front of its host star, and the secondary eclipse, when the planet goes behind, are valuable opportunities to spectroscopically characterize the atmosphere. These spectra can be compared with models to determine mixing ratios of atmospheric gases, clouds, scatterers and/or aerosols. Furthermore, high quality spectra can be used to constrain the formation of exoplanets (e.g., Spiegel & Burrows, 2012), the extent of equilibrium/disequilibrium chemistry (e.g., Moses et al., 2011), vertical mixing (e.g., Visscher & Moses, 2011) and put the Solar System in context.

Transmission spectra and emission spectra of hot Jupiter atmospheres have already been used to detect Na (Charbonneau et al., 2002), K (Sing et al., 2011), Ca (Astudillo-Defru & Rojo, 2013), H (Vidal-Madjar et al., 2003), H_2O (e.g., Deming et al., 2013; Birkby et al., 2013), CO (e.g., Snellen et al., 2010) and possibly CH_4, (Swain et al., 2008, though see Gibson et al. (2012a)). Furthermore, emission and transmission spectra have been used to constrain the mixing ratios of these atoms and molecules. Of considerable interest is the relative

abundances such as the C/O ratio (Teske et al., 2013; Madhusudhan, 2012; Madhusudhan et al., 2011a), which gives clues as to the formation of planets such as circumstellar disk composition and location within the disk (e.g., Öberg et al., 2011; Moses et al., 2013).

Infrared observations of prominent molecular bands in hot Jupiters during secondary eclipse are used to infer an atmospheric temperature profile (e.g., Line et al., 2013b). The level of emission by gases of upper layers as compared to lower levels indicates their relative temperatures. For example, the brightness temperature of the 4.5 μm *Spitzer* band is expected to be higher than the 3.6 μm band for temperature-inverted planets because it encompasses several molecular bands that are high in opacity (and high in altitude), whereas the 3.6 μm band sees deeper in the atmosphere (Knutson et al., 2010).

Broadly, hot Jupiter atmospheres have been classified into (1) planets that have temperatures that decrease with altitude for observable pressures and (2) planets that contain a temperature inversion or stratosphere at observable pressures. We include an isothermal (constant temperature with altitude) in the later case. One possible explanation for the bifurcation into theses profiles is that TiO and VO absorption of stellar flux creates temperature inversions in some planets and not others (Hubeny et al., 2003; Fortney et al., 2008a). An alternative explanation is that the observational techniques to infer temperature inversions (like the 4.5 μm to 3.6 μm brightness ratio) are actually sensing the difference between clear atmospheres and dusty atmospheres, such as has been observed in HD 189733b (Pont et al., 2013; Evans et al., 2013). Recently, spectro-photometry of HAT-P-32b (Gibson et al., 2013b), HAT-P-12b (Line et al., 2013a), WASP-17b (Mandell et al., 2013), GJ 1214b (Kreidberg et al., 2014), GJ 436b (Knutson et al.,

2014) and phase curves of Kepler-7b (Demory et al., 2013) indicate that clouds and hazes may be common in exoplanet atmospheres.

The very short period hot Jupiters, such as WASP-12b (Hebb et al., 2009, P=1.09 days), WASP-19b (Hebb et al., 2010, P=0.79 days), HAT-P-32b (Hartman et al., 2011, P=2.2) and CoRoT-1b (Barge et al., 2008, P=1.51 days), are in the temperature regime where TiO and VO may be abundant atmospheric constituents (Fortney et al., 2010) – their brightness temperatures are respectively 3600 K (Crossfield et al., 2012), 2700 K (Abe et al., 2013), and 2500 K (Deming et al., 2011). TiO and VO are molecules that are so sensitive to the C/O ratio that their abundances decreases by a factor of ~100 going from C/O=0.54 (solar) to C/O=1 (Madhusudhan et al., 2011b). Their presence should be accompanied by a greater radius for the optical wavelengths (~450 to ~850nm) than for infrared wavelengths ($\gtrsim$1000nm) (Fortney et al., 2010) and could explain the bifurcation scheme of planets into temperature inverted and non-temperature inverted planetary atmospheres (Hubeny et al., 2003; Fortney et al., 2008a).

Recent transmission spectroscopy observations have measured the level of TiO and VO in the atmospheres of WASP-19b's, WASP-12b and HAT-P-32b. The first two planets lack temperature inversions (Line et al., 2013b), so TiO and VO should be removed from their higher altitudes. Indeed, Huitson et al. (2013) found that the transmission spectrum of the hot Jupiter WASP-19b has low levels of TiO as compared to theoretical models with solar abundances and local chemical equilibrium. Mancini et al. (2013) also find that WASP-19b's transmission spectrum is consistent with models without TiO/VO absorption. Observations of WASP-12b during primary transit and secondary eclipse were consistent with TiO/VO and TiH absorption (Swain et al., 2013; Stevenson et al., 2013)

but including aerosols in the calculated transmission models and adding HST optical data suggest that TiO/VO are not dominant absorbers (Sing et al., 2013). It is possible that WASP-12b's TiO and VO are trapped on the planet's night-side (Sing et al., 2013). HAT-P-32b's transmission spectrum also shows a lack of strong TiO/VO features, possibly due to gray-absorbing clouds (Gibson et al., 2013b).

The hot Jupiter CoRoT-1b, orbiting a 5960 K effective temperature V=13.6 star (Barge et al., 2008), is better matched with models that include a temperature inversion (Rogers et al., 2009; Gillon et al., 2009; Zhao et al., 2012) or an isothermal profile (Deming et al., 2011). It is thus is a potential candidate for strong observable signatures of TiO/VO. This makes CoRoT-1b a useful comparison planet to WASP-19b and WASP-12b because it has a similarly high brightness temperature (>2000K) but a different temperature profile. Deming et al. (2011) additionally find that CoRoT-1b's secondary eclipse spectrum is well fit by a blackbody, which could indicate an isothermal temperature gradient or, alternatively, a high altitude dust such as been found in HD 189733b (Pont et al., 2013).

CoRoT-1b is favorable for characterization due to its large radius ($R_{\rm p}$ = 1.49 $R_{\rm Jup}$ Barge et al., 2008), high temperature ($T_{\rm blackbody}$ = 2450 K Deming et al., 2011) and moderate mass $M_{\rm p}$ = 1.03 $M_{\rm Jup}$, which combine to give it a large scale height $H = kT/\mu mg \approx 0.01 R_{\rm Jup}$ where k is Boltzmann's constant, T is the kinetic temperature, μ is the mean molecular weight =2.3 for a solar mixture, m is one atomic mass unit and g is the local gravitational acceleration. Furthermore, there is a nearby reference star close in brightness and color (within 0.7 magnitudes in the J, H and K bands) that permits characterization with the MOS method

(Bean et al., 2010; Sing et al., 2012; Gibson et al., 2013a; Bean et al., 2013).

The MOS method is to divide a target star spectrum by one (or an average of several) reference stars to correct for variability in telluric (Earth's) transmission and the response of the instrument. Close proximity of a reference star to the target provides an advantage for calibration, as their atmospheric turbulence and telluric fluctuations are highly correlated. The reference stars' spectra are obtained simultaneously either with multiple slits or, as in our observations, a long slit that includes both the planet hosting star and the reference star.

One observational challenge with the CoRoT-1 system is its faintness at K=12.2. This makes it difficult to obtain sufficient signal to noise for high resolution measurements but we demonstrate that the Infrared Telescope Facility (IRTF) with SpeX and MORIS instruments in a low resolution prism mode (with no diffraction grating) can achieve high precision characterization down to this faint magnitude. We present a 0.8 μm to 2.4 μm transmission spectrum to constrain the presence of infrared absorbing molecules and measure the optical/near IR radius slope as compared to TiO/VO absorption.

3.2 Observations

We observed CoRoT-1b with the SpeX instrument (Rayner et al., 2003) on the Infrared Space Telescope Facility in a low resolution prism mode. When the large 3″ x 60″ slit is placed on CoRoT-1, the actual resolution for the target star is set by the point spread function at $R \approx 80$. A reference star – 2MASS 06482020-0306339 – was placed simultaneously on the slit to correct for telluric transmission variations as well as correlated (common mode) instrumental variations. The 3″ x

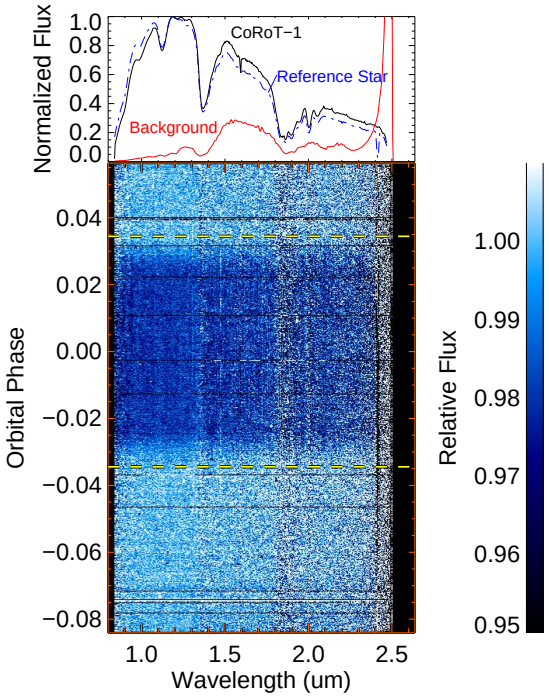

Figure 3.1: *Top* Normalized spectra for the planet hosting star, the reference star and background for Jan 04, 2012 indicate the regions where there are strong telluric absorption features, strong background emission and detector effects (spurious absorption features at 2.41 μm and 1.58 μm). *Bottom*: Dynamic spectrum for the night of Jan 04, 2012. Each row in the image is a single spectrum of CoRoT-1 divided by the reference star and renormalized with a linear baseline. The transit (encompassed by horizontal yellow dashed lines at ingress/egress) is clearly detected in all wavelength channels save the ends of the spectrograph.

60″ slit was selected to minimize slit losses but it still serves to reduce the background levels as compared to a completely slit-less instrument. The reference star with J=11.72, H=11.54, K=11.50 is slightly brighter than CoRoT-1 J=12.46, H=12.22, K=12.15 as determined from 2MASS (Skrutskie et al., 2006) so that the photon noise of the planet host star dominates the photon noise of the measurement. We kept the exposure times short to keep the counts of the two objects

well within the linear regime of the detector. At the same time, their fluxes are close enough so that flux-dependent non-linearity is negligible.

We observed CoRoT-1 for 3 nights on the UT dates of Dec 23, 2011 (full transit), Dec 29, 2011 (half transit) and Jan 04, 2012 (full transit). The first half of Dec 29, 2011 was lost due to high wind (>45 MPH) and closure of the telescope. The remainder of the Dec 29, 2011 night was affected by large seeing fluctuations from 0.9″ to 1.5″. For the full transits, the 2.5 hour transit duration was straddled by 30 to 120 minutes of out-of-transit observations to establish a baseline flux level. Table 3.1 lists the exposure times and number of exposures obtained for the three transits.

We also used MORIS, a high-speed, high-efficiency optical camera (Gulbis et al., 2011) simultaneously with SpeX to obtain photometry at the Sloan z' band for CoRoT-1. We used a 0.9 μm dichroic to split visible light short-ward of 0.9 μm into the MORIS beam path. The field of view of MORIS is similar to the guide camera of SpeX (1′ x 1′ arcmin), permitting us to include two reference stars in addition to CoRot-1 on the MORIS detector. We used short exposures of 5s and 10s to ensure the fluxes were well within the linear regime of the camera. The observing log of MORIS is also included in Table 3.1. Photometric data reduction was carried out following the pipeline and steps of Zhao et al. (2012). The total flux of the two reference stars (2MASS 06482101-0306103 and 2MASS 06482020-0306339) was used for flux calibration. We determined that an aperture size of 36 pixels (corresponding to 4.1″ for a pixel scale of 0.114″/pixel) and a 35-pixel wide background annulus provided the best light curve precision for all 3 nights, although aperture sizes with ±5 pixels gave essentially the same results.

The spectral images were reduced with standard `IRAF ccdproc` procedures with four to eight flat frames, dark subtraction from identical exposure time frames and one to two wavelength calibration frames. Wavelength calibrations were performed with a narrower (0.3″x60″) slit to better centralize the Argon emission lines. Additionally, we rectify all science images using the Argon lamp spectrum as a guide to make sure all vertical columns in the image correspond to individual wavelengths.

Simultaneous *H*+*K* band exposures were made with the infrared guider on SpeX to ensure good alignment of the target and reference star. The stars are visible as reflections off the slit, permitting a simultaneous check that the stars are centered during spectrograph science exposures. In addition to the reflections from the slit, nearby additional reference stars off the slit were also evaluated for centroid motions. The centroid motions show that guiding using the *H*+*K* guider was accurate to within 0.3″, minimizing slit loss errors in the spectrograph. No correlations are visible between telescope shifts (measured from *H*+*K* images) and the individual target and reference stars' fluxes or ratio spectrum between the planet host and reference star.

We extracted all of the spectra with the `twodspec` procedures in `IRAF` (Tody, 1993, 1986). We used a centered aperture of 15 pixels (2.3″) with optimal extraction (spatial pixels weighted by S/N ratio) on the planet host star and reference star (FWHM ≈5 to 9 px or 0.8″ to 1.4″) with a third order Legendre polynomial background subtraction from 89 pixels on each side of the spectrum. These extraction and background sizes were chosen experimentally so as to produce the smallest standard deviation of out-of-transit flux in the final time series. The fact that the highest precision was obtained with a 2.3″

UT Date	$t_{\rm spec}$ (s)	D_{spec}	$N_{\rm spec}$	$t_{\rm phot}$ (s)	$N_{\rm phot}$
Dec 23, 2011	10.0	49%	813	5	2636
Dec 29, 2011	15.0	51%	233	10	691
Jan 04, 2012	15.0	51%	600	5	3319

Table 3.1: Summary of the 2.5 transits observed for CoRoT-1b including the exposure time for SpeX spectra $t_{\rm spec}$, number of spectral exposures $N_{\rm spec}$, spectral duty cycle $D_{\rm spec}$, MORIS photometric exposure time $t_{\rm phot}$ and number of photometric frames $N_{\rm phot}$. The non redundant reads were increased at longer spectrograph exposure times, thus maintaining almost the same duty cycle.

aperture size shows that the 3″ slit width is sufficiently wide to make slit losses negligible.

For each exposure, the CoRoT-1 system's spectrum was divided by the reference star to correct for variable transmission and response of the instrument. This is the same long slit/multi-object method applied by Sing et al. (2012), Bean et al. (2010), Bean et al. (2013) and Gibson et al. (2013a). Figure 3.1 shows a dynamic spectrum from the night of Jan 04, 2012 using the reference star division and then re-normalizing each time series by a linear out-of-transit baseline. The linear baseline division is only used for illustrative purposes in this figure and not the parameter extraction described in Section 3.3.2. Each of the 475 wavelength channels clearly shows the transit except for the ends of the spectrograph due to low response and high thermal background at the larger wavelength end. The telluric transmission above IRTF at Mauna Kea is high enough that transit measurement is still possible between the J, H and K telluric windows.

3.2.1 Noise Measurements

The most critical part of measuring a planet's spectrum is achieving high signal to noise (S/N) ratios. Measurement errors are closely approximated by "minimum noise" at the highest time resolution and spectral resolution but are considerably larger when the data is binned. For this paper, "minimum noise" includes constant read noise per pixel of the detector, shot noise of the source and shot noise of the background. Minimum noise decreases as $1/\sqrt{N}$ for N independent measurements, but we find that the measured noise falls off more slowly, as expected for high precision measurements dominated by systematics. These additional error sources are also known as time-correlated or wavelength-correlated red noise (e.g., Pont et al., 2006; Carter & Winn, 2009). Figure 3.2 and 3.3 show the measured out-of-transit error as a function of bin size and also shows the minimum noise for comparison.

For the data analysis, we used nine equally spaced wavelength bins which minimize the out-of-transit noise while still maintaining sufficient spectral resolution to resolve molecular bands. As expected for high precision flux measurements, the measured noise has components that do not scale as minimum noise decreases. We bin the time data slightly to ~3 min long time bins for computational efficiency when doing MCMC/Gaussian Process fitting. This is still far from the noise floor seen in Figure 3.3 and shorter than the planet's transit ingress duration of 22 minutes and the typical systematics ~10 to ~60 minutes.

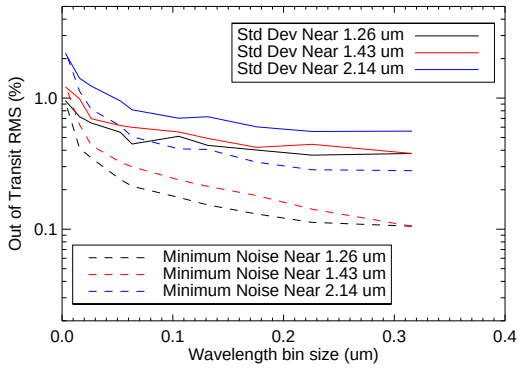

Figure 3.2: Measured out of transit errors as a function of wavelength bin size for the night of Dec 23, 2011. The errors scale with minimum noise but in a non-linear way. We choose the maximum bin size possible while still resolving some broad molecular bands and use 0.17 μm bins for time series analysis. The minimum noise drops quickly for the 0.3 μm bin near 1.43 μm because there is a sharp increase in photons outside of the telluric absorption feature.

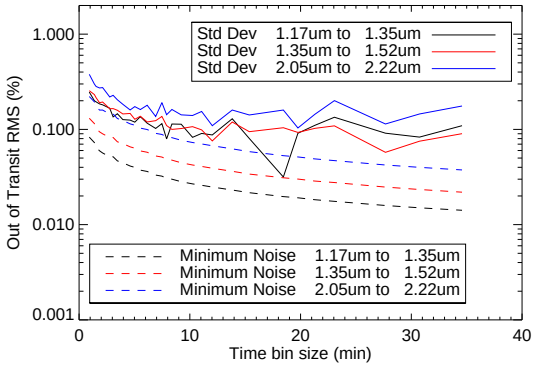

Figure 3.3: Measured out of transit errors as a function of time bin size for the night of Dec 23, 2011 using 0.17μm wide bins. As with the wavelength binning, the measured noise falloff is not as sharp as with minimum noise. For 0.17 μm wide wavelength bins there is an approximate noise floor around 0.1% and a baseline function must be used to remove long term trends. The variations in RMS for long time bins are due to small number statistics for the handful of out-of-transit flux points.

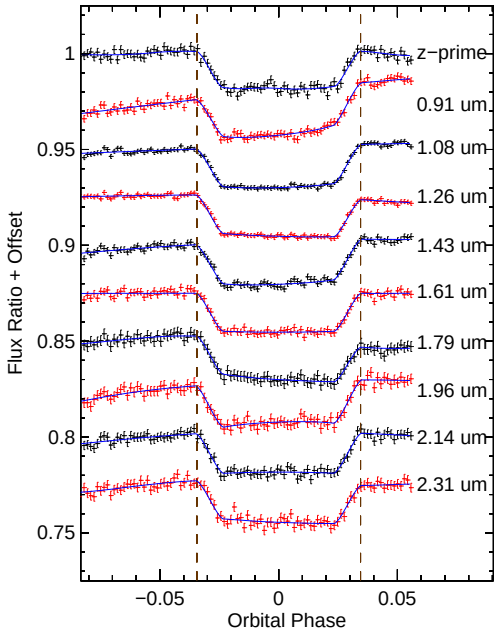

Figure 3.4: Time series for the night of January 04, 2012 binned into 100 time points. The top curve (z-prime) is the MORIS photometry whereas the remaining nine are equally spaced SpeX bands. The transit light curves are fit with the Mandel & Agol (2002) light curve model and with a Gaussian process error matrix (Gibson et al., 2012b) that includes red noise but imposes no specific baseline function for the time series.

3.3 Light Curve Fitting

As described in Section 3.2.1, all R=80 spectral data were binned into nine equally spaced wavelength bins and they are analyzed independently. Figure 3.4 shows the time series for each wavelength bin and it can be seen that the baseline is non-linear. Figures 3.5 and 3.6 also show that the shape of the baseline changes from night to night. It is possible to model the baseline as a slowly varying function like a polynomial (e.g., Bean et al., 2013) and we initially fit the light curve with a third order Legendre polynomial. The Legendre polynomi-

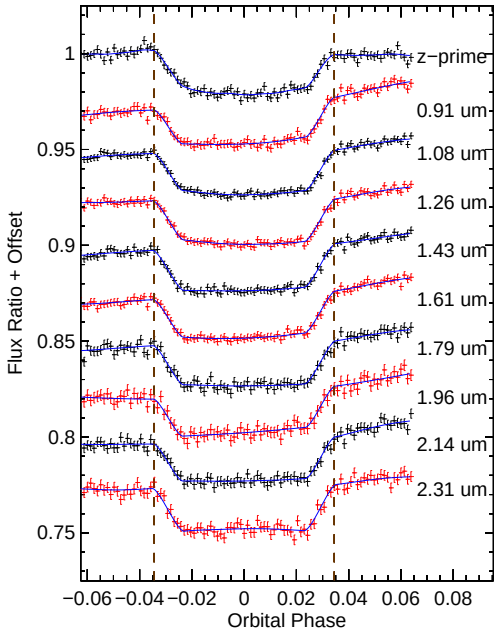

Figure 3.5: Same as Figure 3.4 for the night of Dec 23, 2011.

als were used because their orthogonality reduces the covariance between fitted coefficients. The polynomial fits showed discrepancies between nights, so we use a non-parametric approach detailed in Section 3.3.1 rather than impose a specific shape on the baseline fit.

3.3.1 Gaussian Process Model

We use a Gaussian process (Gibson et al., 2012b, 2013a) to model red noise and the flux baseline. The advantage of the Gaussian process framework is that it does not assume that the baseline follows a pre-defined function like a polynomial where the coefficients are fitted parameters. Instead, the Gaussian process assumes the baseline and mid-transit follow a correlated normal distribution de-

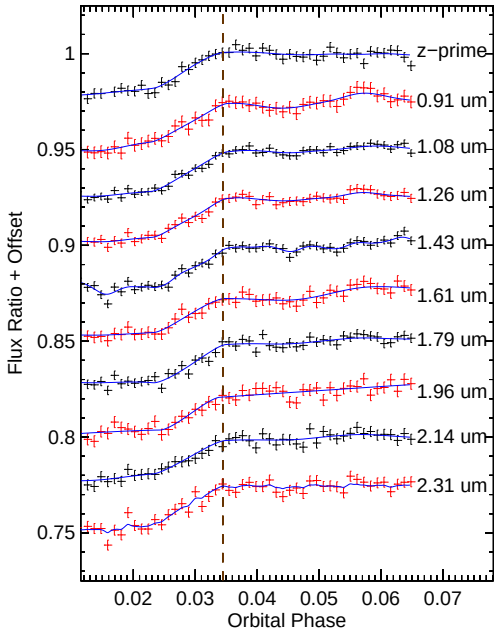

Figure 3.6: Same as Figure 3.4 for the night of Dec 29, 2011.

scribed by a covariance kernel. For repeated experiments following a Gaussian process, the actual shape of the baseline can vary from realization to realization while maintaining the same covariance kernel. The Gaussian Process method uses Bayesian model selection so that it weights against complex models to mitigate overfitting.

We use the integer form of the Matérn covariance kernel (Rasmussen, 2006),

$$C_{nm} = \Theta_0^2 \exp\left(-\Theta_1 \sqrt{2\left(p+\frac{1}{2}\right)}|x_n - x_m|\right) \frac{\Gamma(p+1)}{\Gamma(2p+1)} \times \left(\Sigma_{i=0}^{p} \frac{(p+i)!}{i!(p-i)!}\left(\Theta_1|x_n - x_m|\sqrt{8\left(p+\frac{1}{2}\right)}\right)^{p-i}\right) + \delta_{nm}\sigma_n^2 \quad (3.1)$$

where C_{nm} is the covariance between data points (x_n,y_n) and (x_m,y_m), Θ_0 is a

hyper-parameter describing the strength of the correlation between data points, Θ_1 is the inverse time scale hyper-parameter, p is the index of the Matérn kernel, δ_{nm} is the Kronecker delta function and σ_n is the white-noise component of an individual point's error. This is a generalized form of the $p = 1$ Matérn kernel used on WASP-29b transit data (Gibson et al., 2013a). We let the p parameter be another hyper-parameter with the possible values of 0, 1, 2 or infinity (a squared exponential kernel $C_{nm} = \Theta_0^2 e^{-\Theta_1 (x_n - x_m)^2/2}$) because higher values of p are essentially indistinguishable from the infinity case (Rasmussen, 2006). The four different kernels are parametrized by Θ_2 with values of 0, 1, 2 and 3 for the respective values of p. All forms of the above kernel have correlations that decrease with separation in time. In other words, points that are close together are highly correlated but far away are less correlated. For the data series in this work, x_n and x_m are orbital phase and y_n and y_m are normalized flux. The choice of kernel does not affect the individual white noise errors which are assumed to be independent and Gaussian distributed with a standard deviation σ_n.

The need for a covariance kernel is justified by the fact that the time series are not well fit by a flat baseline. If we do fit the time series to a flat, white noise baseline model – with fixed semi-major axis, impact parameter and orbital period from literature values (Bean, 2009) and free planet-to-star radius ratio R_p/R_* and free linear limb darkening – the resulting residuals show correlations, as visible in the autocovariance estimator. If the autocovariance has a spike at zero lag and then is flat for all lags greater than zero, the noise is independent and identically distributed - white noise. On the other hand, if there is structure to the autocovariance, then there are correlation between flux measurements. Figure 3.7 shows a few examples of the autocovariance estimator of the residuals and the autocovariance estimator of the best-fit Gaussian process

model. The autocovariance estimator is a biased estimator (Wei, 2006) so it can be different from the covariance kernel. Appendix A shows the kernel, individual realizations and the ensemble average of the autocovariance of the same best-fit hyperparameters used in Figure 3.7.

The inclusion of correlated noise requires that the full likelihood function must be used in evaluating a model instead of a plain χ^2 statistic. The full likelihood function is

$$\mathcal{L} = \frac{1}{(2\pi)^{n/2}|\mathbf{C}|^{1/2}} \exp\left(-\frac{1}{2}\mathbf{r}^T\mathbf{C}^{-1}\mathbf{r}\right) \tag{3.2}$$

where $\mathcal{L}$ is the likelihood function when evaluating a model for covariance matrix $\mathbf{C}$ and residual vectors $r_n = y_n - f_n$ for data value y_n and model value f_n and ^{T} is the transpose (Gibson et al., 2012b). In the case of statistically independent non-correlated data $\Theta_0 = 0$ and $\mathcal{L} \propto \exp^{-\chi^2}$ where $\chi^2 = \sum_n (y_n - f_n)^2/\sigma_n^2$, the standard chi-squared statistic. However, we find that $\Theta_0 \neq 0$ and that correlated noise is present in the data.

3.3.2 Extracted Parameters

We fit all time series with the transit function from Mandel & Agol (2002) and use a series of MCMC chains to explore the parameter uncertainty distributions. The out-of-transit flux, planet-to-star radius ratio R_p/R_*, linear limb darkening u_1 and hyper-parameters Θ_0, Θ_1 and Θ_2 are fitted to the data while all other transit parameters – impact parameter, semi-major axis and orbital period – are fixed at the literature values from Bean (2009). For all parameters and hyper-parameters we use flat priors. All parameters and hyper-parameters are constrained by the likelihood function except in the case where the covariance strength hyper-

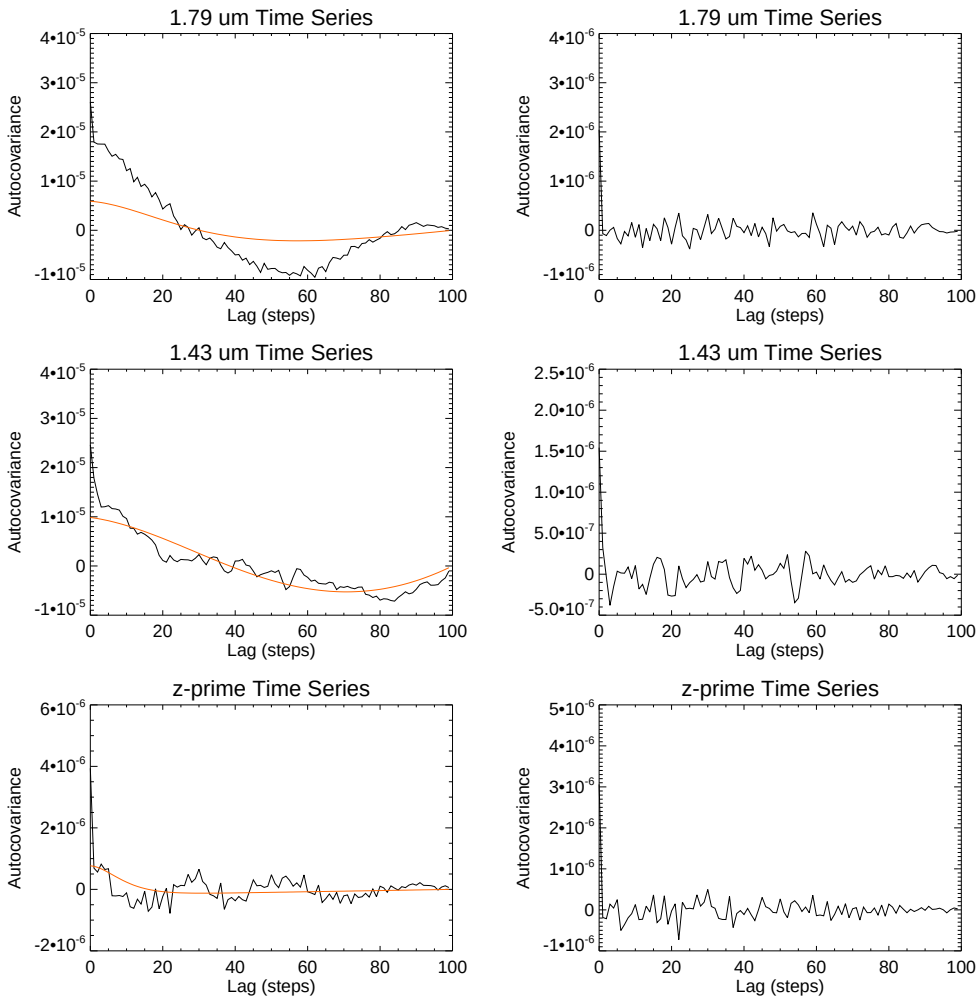

Figure 3.7: *Left*: Autocovariance estimator of the residuals fit with a white noise model and a flat baseline (black line) compared with the autocovariance estimator of a best-fit Gaussian Process model (orange line). These example light curves were for the SpeX 1.79 μm bin and SpeX 1.43 μm bin, which have stronger baseline trends, and the z' filter for Jan 04, 2012 data, which was flatter. Appendix A shows simulated individual realizations of the same Gaussian Processes and how they compare to the covariance kernel. *Right*: The same light curves are fit with the Gaussian-Process model and the autocovariance of the final residuals (black line) show no correlation between data, just the white noise peak at zero lag.

parameter (Θ_0) is much smaller than the white noise, σ_n. In these cases the time scale hyper-parameter (Θ_1) is poorly constrained but does not strongly affect the R_p/R_* result over many orders of magnitude. For the continuous parameters, we use Gaussian proposal distributions from the current value and for the discreet kernel index hyper-parameter (Θ_2), we use a uniform proposal distribution over the integers from 0 to 3.

Each time step in the MCMC chain requires a matrix inversion when evaluating the likelihood, which can make evaluation computationally expensive. To decrease chain evaluation time, the time series are binned to 100 time points for the nights of Dec 23, 2011 and Jan 04, 2012 with a resulting bin sizes of ~3 minutes. Although this is comparable to OH variation timescales, increased number of bins did not give different results. For Dec 29, 2011 we use 50 time points to keep the timescales comparable. The chains are run to 6000 points each with the first 1000 points discarded to allow for convergence, comparable to Gibson et al. (2013a)'s 5000 points with 1000 discards. The MCMC data series show stable parameter distributions beyond 1000 points. Three independent chains for all light curves are used to check for local minima and all final radius parameters and uncertainties agree between the chains to within 0.1%.

The example parameter correlation plot for the fit to the z' light curve of Jan 04, 2012 in Figure 3.8 shows how the fitted planet radius R_p/R_* can correlate to the other fitted parameters . This particular light curve showed the strongest dependence of R_p/R_* on the flux offset A_0 and hyper-parameters Θ_0, Θ_1 and Θ_2. For the remaining curves, the R_p/R_* posterior is nearly orthogonal to the other hyper-parameters.

The same `IRAF` data analysis pipeline and MCMC light curve fitting is ap-

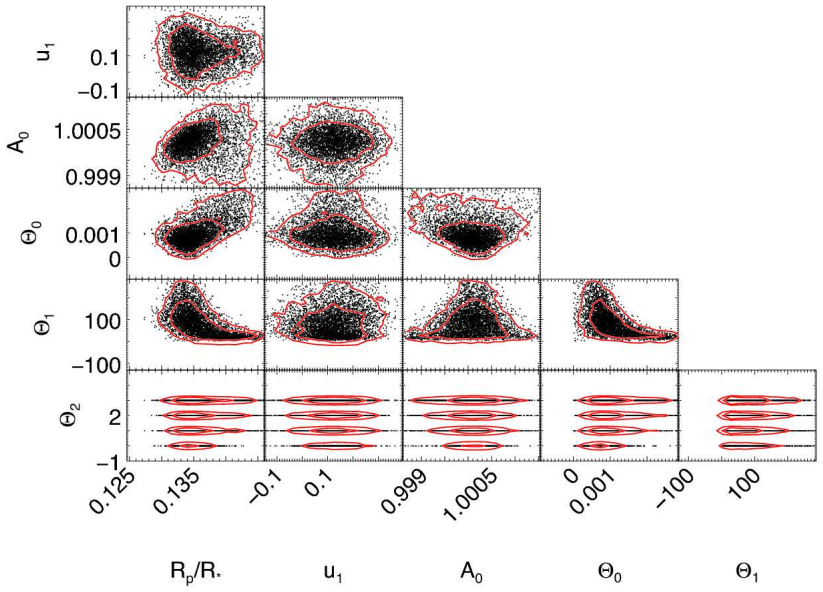

Figure 3.8: Posterior density distribution for the fitted parameters for the night of Jan 04, 2012 for the MORIS z' time series from the MCMC chain. The star to planet radius ratio R_p/R_* parameter correlates with the flux offset A_0, the hyper-parameters of the Gaussian process model Θ_0 (strength of correlations) and Θ_1 (inverse timescale of hyper-parameters) and Θ_2 (the Matérn type) but not u_1 (the linear limb darkening parameter) because R_p/R_* and u_1 have nearly orthogonal distributions. The Θ_2 parameter is a parametrization of the Matérn index p and is discrete – see Section 3.3.1 – so there is an apparent discontinuity in phase space. 95% and 68% confidence regions for each projected distribution are shown in red. The correlation between parameters is smaller for the rest of the other SpeX and MORIS light curves.

plied to all three nights of observation and the fitted radius ratio and uncertainties are shown in Figure 3.9. The three nights are consistent within errors for a given wavelength. However, there is a slight decrease in radius fit for the night of Jan 04, 2012.

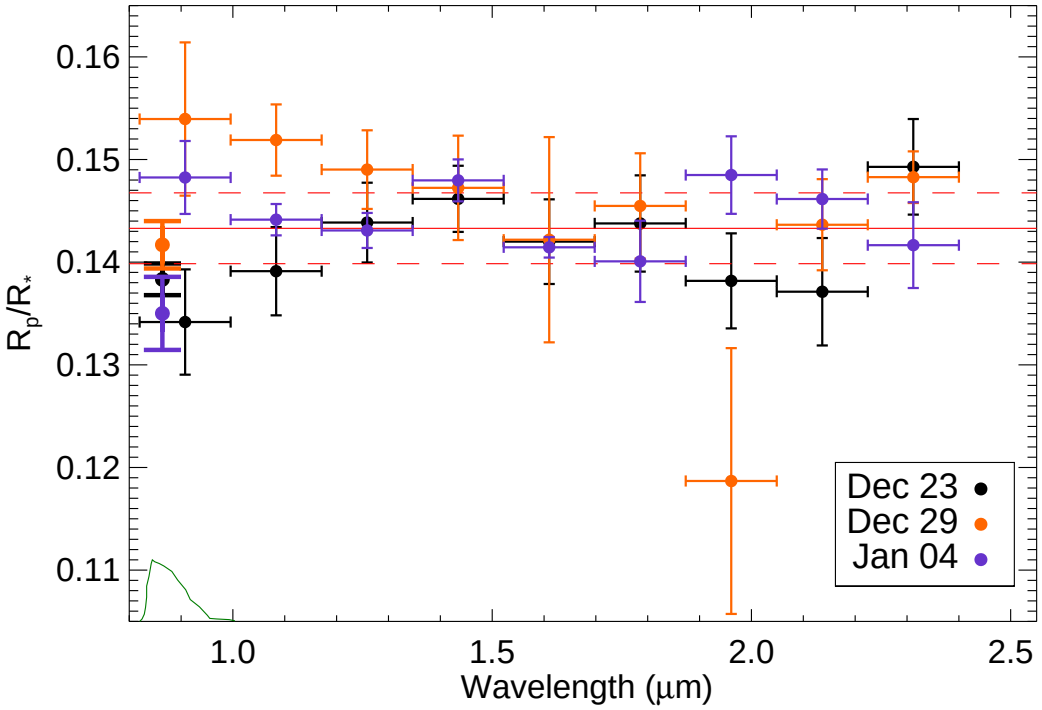

Figure 3.9: Fitted radius ratio parameter as a function of wavelength for the three independent nights of observations with horizontal error bars as the bandwidths for spectral wavelength bins and vertical error bars with 68% uncertainty. Points with bold lines are the simultaneous z' photometry with the MORIS camera with a filter transmission curve (normalized to unity and scaled to 1/10 the plot size) shown in green. At a given wavelength, all points are within 2.1σ of the weighted average, though there is a slight systematic shift downward for the night of Jan 04 (purple). The horizontal red line shows the CoRoT spacecraft radius (Bean, 2009) and the dashed red lines indicate three scale heights above and below this value.

The three sets of observations in Figure 3.9 are combined with a weighted average to produce a final transmission spectrum of the planet to be used in comparison to models. The weights are the inverse squared error in each wave-

length bin for each night. We make the assumption that weather-related variability on the hot Jupiter itself has a negligible effect on the transmission spectrum. We also assume that the errors in radius from night to night are independent.

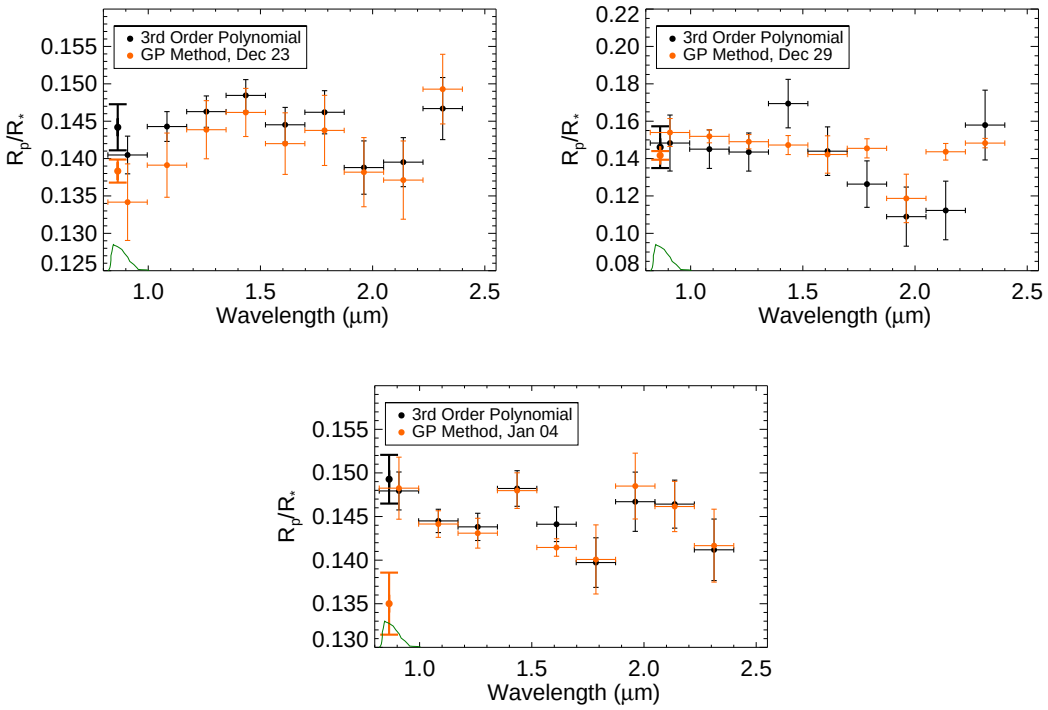

Figure 3.10: Comparison between a polynomial baseline Levenberg-Marquardt fit and a Gaussian process method for the baseline and flux variations. Photometry points (z' band) are shown with bold lines, and the corresponding z' bandpass is shown in green. The results are largely consistent for the SpeX data on the full transits of Dec 23, 2011 and Jan 04, 2012, but differ on the half transit of Dec 29, 2011 and the MORIS photometry for Jan 04, 2012. The MORIS photometry light curve for Jan 04, 2012 shows particularly large sensitivity to the fitting method because the flux bends down after egress – see Figure 3.4. For the half transits of Dec 29, 2011, the third order polynomial (due to the shorter time baseline) produces much larger scatter for the half transit than the Guassian process method because it is fitting a specific shape to the light curve in the presence of red noise.

It is worth noting that the Gaussian process method achieved higher precision than a polynomial baseline on the half-transit observation for Dec 29, 2011. Figure 3.10 shows a comparison between the best-fit radius when using a third order Legendre baseline fit as compared to the Gaussian correlated process. Both the scatter and error bars are larger when imposing a specific baseline shape. There was one particular light curve, the MORIS z' photometry for Jan 04, 2012, that showed a very strong dependence on the type of treatment of systematic errors. As seen in the time series, Figure 3.4, the flux bends downward after egress. When the light curve is fit with a third order Legendre polynomial, this drop in flux is extrapolated to a higher flux during transit and thus the planet-to-star radius ratio estimate R_p/R_* is large. When the light curve is fit with the Gaussian Process method, the deviations from a flat baseline are best-fit with shorter time scale correlations and an essentially flat baseline. Our Gaussian process kernel (Equation 3.3.1) incorporates different shapes through the Matérn index, but does not increase the upper limit to the same value as the polynomial baseline. We adopt the Gaussian Process model fits, but given the dependence of R_p/R_* on the method, we also evaluate our science results with the polynomial model fits.

The average spectrum, listed in Table 3.2, has R_p/R_* uncertainties ranging from 0.7% to 2% of the mean value ($R_{p,mean}/R_* = 0.144$) across the near-infrared coverage. This uncertainty is comparable to the scale height of the atmosphere (~0.8% for a 2400K atmosphere), whereas strong spectral features are expected to be three to five scale heights in planet radius variation (Burrows & Orton, 2009). Figure 3.9 shows no immediate statistically significant (5σ) molecular features.

Wavelength (μm)	R_p/R_*
z′ (0.86)	0.1389 ± 0.0012[a]
0.908	0.1450 ± 0.0027
1.083	0.1448 ± 0.0013
1.259	0.1440 ± 0.0014
1.434	0.1474 ± 0.0016
1.610	0.1415 ± 0.0010
1.786	0.1426 ± 0.0026
1.961	0.1431 ± 0.0029
2.137	0.1440 ± 0.0022
2.312	0.1470 ± 0.0020

Table 3.2: Weighted average planet-to-star radius ratio R_p/R_* for the three nights of observations shown in Figure 3.9. Quoted error bars are calculated by propagating the individual MCMC uncertainties in quadrature. The central wavelength for each 0.1755 μm bin is given in the first column except for the photometry filter where the first moment is given in parentheses. [a] the MORIS z' time series showed particularly large sensitivity to the treatment of systematic errors. A polynomial baseline fit gives a weighted average $R_p/R_* = 0.147 \pm 0.002$

3.4 Comparison with Models

The error-weighted average transmission spectrum for the three nights is compared against a representative model for hot Jupiter atmospheres from Fortney et al. (2008b, 2010). We select this model as a starting point because it has a published infrared spectrum, solar abundances and equilibrium chemistry. The blackbody temperatures fit to infrared data of ≈2400 K (T_{bb}=2380 K,T_{bb}=2460K Zhao et al., 2012; Deming et al., 2011), and short orbital period P = 1.509 days (Barge et al., 2008) indicate that it is comparable to the $T_{\rm kinetic}$=2500 K isothermal model from Fortney et al. (2010).

The equilibrium model from Fortney et al. (2008b, 2010) shows substantial

opacity in the optical as compared to the infrared due to mainly TiO and VO absorption, so we compare the CoRoT derived radius (Bean, 2009) to our transmission spectrum, as seen in Figure 3.11. The Bean (2009) radius is larger than the original discovery (Barge et al., 2008), but we adopt the Bean (2009) value because it was found with a newer data processing pipeline. The combined CoRoT data and IRTF data show no evidence for an optical to infrared slope. Fitting a flat spectrum to the data gives a reduced chi-squared ($\bar{\chi^2}$) of 2.9 for 10 degrees of freedom whereas the model with TiO/VO gives $\bar{\chi^2}$ of 4.6 for 10 degrees of freedom. The same model with TiO and VO artificially removed, gives $\bar{\chi^2}$ of 2.4 for 10 degrees of freedom. As mentioned in Section 3.3.2, the MORIS results were particularly sensitive to the choice of model to fit the time series. If we use a polynomial baseline fit to the time series, the TiO/VO rich model is again disfavored with a $\bar{\chi^2}$ of 2.9 as compared to the TiO-removed model with $\bar{\chi^2}$ of 1.6 and a flat line of $\bar{\chi^2}$ of 1.3.

The hot Jupiter WASP-19b also shows no evidence for TiO/VO absorption (Huitson et al., 2013; Mancini et al., 2013). For this planet, TiO/VO depletion is expected since WASP-19b has no observed temperature inversion (stratosphere) (Anderson et al., 2013). WASP-12b similarly has no stratosphere, but does have a larger optical to infrared transit depth ratio. Models for WASP-12b that included either TiO/VO or TiH were consistent with initial data (Swain et al., 2013; Stevenson et al., 2013) but adding optical data and including models with aerosols together suggest that WASP-12b has low levels of TiO/VO (Sing et al., 2013).

CoRoT-1b, by contrast, is better matched by models *with* a stratosphere or isothermal temperature profile. Rogers et al. (2009) compare a suite of equilib-

rium abundance models with multi-color photometric secondary eclipses on CoRoT-1b. The molecular features in these models appear in absorption or emission depending on the temperature structure of a planet's atmosphere and Rogers et al. (2009)'s models with no temperature inversion fail to produce the *Ks* and narrowband 2.1 μm brightness temperatures for the planet. The only models that come close to matching the observations include an extra optical absorber at the 0.01 to 0.1 bar level. Deming et al. (2011) also find that the secondary eclipse fluxes are better fit with models that include a temperature inversion than models without. Still, Deming et al. (2011) find consistency with a blackbody spectrum, which could be due to an isothermal profile or a thick layer of high altitude dust.

Plausible absorbers that could create a stratosphere in CoRoT-1b are TiO and VO (Fortney et al., 2008a), which should also increase the optical radius as compared to the infrared. However, since our IRTF-CoRoT combined spectrum is disfavored by models with TiO/VO absorption, we expect another species is responsible for the temperature inversion, such as sulfur-containing compounds (Zahnle et al., 2009). Alternatively, a high altitude haze or dust (e.g., Pont et al., 2013) could explain the blackbody-like emission from CoRoT-1b and also flatten out molecular features in the transmission spectrum.

Many other atmospheric optical scattering and absorbing processes may occur in hot Jupiter atmospheres including (a list from Sing et al. (2013)): Raleigh scattering off molecules, Mie and Raleigh scattering off dust, tholin hazes and gray absorbing clouds. The majority of these processes increase planetary radii at short wavelengths as compared to long wavelengths. Our observations, by contrast, show that the optical radius is not significantly larger than the infrared

radius based on the CoRoT photometry. Gray absorbing clouds are the one item on the above list that could equalize the optical and infrared transit depths. Recent observations of HAT-P-32b (Gibson et al., 2013b), HAT-P-12b (Line et al., 2013a), and Kepler-7b (Demory et al., 2013) indicate that high altitude clouds may be pervasive in exoplanet atmospheres. In HAT-P-32b, gray-absorbing clouds may obscure TiO/VO features (or the TiO and VO may be present at very low abundances) (Gibson et al., 2013b). Analysis of the above a processes is limited with only CoRoT photometry, but additional optical spectroscopy would be useful in constraining the strength of these scattering and absorbing phenomena.

We observe a 2σ peak at 1.4 μm in the spectrum, close to a 1.4 μm water feature seen in all temperature classes of Fortney et al. (2010)'s equilibrium models. This same feature was used to detect water vapor in WASP-19b with HST (Huitson et al., 2013). However, if water vapor in CoRoT-1b caused the 2σ feature at 1.4 μm, the 1.8 μm radius should also be elevated, which is not seen in our spectrum. One possible explanation is that the 1.4 μm peak is due to H_2C_2 or HCN, which are both predicted to be abundant in hot Jupiter atmospheres (Moses et al., 2013). Unfortunately, the significance level of this peak is too low to distinguish between these molecules or rule out the possibility of a statistical deviation or un-removed telluric absorption signature.

3.5 Conclusion

We present a 0.8 μm to 2.4 μm transmission spectrum for the hot Jupiter CoRoT-1b, the faintest (K=12.2) host star for which the planet has been spectroscopically

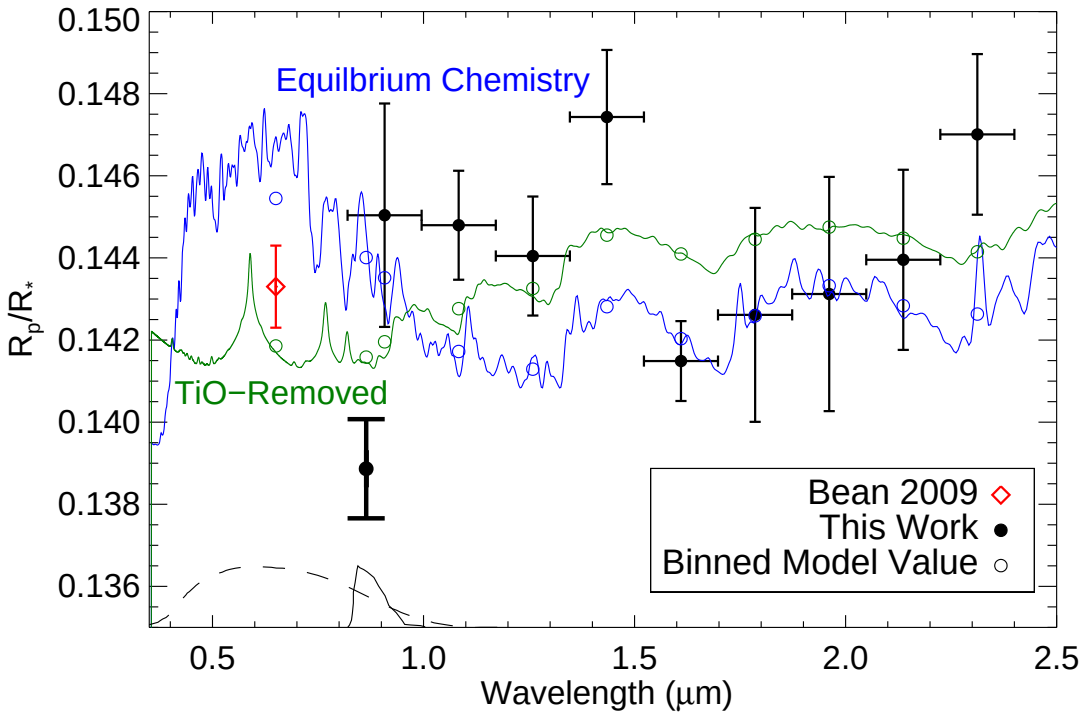

Figure 3.11: Measured planet-to-star radius ratio spectrum compared to a 2500 K isothermal model (blue) from (Fortney et al., 2010) with no clouds or hazes but significant TiO/VO absorption. Black data points are the weighted average IRTF data for three transits with spectral data in thin lines and photometry data in thick lines. The red point is the CoRoT value from 36 transits (Bean, 2009). Y error bars represent 1σ uncertainties whereas X error bars span spectral windows, except in the cases of photometric data. Photometric filter curves that are normalized to unity and scaled to 1/10 of the figure are shown in with black lines for the CoRoT planet finder response (dashed line) and the MORIS z' filter (solid line). The IRTF data (black) combined with the CoRoT point (red) disfavor the TiO/VO-driven optical to infrared absorption slope and give a χ^2 per degree of freedom of 4.6 as compared to a χ^2 of 2.4 per degree of freedom for the same model with TiO removed (green).

characterized to date. With the MOS method and a single nearby simultaneous reference star, we achieve 0.03% to 0.09% precision of the transit depth R_p^2/R_*^2

when combining all three nights of data, comparable to one atmospheric scale height for this hot Jupiter's temperature. We conclude the following items from our analysis:

- The IRTF spectrum, when combined with the optical planet-to-star radius ratio derived from observations by the CoRoT spacecraft (Bean, 2009), disfavors a model that includes TiO/VO as compared to a model that is spectrally flat or has TiO removed. This goes against the prediction that CoRoT-1b's thermal inversion is due to TiO/VO absorption. Other recently characterized hot Jupiters with similarly high temperatures, WASP-19b and WASP-12b, also lack strong TiO/VO (Anderson et al., 2013; Sing et al., 2013) features, but TiO/VO is expected to be depleted in these planets because they have no observed temperature inversions.
- No statistically significant molecular features are seen in the 0.8 μm to 2.4μm transmission spectrum, although there is a small 2σ peak at 1.4 μm, possibly due to H_2C_2 or HCN. Our precision is not high enough to constrain the detailed composition of H_2O, CO, and other gases due to the systematics and faintness of the host star.
- The Gaussian process method for determining systematics and the baseline achieves better precision in extracted parameters and more robustness when applied to the half-transit on Dec 29, 2011 as compared to a deterministic polynomial baseline. For data sets with strong out-of-transit curvature, the Gaussian Process model can give significantly different results from a polynomial baseline.

3.6 Acknowledgements

This research was funded in part by the New York/NASA Space Grant Fellowship. Based on observations made from the Infrared Telescope Facility, which is operated by the University of Hawaii under Cooperative Agreement no. NNX-08AE38A with the National Aeronautics and Space Administration, Science Mission Directorate, Planetary Astronomy Program. M.Z. is supported by the Center for Exoplanets and Habitable Worlds at the Pennsylvania State University. Thanks to Eva-Maria Mueller and Joyce Byun for useful MCMC suggestions. The authors wish to recognize and acknowledge the very significant cultural role and reverence that the summit of Mauna Kea has always had within the indigenous Hawaiian community. We are most fortunate to have the opportunity to conduct observations from this mountain. We also thank the anonymous referee for useful comments and corrections.

3.7 Appendix: Simulated Series

In order to compare an autocovariance of residuals to an input kernel, it is illustrative to show the autocovariance of some simulated time series. Figure 3.12 shows simulations for the best-fit hyper-parameters from the 1.79 μm, 1.43 μm and z' light curves on the night of January 04, 2012. The two autocovariance plots of the residuals are shown in Figure 3.7

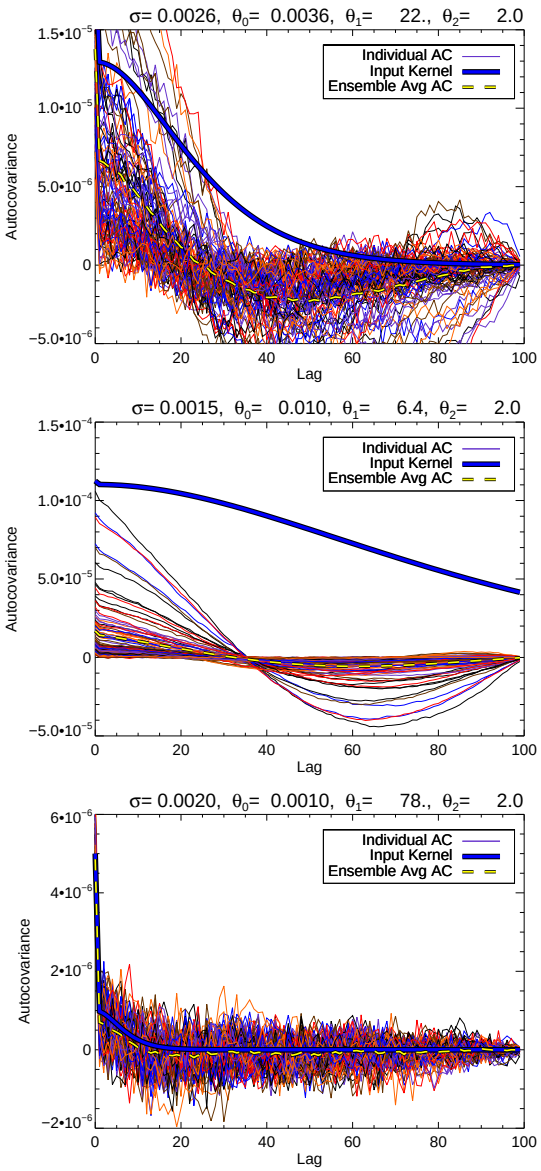

Figure 3.12: Autocovariance estimators of simulated time series for a given kernel (solid blue line) and hyper-parameters given in the title. The individual colored thin lines show different realizations of the same covariance kernel and the average is shown as a dotted yellow line. The ensemble average is not equal to the kernel function because the autocovariance estimator is a biased estimator of the true autocovariance (Wei, 2006).

BIBLIOGRAPHY

Abe, L. et al. 2013, A&A , 553, A49, 1303.0973

Anderson, D. R. et al. 2013, MNRAS , 430, 3422, 1112.5145

Astudillo-Defru, N., & Rojo, P. 2013, ArXiv e-prints, 1306.5475

Barge, P. et al. 2008, A&A , 482, L17, 0803.3202

Bean, J. L. 2009, A&A , 506, 369, 0903.1845

Bean, J. L., Désert, J.-M., Seifahrt, A., Madhusudhan, N., Chilingarian, I., Homeier, D., & Szentgyorgyi, A. 2013, ApJ, 771, 108, 1303.1094

Bean, J. L., Miller-Ricci Kempton, E., & Homeier, D. 2010, Nature , 468, 669, 1012.0331

Birkby, J. L., de Kok, R. J., Brogi, M., de Mooij, E. J. W., Schwarz, H., Albrecht, S., & Snellen, I. A. G. 2013, ArXiv e-prints, 1307.1133

Burrows, A., & Orton, G. 2009, ArXiv e-prints, 0910.0248

Carter, J. A., & Winn, J. N. 2009, ApJ, 704, 51, 0909.0747

Charbonneau, D., Brown, T. M., Noyes, R. W., & Gilliland, R. L. 2002, ApJ, 568, 377, arXiv:astro-ph/0111544

Crossfield, I. J. M., Barman, T., Hansen, B. M. S., Tanaka, I., & Kodama, T. 2012, ApJ, 760, 140, 1210.4836

Deming, D. et al. 2011, ApJ, 726, 95, 1011.1019

——. 2013, ApJ, 774, 95, 1302.1141

Demory, B.-O. et al. 2013, ApJ, 776, L25, 1309.7894

Evans, T. M. et al. 2013, ApJ, 772, L16, 1307.3239

Fortney, J. J., Lodders, K., Marley, M. S., & Freedman, R. S. 2008a, ApJ, 678, 1419, 0710.2558

Fortney, J. J., Marley, M. S., Saumon, D., & Lodders, K. 2008b, ApJ, 683, 1104, 0805.1066

Fortney, J. J., Shabram, M., Showman, A. P., Lian, Y., Freedman, R. S., Marley, M. S., & Lewis, N. K. 2010, ApJ, 709, 1396, 0912.2350

Gibson, N. P., Aigrain, S., Barstow, J. K., Evans, T. M., Fletcher, L. N., & Irwin, P. G. J. 2013a, MNRAS , 428, 3680, 1210.7798

——. 2013b, MNRAS , 436, 2974, 1309.6998

Gibson, N. P. et al. 2012a, MNRAS , 422, 753, 1201.6573

Gibson, N. P., Aigrain, S., Roberts, S., Evans, T. M., Osborne, M., & Pont, F. 2012b, MNRAS , 419, 2683, 1109.3251

Gillon, M. et al. 2009, A&A , 506, 359, 0905.4571

Gulbis, A. A. S. et al. 2011, PASP , 123, 461, 1102.5248

Hartman, J. D. et al. 2011, ApJ, 742, 59, 1106.1212

Hebb, L. et al. 2009, ApJ, 693, 1920, 0812.3240

——. 2010, ApJ, 708, 224, 1001.0403

Hubeny, I., Burrows, A., & Sudarsky, D. 2003, ApJ, 594, 1011, arXiv:astro-ph/0305349

Huitson, C. M. et al. 2013, ArXiv e-prints, 1307.2083

Knutson, H. A., Benneke, B., Deming, D., & Homeier, D. 2014, Nature , 505, 66

Knutson, H. A., Howard, A. W., & Isaacson, H. 2010, ApJ, 720, 1569, 1004.2702

Kreidberg, L. et al. 2014, Nature , 505, 69, 1401.0022

Line, M. R., Knutson, H., Deming, D., Wilkins, A., & Desert, J.-M. 2013a, ApJ, 778, 183, 1310.4796

Line, M. R. et al. 2013b, ApJ, 775, 137, 1304.5561

Madhusudhan, N. 2012, ApJ, 758, 36, 1209.2412

Madhusudhan, N. et al. 2011a, Nature , 469, 64, 1012.1603

Madhusudhan, N., Mousis, O., Johnson, T. V., & Lunine, J. I. 2011b, ApJ, 743, 191, 1109.3183

Mancini, L. et al. 2013, ArXiv e-prints, 1306.6384

Mandel, K., & Agol, E. 2002, ApJ, 580, L171, arXiv:astro-ph/0210099

Mandell, A. M., Haynes, K., Sinukoff, E., Madhusudhan, N., Burrows, A., & Deming, D. 2013, ApJ, 779, 128, 1310.2949

Moses, J. I., Madhusudhan, N., Visscher, C., & Freedman, R. S. 2013, ApJ, 763, 25, 1211.2996

Moses, J. I. et al. 2011, ApJ, 737, 15, 1102.0063

Öberg, K. I., Murray-Clay, R., & Bergin, E. A. 2011, ApJ, 743, L16, 1110.5567

Pont, F., Sing, D. K., Gibson, N. P., Aigrain, S., Henry, G., & Husnoo, N. 2013, MNRAS , 432, 2917, 1210.4163

Pont, F., Zucker, S., & Queloz, D. 2006, MNRAS , 373, 231, astro-ph/0608597

Rasmussen, C. E. & Williams, C. K. I. 2006, Gaussian Processes for Machine Learning (The MIT Press)

Rayner, J. T., Toomey, D. W., Onaka, P. M., Denault, A. J., Stahlberger, W. E., Vacca, W. D., Cushing, M. C., & Wang, S. 2003, PASP , 115, 362

Rogers, J. C., Apai, D., López-Morales, M., Sing, D. K., & Burrows, A. 2009, ApJ, 707, 1707, 0910.1257

Schlawin, E., Zhao, M., Teske, J. K., & Herter, T. 2014, ApJ, 783, 5, 1401.3337

Sing, D. K. et al. 2011, A&A , 527, A73, 1008.4795

——. 2012, MNRAS , 426, 1663, 1208.4982

——. 2013, ArXiv e-prints, 1309.5261

Skrutskie, M. F. et al. 2006, AJ, 131, 1163

Snellen, I. A. G., de Kok, R. J., de Mooij, E. J. W., & Albrecht, S. 2010, Nature , 465, 1049, 1006.4364

Spiegel, D. S., & Burrows, A. 2012, ApJ, 745, 174, 1108.5172

Stevenson, K. B., Bean, J. L., Seifahrt, A., Desert, J.-M., Madhusudhan, N., Bergmann, M., Kreidberg, L., & Homeier, D. 2013, ArXiv e-prints, 1305.1670

Swain, M. et al. 2013, Icarus, 225, 432, 1205.4736

Swain, M. R., Vasisht, G., & Tinetti, G. 2008, Nature , 452, 329

Teske, J. K., Schuler, S. C., Cunha, K., Smith, V. V., & Griffith, C. A. 2013, ApJ, 768, L12

Tody, D. 1986, in Society of Photo-Optical Instrumentation Engineers (SPIE) Conference Series, Vol. 627, Society of Photo-Optical Instrumentation Engineers (SPIE) Conference Series, ed. D. L. Crawford, 733

Tody, D. 1993, in Astronomical Society of the Pacific Conference Series, Vol. 52, Astronomical Data Analysis Software and Systems II, ed. R. J. Hanisch, R. J. V. Brissenden, & J. Barnes, 173

Vidal-Madjar, A., Lecavelier des Etangs, A., Désert, J., Ballester, G. E., Ferlet, R., Hébrard, G., & Mayor, M. 2003, Nature , 422, 143

Visscher, C., & Moses, J. I. 2011, ApJ, 738, 72, 1106.3525

Wei, W. 2006, Time series analysis: univariate and multivariate methods (Pearson Addison Wesley)

Zahnle, K., Marley, M. S., Freedman, R. S., Lodders, K., & Fortney, J. J. 2009, ApJ, 701, L20, 0903.1663

Zhao, M., Monnier, J. D., Swain, M. R., Barman, T., & Hinkley, S. 2012, ApJ, 744, 122, 1109.5179

CHAPTER 4

REDUCED OPTICAL ACTIVITY AND LARGE PARTICLES FROM THE DISINTEGRATING PLANET CANDIDATE KIC 12557548B

The intriguing exoplanet candidate KIC 12557548b has a comet-like tail of dusty debris trailing a small rocky planet. It is expected that the central body is a sub-Mercury planet that was once larger and has lost mass through disintegration. The tail of debris absorbs up to 1.3% of the stellar light in the Kepler observatory's bandpass (0.42 μm to 0.9 μm) and extends behind the planet by a few stellar radii. KIC 12557548b is the first of a few disintegrating planets found outside the solar system. Observing the tail's transit depth at multiple wavelengths can reveal the composition and particle size of the debris, constraining the makeup and lifetime of the sub-Mercury planet. Early dust particle size predictions from the scattering of the comet-like tail pointed towards a dust size of ~0.1μm. These small particles would produce a much deeper optical transit depth than near-infrared transit depth. We measure a transmission spectrum for KIC 12557548b using the SpeX spectrograph and MORIS imager on the Infrared Telescope Facility from 0.8 μm to 2.4 μm with simultaneous r' (0.63 μm) photometry and one night in H band (1.63 μm) using the Wide-Field IR Camera at the Palomar 200-inch telescope. The infrared spectra are plagued by systematic errors, but sufficient precision is obtained when using differential spectroscopic calibration. The average differential transmission spectrum is flat, supporting findings that KIC 12557548b's debris is likely composed of larger particles $\gtrsim$ 0.5μm. The r' photometry is more stable with all transit depths below the average Kepler value, suggesting that the observations occurred during a weak period or that the mechanisms producing optical broadband transit depths are

suppressed.

4.1 Introduction

Analysis of public data from the Kepler mission (Borucki et al., 2010) uncovered the exotic KIC 12557548 system, which contains a disintegrating rocky planet candidate ($\lesssim 0.1 M\oplus$) with an orbital period of 15.7 hours (Rappaport et al., 2012). The planet's escaping debris cause a variable ($\lesssim$0.2% to 1.3%) broadband optical absorption with a constant period, unlike any of the thousands of previously discovered transiting exoplanets. The large optical transit depths of the disintegrating debris are in contrast to escaping winds from hot Jupiters, which are transparent in broadband optical light and can only be detected at narrow gaseous absorption lines (e.g. Vidal-Madjar et al., 2003). The broadband spectral nature of the atmospheric absorption indicates that the material is composed of solid particles. The long duration of the transit compared to a planetary crossing time indicates that it has a tail of debris longer than the diameter of its host star. Furthermore, the discoveries of KOI 2700b (Rappaport et al., 2014) and EPIC 201637175b (Sanchis-Ojeda et al., 2015) reveal that there are multiple planets with tails of dusty effluents and more may be discovered around nearby stars. These disintegrating planets provide an exciting promise for characterizing the cores of planets that are inaccessible in the solar system and complement the studies of planet composition using the pollution of white dwarf atmospheres, which characterizes the end state of planetary accretion of the bulk of an entire planet onto evolved stars (e.g. Jura, 2003).

The destruction mechanism proposed by Rappaport et al. (2012) and Perez-Becker & Chiang (2013) to explain the tail of solid debris is that a hy-

drodynamic wind of a metal-rich vapor condenses into grains after adiabatic cooling. The calculated mass loss rate suggests that KIC 12557548b may be in the catastrophic end state of its life, which will destroy it entirely (Perez-Becker & Chiang, 2013). Stellar activity may factor into the planet's destruction – the deepest transit depths tend to coincide with times at which the star spots face our line of sight and shallow transit depths occur when the stellar spots are rotated out of our line of sight (Kawahara et al., 2013). The transit depth traces the disintegrating activity directly as the planet's physical radius is too small to contribute more than 10^{-5} to the average 10^{-2} transit depth. This correlation has been confirmed with additional Kepler data, but there is also the possibility that occultations of star spots by the comet's tail affect the transit depth (Croll et al., 2014b).

The average Kepler light curve of KIC 12557548 over 2000 transits is a diagnostic tool for measuring the properties and grain sizes of KIC 12557548b's debris. Prior to the flux decrement (transit), there is a small flux increase due to scattering of dust particles into the line of sight. The flux increase is sensitive to dust particle size, and models matching the flux increase are consistent with Mie-scattering from small dust grains (~ 0.1 μm) (Budaj, 2013; Brogi et al., 2012). Budaj (2013) modeled the light curve as Mie-scattering and absorption from spherical pyroxene and iron dust grains 0.01μm to 1μm in radius. The models with 0.1 μm to 1.0 μm grains fit the beginning of the average Kepler light curve better whereas the models with 0.01 μm to 0.1 μm grains fit the egress better, suggesting that larger particles either are ejected or form near the planet and get whittled down as they progress along the tail. Brogi et al. (2012) model the scattering of dust particles with a Henyey-Greenstein phase function and find similar size particles, with a best-fit power law grain size distribution from

0.04μm to 0.19μm. KIC 12557548b's tail length also constrains the particle size and dust composition because the tail length is a strong function of the sublimation time of dust particles. van Lieshout et al. (2014) estimate the sublimation timescales for a variety of dust compositions and sizes and find that only 10μm Corundum and 100μm or larger silicates can have the right sublimation times at KIC 12557548b's orbital radius to reproduce the observed tail length.

A multi-wavelength simultaneous light curve provides additional diagnostics of the planet's escaping transiting debris because the scattering and absorption of dust particles is highly wavelength dependent when the wavelengths become larger than the size of the particles (e.g. Draine, 2011). Croll et al. (2014a) obtained simultaneous Kepler (~0.65μm) and K_S-band (2.15μm) light curves for two separate epochs and compared the transit depths. Both the 0.65μm and 2.15μm light curves were consistent within errors, giving evidence for particle sizes $\gtrsim$ 0.5μm.

The size of particles escaping a disintegrating planet can change with time, so studies at different epochs may give different results. Bochinski et al. (2015) find that the spectral slope of the debris cloud changes between two nights of observation. The spectral slope between the u', g' and z' bands of a deep transit is consistent with interstellar medium reddening laws for (0.25μm to 1μm) particles, whereas the weaker transit had a flatter spectral energy distribution, which would be expected for larger grains. Similarly, spectra of three different transits of EPIC 201637175b (Sanchis-Ojeda et al., 2015) show that the spectral slope during the deep transit is consistent with dust particles $\sim$ 0.2μm to $\sim$ 0.4μm in size, and the two weaker transit events are spectrally flat and consistent with larger-sized dust particles.

We observed the disintegrating system KIC 12557548b over 8 transits with the SpeX spectrograph and MORIS imager on the Infrared Telescope Facility (IRTF), covering the wavelengths from 0.6 μm to 2.4 μm, to give additional constraints on the particle sizes escaping from KIC 12557548b. Section 4.2 describes our observations, where we show that the optical transit depths are all weaker than the average Kepler value and that the infrared spectrum is flat. Section 4.3 describes our fitted transmission spectrum, which is best fit by large particles $\gtrsim$ 0.5μm. We conclude in Section 4.4, and also consider different ways to average the variable spectra in Section 4.6.

4.2 Observations

We observed 8 transits of KIC 12557548b with a simultaneous reference star (2MASS J19234770+5130175) to correct for telluric, detector and instrument systematics. This is the same general observational setup used when obtaining a transmission spectrum of the hot Jupiter CoRoT-1b Schlawin et al. (2014), but there are a few noteworthy differences. The Kepler observatory (0.423 μm to 0.897 μm bandpass Koch et al., 2010) halted photometry after a reaction wheel failure, so for KIC 12557548 we used the MORIS imager (Gulbis et al., 2011) in the r' band (0.542 μm to 0.693 μm) to give optical information simultaneously with the SpeX infrared wavelengths 0.8μm to 2.4μm, shown in Figure 4.1. KIC 12557548 (K =13.32) and its reference star J19234770+5130175 (K=14.00, as determined by 2MASS Skrutskie et al., 2006), are both fainter than CoRoT-1 (K=12.15) and its nearby reference star (K=11.50) meaning that the minimum photon-limited noise floor is higher and that background subtraction plays a larger role in the spectral extraction. The KIC 12557548 system is overall more

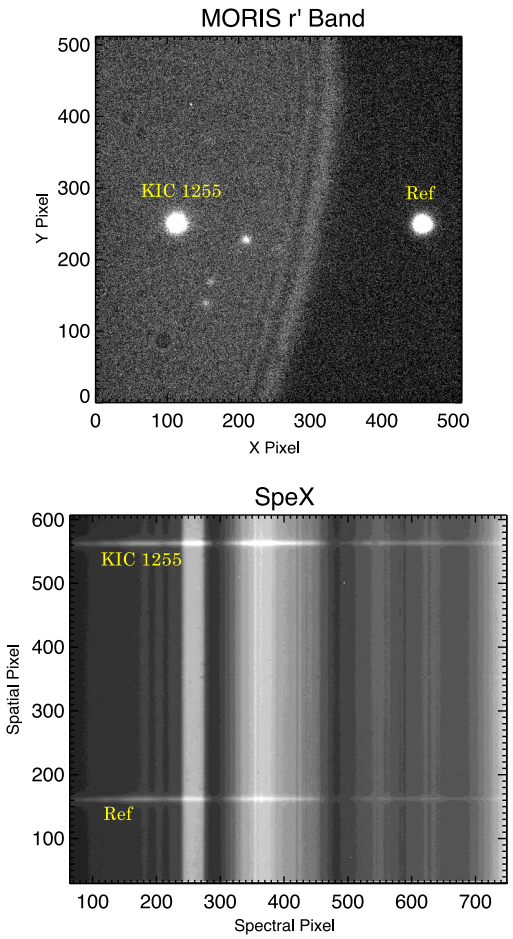

Figure 4.1: *Top* Example raw MORIS image, showing an arc of emission that is likely a reflection off the foil that reduces the emissivity of the IRTF telescope. The contrast of the arc emission has been emphasized in this image for visual purposes although it is a small fraction of the stellar flux. *Bottom* Example SpeX image after rectifying all wavelengths for background subtraction.

challenging to achieve high precision on due to its faintness and the fact that the transit depths are variable, so multiple nights must be acquired to ensure transit detection.

The reference star, 2MASS J19234770+5130175, shown in Figure 4.1, is 39″ away from KIC 12557548, so that both can lie in the 60″ long slit with more than

5″ of baseline for background subtraction. The upper baseline (in Figure 4.1) is shorter for KIC 12557548 (5″) than for the reference star (16″) because the stars must be displaced upward on the SpeX array in order to fit both on the MORIS detector. In addition to this spatial baseline for background subtraction, the light curves require time baselines on either side of transit to fit the normalized out-of-transit flux. We obtained 0.5 to 2.6 hours of baseline on either side with an average of 1.4 hours, comparable to the ~1.4 hour transit duration where the average Kepler light curve drops below 99.95%. The seeing varied between all the nights, as shown in Table 4.1, but was always smaller than 1/3 of the 3 arcsecond slit width. Furthermore, care was taken to align the two stars within the slit so that they were less than 0.1 arcsec displaced in the dispersion direction to minimize differential slit loss between KIC 12557548 and its reference star.

The 8 transits are spread over many nights, spatial positions, detectors and potential disintegration activity of the planet. The four observations in 2013 on UT August 13, 15, 17 and UT September 3 were followed by a SpeX detector upgrade from a Aladdin InSb detector to a Hawaii-2RG with lower read noise. The new Hawaii-2RG is sensitive to alpha particles emitted by a Thorium-containing coating within the SpeX instrument but they are easily excluded with 5σ clipping in the spatial profile fitting and time series. All 2013 observations were interrupted by a telescope guiding jump subsequently determined to be due to a chopping mirror; these jumps were avoided in 2014. The interruptions in 2013 were corrected for within 10 minutes, with the exception of UT August 17, which also suffered a telescope guiding issue that had to be corrected at zenith, visible in Figure 4.2. In 2014, we observed the transit on UT August 14, August 18, September 2 and September 4 with no guiding interruptions, good seeing and lower read noise in the newer Hawaii-2RG detector. We also observed the

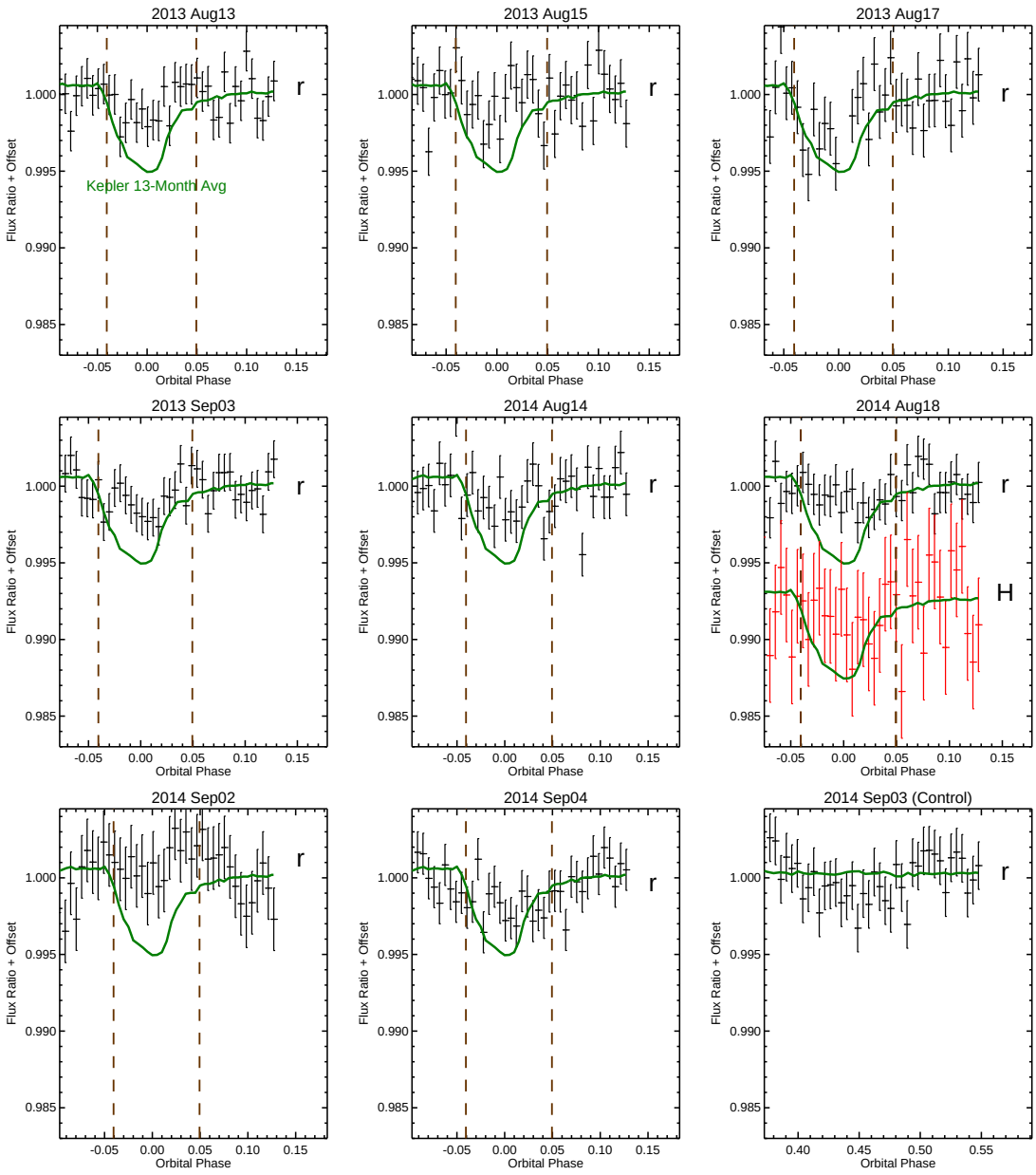

Figure 4.2: The time series in the r' (0.63μm) filter of the MORIS camera (black points with error bars) and H band filter of the WIRC cameras show transit depths that are weaker than the average short cadence Kepler light curve (green). The vertical dashed lines mark approximate start and end of the transit (using the points where the average Kepler light curves falls below 99.95%).

UT Date	t_{spec} (s)	t_{phot} (s)	1.6μm Seeing (arcsec)
August 13, 2013	75	5	0.5
August 15, 2013	75	5	1.0
August 17, 2013	75	5	0.6
September 03, 2013	75	5	0.4
August 14, 2014	60	10	1.0
August 18, 2014	60	20	0.8
September 2, 2014	60	20	0.6
September 4, 2014	60	20	0.5
(Out of Transit)			
September 3, 2014	60	20	0.5

Table 4.1: Summary of the 8 transits and 1 out-of-transit nights, with the exposure time for SpeX spectra t_{spec}, MORIS photometric exposure time t_{phot} and FWHM median seeing in arc seconds measured across the infrared wavelengths from 0.9μm to 2.3μm.

same system on UT September 3, 2014 when it was outside of transit to quantify the light curve systematics over 3 hours and to use as a control.

The simultaneous MORIS imager r' band photometry is achieved with a 0.8 μm dichroic to split off short wavelengths while still passing the infrared light to the spectrograph. The field of view of MORIS is 1′ x 1′, similar to that of the guide camera of SpeX and it permitted us to include the same reference star (2MASS J19234770+5130175) on the MORIS detector. We used exposures of 5s in 2013 and later increased to 10 - 20s in 2014 to reduce seeing and scintillation noise (Table 1). The camera was kept in focus throughout the observations (as opposed to a purposeful de-focusing technique, eg., Southworth et al., 2009) due to KIC12557548's faintness and the fine pixel sampling of MORIS (0.12″/pixel).

Photometric data reduction was carried out following the pipeline and steps of Zhao et al. (2012). We found that an aperture size of 28 pixels in diameter

(corresponding to 3.4″) and a 35-pixel wide background annulus provided the lowest out-of-transit scatter in the light curves for all 2013 nights, although aperture sizes with ±3 pixels gave the same results. In 2014, the reference star was closer to the edge of the MORIS detector because we moved the stars to a a cleaner part of the 3″× 60″ slit for SpeX. Thus, a different method was required to extract photometry. We divided KIC 12557548 by the reference star and extracted photometry on the difference image normalized by the photometry on the reference star. This allowed a similar level of precision as in 2013 but using a 30 pixel aperture diameter and only a 14 pixel wide background annulus, separated from the aperture by 4 pixels. A non-uniform background illumination (a 1% step in background brightness going from the reference star to target star with a peak at the intersection, visible in Figure 4.1) plagued the MORIS camera on all nights. The likely cause of this non-uniform background is a specular reflection from a bright star. The structure in the background moves during the night but the step in brightness remains between the stars, so that the background is relatively uniform surrounding each star when performing aperture photometry. This background structure is not visible in the infrared slit viewer within SpeX nor the spectrograph, likely because it is mitigated by baffling or the cold pupil stop in SpeX.

On UT August 18, 2014, we also simultaneously observed a transit of KIC 12557548b with the Palomar Hale 200-inch telescope and its Wide-field Infra Red Camera (WIRC) (Wilson et al., 2003) in the *H* band. We used an engineering-grade HAWAII-2 array with a field of view of 8.7′ × 8.7′ for the observation[1]. We followed the well-established precision photometry procedures

[1]The original science grade H2 array failed in April 2014. The engineering grade array has much lower well depth, more hot/bad pixels, and one less-responsive quadrant, but is nonetheless sufficient for this study due to the faintness of the target and enough reference stars nearby.

for WIRC and "stared" at the target throughout the observation (e.g., Zhao et al., 2012, 2014). We took 30s exposures and kept the telescope focused due to the faintness of the target and the high background. For the same reason, we also took sky background immediately before and after the observation to construct a normalized "supersky" for sky subtraction in the reduction, which was turned out to be necessary. We followed the data reduction steps outlined in Zhao et al. (2014), and used 6 stars with fluxes in the range of 0.6 – 2× that of the target in the good part of the detector as references. A photometry aperture of 5″ and a background annulus from 6.3″ to 10″ resulted in the best light curve precision.

The optical transit depths, as measured by MORIS, are much smaller than the past behavior for the planet as determined by the Kepler observatory, as shown in Figure 4.2. The r' band transit depths for 8 nights are *all* less than 0.43%, whereas the *average* Kepler value is 0.504%. If we assume transits are all statistically independent and have a probability distribution function as given in van Werkhoven et al. (2014), the probability of 8 transits less than 0.43% is 0.2% (the equivalent of a 3.2 σ event in a Gaussian distribution), suggesting that the activity fell into the weaker periods found by Kepler or that it changed after May 2013, when the Kepler observatory stopped monitoring KIC 12557548. KIC 12557548b was observed by the Kepler observatory to have ~20 day intervals of weak activity with shallow transit depths ($\lesssim$ 0.2%) (van Werkhoven et al., 2014). However, it would be unlikely that the observations in both 2013 and 2014 would fall into weak transit intervals as there were only two 20 day weak activity intervals in 3.7 years of monitoring in the 15 quarter analysis by van Werkhoven et al. (2014).

The processing pipeline for the SpeX spectrograph used in Schlawin et al.

(2014) was improved to handle the relatively larger background-to-source brightness. The spectrograph images (prior to extraction) were rectified so that each column corresponds to one wavelength (see Figure 4.1), but instead of using an Argon lamp spectrum for the straightening, the background spectrum was cross-correlated with a master image to account for the slight differences in illumination and flexure between the Argon lamp and sky image. We dark-subtracted each frame and flat-fielded using a sky flat to fit the non-uniform transmission of the reflective 3″× 60″ slit and a filtered lamp image to remove the pixel-to-pixel responsiveness variations. The sky flats were shifted to account for the flexure of the instrument. The image rectification and sky flat fields improved background subtraction while still using a simple 4th-order background fit including all pixels more than 3.7 arcseconds from the source on either side.

We employed a custom optimal extraction based on the method of Horne (1986), to increase control of the spatial profile polynomial fit and we use the standard deviation of the background fit residuals for empirical estimation of background and read noise. We use a 7 arcsecond aperture, which is well above the seeing for all nights (0.5 to 1 arcsec in the infrared, listed in Table 4.1). We tested aperture sizes from 5 to 10″ with little effect on the results because optimal extraction weights the core of the PSF more than the wings. This pipeline is checked on CoRoT-1b transit data (Schlawin et al., 2014) and produces consistent results, but the improvements are less important for the higher signal-to-background ratio of the CoRoT-1b observations.

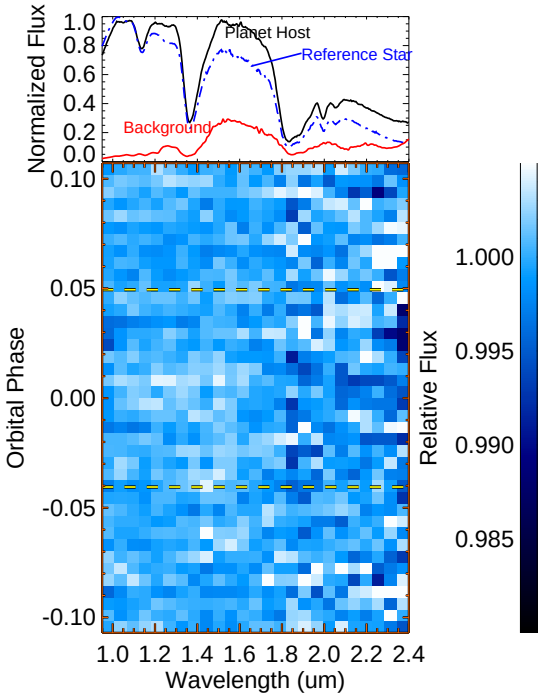

Figure 4.3: *Top Panel* Normalized KIC 12557548, reference star and background spectra showing where the signal to noise drops because of telluric (Earth's) absorption and background emission. *Bottom Panel* Dynamic differential spectrum for the combined 6 nights of transit with 25 wavelength bins and 5σ clipping to remove cosmic rays, alpha particle hits and large systematics. There is no statistically differential transit at a phase of 0.0.

4.3 Differential Dynamic Spectrum

There are substantial common-mode (affecting all wavelengths) systematics affecting the SpeX detector on most nights, including August 18, 2014 where we obtained simultaneous *H* WIRC photometry. For this night, the *H* band transit depth is 0.19 ± 0.11 % consistent with the *r'* depth of 0.07% ± 0.06% whereas the SpeX spectra binned to the same wavelengths as *H* band (1.48 to 1.78 μm) give 1.26 ± 0.18%. The rest of the wavelengths measured by the SpeX spectrograph are also 1.3% to within errors, suggesting that it has a common-mode

systematic. There are fluctuations in the broadband transit depth measured by the SpeX instrument, going from a strong flux decrease during transit on August 15, 2013 to a flux increase during transit on August 17, 2013. We therefore analyze the SpeX data in a differential way by dividing all light curves by the binned broadband time series (differential spectra). The absolute spectra, alternate averaging methods and transit injection tests are explored in Appendix 4.6.

The systematics present in the absolute SpeX time series that occurred for KIC 12557548 but not CoRoT-1b (Schlawin et al., 2014) were surprising, so we performed numerous tests on the data to ascertain the best averaging and analysis methods. Most spectroscopic exoplanet observations are affected by systematics like detector ramps (e.g. Crossfield et al., 2012b), detector non-linearity (e.g. Gibson et al., 2012), variable slit loss (e.g. Sing et al., 2012) and telluric absorption (e.g Crossfield et al., 2012a), some of which can be calibrated out and others not. We searched the SpeX observations for evidence of differential slit loss, specks on the reflective slit substrate, non-linearity, detector anomalies, guiding errors, background variations, stray light, spectral shifting, insufficient OH airglow subtraction, sum versus optimal extraction, extraction aperture size, background fitting order, background fitting regions, flat field errors, telluric absorption lines, correlations with airmass and telescope flexure. None of these tests resulted in robust correlations with the observed anomalies. However, the control night of September 3, 2014 suggests that non-astrophysical variations are possible during transit. We fit the light curves on this control night in the same manner as Section 4.3.1 as if it were a real transit. We find that for the five wavelength channels, the transit depths deviate from zero – see Appendix 4.6. We therefore choose to fit differential spectra and combine data from multi-

ple nights to derive the planet system's transmission spectrum.

Figure 4.3 shows the differential dynamic spectrum surrounding mid-transit of KIC 12557548b where the 5 nights for which MORIS transit depths were greater than 0.1% (August 13, 2013, August 17, 2013, September 03, 2013, August 14, 2014 and September 04, 2014) are combined into 25 wavelength bins and 5.4 minute time bins. The broadband behavior is divided out to remove common-mode systematics. The orbital phase is centered on a reference epoch of BJD=2454833.039, the flux minimum of the average Kepler light curve using the publicly available data. The approximate transit start and end (where the flux drops below 99.95% of the out-of-transit flux as measured in the average Kepler transit profile) are shown as horizontal dashed lines. The different nights are averaged with 5σ clipping from the median to remove bad pixels, cosmic ray hits and the alpha particle hits caused by a Thorium anti-reflective coating within SpeX. The differential dynamic spectrum shows no statistically significant deviations from a flat spectrum.

4.3.1 Light Curve Fitting

We averaged all available short cadence Kepler data (quarters 13 through 17 or 13 months) in order to construct a light curve model. We phased the light curve at an orbital period of P=0.6535538 days (van Werkhoven et al., 2014) and binned the data into time samples of 9.4 minutes (0.01 in orbital phase), which results in median errors of 0.005%, well below the measured precision of SpeX or MORIS. There are still small residuals in the curve, visible out of transit in Figure 4.2 for September 3, 2014.

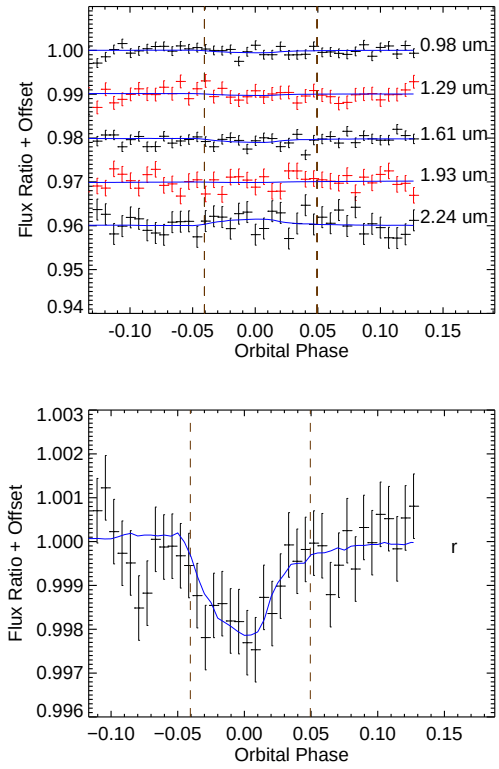

Figure 4.4: *Top:* The time series for five equally spaced wavelength spectroscopic bins separated into 40 equally spaced time bins, 5.4 minutes each over the 5 nights with the largest MORIS transit depths. Each time series is divided by the broadband light curve to remove common-mode systematics. The average Kepler short cadence light curve (KSC) is used as a model (solid lines) with a free parameter for the scaling of the transit depth and two free parameters for the linear baseline. Red/black colors are alternated between wavelengths to distinguish overlapping time series.
Bottom: The MORIS r' photometry ($\sim$ 0.56 to 0.69μm) for the 5 deeper transit depth nights is still about half the average from the KSC curve.

We fit each time series for each night individually using this average Kepler Short Cadence light curve (KSC), but scaled from its out-of-transit value by a free parameter. We bin the spectrum into five wavelength bins to improve the signal to noise for model fitting. We also include a linear baseline (fit simul-

taneously with the model as in Schlawin et al. (2014)) to account for long term trends. The transit epoch is fixed at a constant-period ephemeris with mid-transit at 2454833.039 BJD, the minimum of the Kepler short-cadence average light curve. We also confirmed that the average MORIS light curve is consistent with this ephemeris within errors when the epoch is left as a free parameter. Error bars in the time series are calculated as the standard deviation of the flux out of transit. These are propagated to transit depth scaling with a numerical covariance matrix using the routine `mpfit` (Markwardt, 2009). We down-selected the 5 nights with transit depths above 0.1% as measured by the MORIS camera in r' band to use for light curve analysis. Illustrative fits are shown in Figure 4.4 for the average time series of these nights both for the differential time series and the photometric light curve. The individual extracted spectra, shown in Figure 4.5, are within errors of each other and show no consistent trend with wavelength.

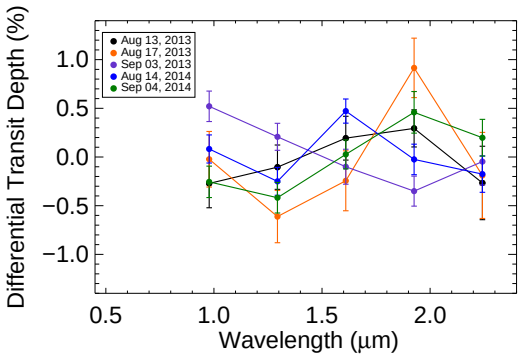

Figure 4.5: Individual differential spectra are found from the SpeX data covering the 5 nights with the strongest transit depths as measured by the MORIS camera in the r' band. The transit depth and errors are found by scaling the average Kepler Short Cadence (KSC) curve to best fit the data. The individual spectra broadly agree to within errors.

In order to calculate the inferred dust particle sizes from the differential spectra, it is necessary to assume a mean value. We adopt the mean value equal to the average MORIS r' band transit depth for these 5 larger transit nights or 0.25 ± 0.03%. This assumption is based on (1) the fact the optical (0.42μm to 0.90μm) to infrared (2.15 μm) transit depth ratio is 1.02 ± 0.20 during two different transits (Croll et al., 2014a) (2) the measured spectrum is shown to be flatter during weaker transit events (Bochinski et al., 2015) and (3) our simultaneous optical (0.63μm) and H band (1.63 μm) measurement on August 18, 2014 are consistent with errors.

We combine the individual nights' spectra with a weighted average where the weights are proportional to the $1/\sigma^2$ where σ is the error in the transit depth. Next, we add the MORIS average r' transit depth of 0.25 ± 0.03% for the absolute offset. The resulting transmission spectrum is shown in Figure 4.6, with two sets of error bars. The set of solid error bars is from the out-of-transit standard deviation propagated through to transit depth and the average. The dashed error bars are a more conservative estimate from the scatter in the data to calculate the standard deviation of the mean.

The average spectrum shown in Figure 4.6 favors large particle sizes, in contrast to our initial prediction that it would show strong wavelength dependence due to small particles. The forward scattering peak preceding transit is best fit by particle sizes of $\sim 0.1\mu$m (Budaj, 2013; Brogi et al., 2012), which have a pronounced drop in extinction from the optical to infrared wavelengths. Representative models are shown in Figure 4.6 for a single-particle size distribution of spherical Mg-rich pyroxene grains. The model with a nominal 0.1μm median particle size (blue curve in Figure 4.6) is disfavored by our data. For this model,

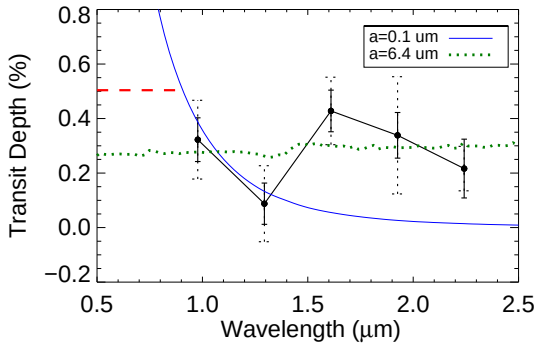

Figure 4.6: The average differential spectrum of KIC 12557548b from the individual nights shown in Figure 4.5. The two error bars are the error propagation method (solid lines) and from the scatter in the individual nights (dashed lines). The red dashed horizontal line shows the average transit depth measured by the Kepler observatory in the optical. Our r' photometry is far below the average Kepler value and the infrared spectrum is flat to within errors. Over-plotted are two example model spectra - one for a log-normal population of particles with a 0.1μm median radius and another for a larger 6.4μm median radius.

the reduced chi-squared, $\bar{\chi^2}$, is 10.6. Instead, a population of 6.4μm median radius grains (green dotted curve) better fits the data ($\bar{\chi^2}$ = 2.6). The models are described further in Section 4.3.2.

4.3.2 Inferred Particle Sizes

We compare measured spectra to Mie scattering models for different compositions of dust grains. The calculated transmission spectrum does not have a steep downward slope from the optical to infrared as would be expected from small (0.1μm-sized) particles, shown in Figure 4.6. To calculate the theoretical Mie spectra, we use the `IDL` Mie theory code `mie_single.pro` (Grainger et al.,

2004) to calculate the extinction as a function of wavelength. We assume that the debris escaping from KIC 12557548 is optically thin and input the complex indices of refraction from Dorschner et al. (1995) for pyroxene and olivine compositions. For the particle size distribution, we consider a broad log-normal function with particle number proportional to $\exp\left(-2\left(\ln(a) - \ln(\mu)\right)^2\right)$, where a is the particle radius and μ is the median of the distribution.

In Figure 4.7, we show the χ^2 statistic as a function of particle size for two different error estimates. For both error estimates and three different compositions: Mg-rich pyroxene ($MgSiO_3$), Fe-rich pyroxene ($Mg_{0.7}Fe_{0.3}SiO_6$) and olivine $MgFeSiO_4$ (Dorschner et al., 1995), the models with large dust particles better fit the data. For the errors propagated from the out-of-transit standard deviation in the time series, the lower limit on the particle sizes is 0.5 μm to 0.8 μm, depending on composition, for a Pearson's χ^2 test probability of 0.2% (equivalent of a 3 σ event in a normal distribution). On the other hand, if the conservative error estimate is taken from the scatter in the individual spectra from Figure 4.5, the same lower limit is 0.2 μm to 0.3 μm for the median of the lognormal particle size distribution.

The large particle sizes calculated from our transmission spectrum and the weak transit depths we observed for the 8 different nights spread over 2 years leave a few possible scenarios for KIC 12557548's lifetime. If the particle size distribution remains unchanged between strong transits and weak transits, then the large dust particles (also found by Croll et al. (2014a) during 2 strong transits) imply a short lifetime of the planet. If the particles are $\gtrsim 0.5\mu$m, then the mass loss rate of the system approaches $0.1M_\oplus$/Gyr (Perez-Becker & Chiang, 2013). For a maximum mass of $0.02M_\oplus$, the lifetime of the planet is less than

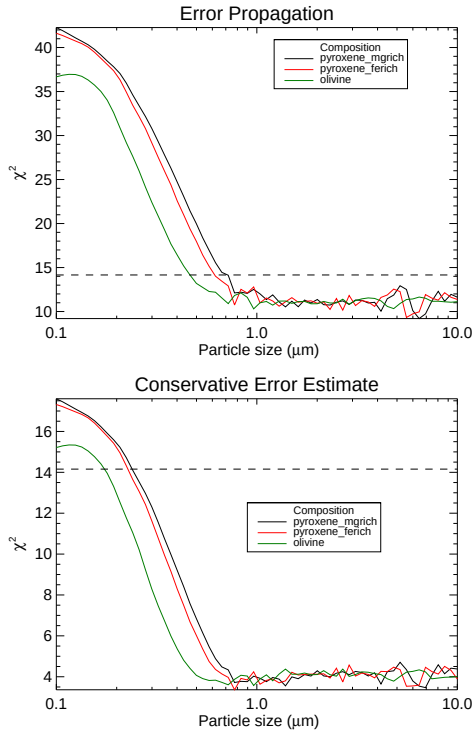

Figure 4.7: χ-Squared statistic as a function of median particle size for the measured differential spectrum shown in Figure 4.6 and a log-normal distribution of particle sizes. We consider three different compositions, but the inferred particle sizes are relatively insensitive to composition. A horizontal dashed lined shows the 0.2% probability for a χ^2 distribution with 4 degrees of freedom, which corresponds to the likelihood of a 3σ event in a Normal distribution. The data favor large particle size distributions, but the significance varies on whether one adopts the propagated errors (*Top*) versus the scatter in the differential spectra *Bottom*.

200 Myr, suggesting KIC 12557548 is in the late catastrophic phase of planet disintegration (Perez-Becker & Chiang, 2013). On the other hand, the dust size distribution may shift to smaller particle radii for strong transit depths as suggested by (Bochinski et al., 2015). In this case, the lifetime could be closer to 1 Gyr if it returns to $\sim 0.1\mu$m particles for strong disintegration events. This would increase the likelihood of detecting disintegrating planets like KIC 12557548b,

KOI 2700b and EPIC 201637175b. Similarly, if the disintegration activity has decreased significantly since since 2009-2013 when the Kepler Observatory monitored KIC 12557548, then the total mass ejected into the comet-like tail per orbit is less than about 1/3 the average value implied by the Kepler Quarters 1-17. This would increase the lifetime of the planet and mean that the Kepler Observatory happened on a outburst of disintegration activity that is less than the average over long ($\gtrsim$ 10yr) timescales.

4.4 Conclusion

We observed the KIC 12557548 system for 8 transits using the SpeX spectrograph simultaneously with the MORIS imager in the r' photometry band. Our observations took place after the Kepler observatory stopped monitoring KIC 12557548, so we relied on MORIS for optical photometry while taking spectroscopy from 0.8μm to 2.4μm with SpeX. The r' photometric light curves have systematically smaller transit depths than the average value measured by the Kepler observatory. If we use the histogram from van Werkhoven et al. (2014), the probability of 8 independent transits having depths below 0.37% is 0.02%, indicating that the disintegration changed modes from when KIC 12557548 was observed by the Kepler observatory or that both in August/September of 2013 and 2014, our observations fell into particularly weak periods.

Our spectroscopic extractions using the SpeX instrument and differential spectroscopy show a flat spectrum across the wavelengths from 0.8μm to 2.4μm. The absolute time series were affected by systematics had had large variability in transit depth over the nights. This was unlike our previous observa-

tions of CoRoT-1b (Schlawin et al., 2014), which achieved sub-0.1% precision in transit depth across multiple wavelength channels. When we combine all of the differential spectra of KIC 12557548b over the nights with MORIS r' transit depths greater than 0.1%, we find that the transmission spectrum disfavors Mie scattering by small $\sim 0.1\mu$m olivine or pyroxene dust particles predicted by forward scattering models (Budaj, 2013; Brogi et al., 2012). It is likely that the dust particles we observed are larger in size ($\gtrsim 0.5\mu$m) for our epochs of observation. A similar large particle size is found by Croll et al. (2014a). Large dust particle sizes would result in short lifetimes of the planet, $\lesssim 10^7$yr (Perez-Becker & Chiang, 2013) if the dust particle size distribution we observed during weak transits is the same as during strong transits.

Continued monitoring in the visible will ascertain if the unusually weak disintegration activity observed in the r' band is an indication that the disintegration mechanism has changed or if it went through two weak periods during both August/September of 2013 and 2014. Additionally, the brighter recently discovered EPIC 201637175b system (Sanchis-Ojeda et al., 2015) presents another case to explore the transmission spectrum of a disintegrating planet. The EPIC 201637175 system's transit profile is more symmetric than KIC 12557548, indicating another geometry and potentially different particle size distributions for the escaping debris. Furthermore, long wavelength observations, such as with JWST will be useful for constraining the composition of the escaping debris and thus reveal the chemical makeup of these disintegrating bodies, a rare glimpse into the core of planets that have been peeled away layer by layer.

4.5 Acknowledgements

The authors wish to thank Bryce Croll and Saul Rappaport for their helpful suggested regarding observing. Thanks to James P. Lloyd for his advice on the interpretation of the spectra. Based on observations made from the Infrared Telescope Facility, which is operated by the University of Hawaii under contract NNH14CK55B with the National Aeronautics and Space Administration. M.Z. acknowledges support from NASA OSS grant NNX14AD22G and the Center for Exoplanets and Habitable Worlds at the Pennsylvania State University. The authors wish to recognize and acknowledge the very significant cultural role and reverence that the summit of Mauna Kea has always had within the indigenous Hawaiian community. We are most fortunate to have the opportunity to conduct observations from this mountain.

4.6 Appendix: Absolute SpeX Spectra

The individual transits of KIC 12557548 show dramatic night-to-night anomalies and variations in the SpeX infrared data, as visible in Figures 4.8 and 4.9. The system is intrinsically variable, as measured in high precision with the Kepler Observatory, although we expected that the variations among the 8 observed transits to be small because the MORIS photometry shows roughly 0.25% or below transit depths for all nights. If we assume that the near-infrared optical depth is proportional to the optical depth at $\sim 0.6\mu$m (as found tentatively with the Palomar H band data and by Croll et al. (2014a), then the variability observed in the SpeX spectrograph from 0.8μm to 2.4μm is likely due to systematic errors. Still, we consider the possibility that some of these variations are astrophysical. In this section, we fit the time series in the absolute sense instead of differentially (as done in Sections 4.3 and 4.3.2.)

The nights of August 15, 2013 and August 17, 2013 show deviation in the relative flux of the background near the two stars within the SpeX instrument corresponding to the time of the transit. These background fluctuations likely created anomalous bumps and troughs in the SpeX light curve, producing a strong positive transit and negative transit respectively. Given the background fluctuations, we only include the 6 remaining nights for absolute transmission spectrum analysis.

We adopt several methods of averaging both the individual spectra shown in Figure 4.9. When combining spectra obtained on different nights, we used weighted averaging with the weights proportional to $1/\sigma^2$, where σ is the error in transit depth propagated from the out-of-transit standard deviation. When

estimating the error of the average spectra, we also calculate the standard deviation of the mean using the scatter in the data as a conservative error estimate. Alternatively, one can combine the time series of multiple nights (shown in Figure 4.10 *Left*) and fit this combined time series. In the average time series method, errors are calculated from the standard deviation of the out-of-transit flux. The time series method results in a spectrum that rises from the optical r' band to the infrared, shown in Figure 4.10 (*Right*).

4.6.1 Alternate Chi-Squared Particle Size Constraints

For the average absolute spectra shown in Figure 4.10 we fit the data to Mie scattering models with log-normal size distributions of pyroxene grains, as done in Section 4.3.1. We show the constraints on particle sizes in Figure 4.11 for the 6 night time series average and for the average of the 6 nights with errors estimated from the scatter in the nights. In all cases, as with the differential spectra, the data favor large dust particle sizes, but the significance of the constraints changes depending on the method. In the former case, the models are not consistent with the data because the spectrum rises with wavelength and in the latter case, the particle size is weakly constrained to be above 0.1 μm. Using the scatter in the spectra (conservative case) gives the maximum error bars since it assumes no intrinsic astrophysical variability to the system. Continued monitoring of KIC 12575548b in both the infrared and optical will be invaluable in constraining the particle size and degree of variability.

Wavelength	Transit Depth (%)
0.63 (r')	0.16 ± 0.06
0.99	-0.21 ± 0.13
1.29	-0.09 ± 0.23
1.61	-0.14 ± 0.15
1.93	0.26 ± 0.26
2.24	0.84 ± 0.23

Table 4.2: Fitted transit depths for the control night of September 3, 2014, showing deviations from zero.

4.6.2 Transit Injection

As mentioned in Section 4.3.1, the control night of September 3, 2014 is fit as if it occurred during a transit to determine if there are systematics. The fitted transmission spectrum for this control night is not zero within errors, but the systematics are smaller than the large deviations occurring on August 15, 2013 and August 17, 2013. Table 4.2 shows that the individual transit fits for the control night vary by up to 3.7 σ, suggesting under-estimated errors in the absolute specta.

We perform another test of significance by injecting a transit into our control night of data, September 3, 2014. For this test, shown in Figure 4.12 left, we take the control night, which is out of transit and shift the orbital phase to fit a transit model as if it were real data during the transit. This control night shows deviations from zero that are not expected for Gaussian identically distributed independent errors, as listed in Table 4.2. Despite these variations, we demonstrate that at 1% deep transit would be recovered by the SpeX spectrograph and MORIS r' imager, shown in Figure 4.12 right.

4.7 Bootstrap Error Estimates

Another way to estimate errors in the transit depth from the light curve is by bootstrapping (e.g. Freedman, 1981). We resample the data with replacement so that the new time series is as long as the original. We find the best fit and repeat for 500 different re-samples of data of each time series. We then calculate a standard deviation of the fitted transit depths to find an uncertainty in the best-fit transit depth. The errors are close to the method described in Section 4.3.1 using a covariance matrix from `mpfit`, as visible for an example of a control night fit in Figure 4.13 (Left), though they are larger for long wavelengths. We also fit all differential transit depths with bootstrap errors and calculate the weighted average of the 5 nights with the strongest MORIS r' transits as done in Section 4.3. This weighted average differs slightly from the method using the `mpfit` covariance matrix by as much as 1.2σ, but the final result of the flat transmission spectrum (which favors large dust particle sizes $\gtrsim 0.5\mu$m) remains unchanged, visible in Figure 4.13 Right.

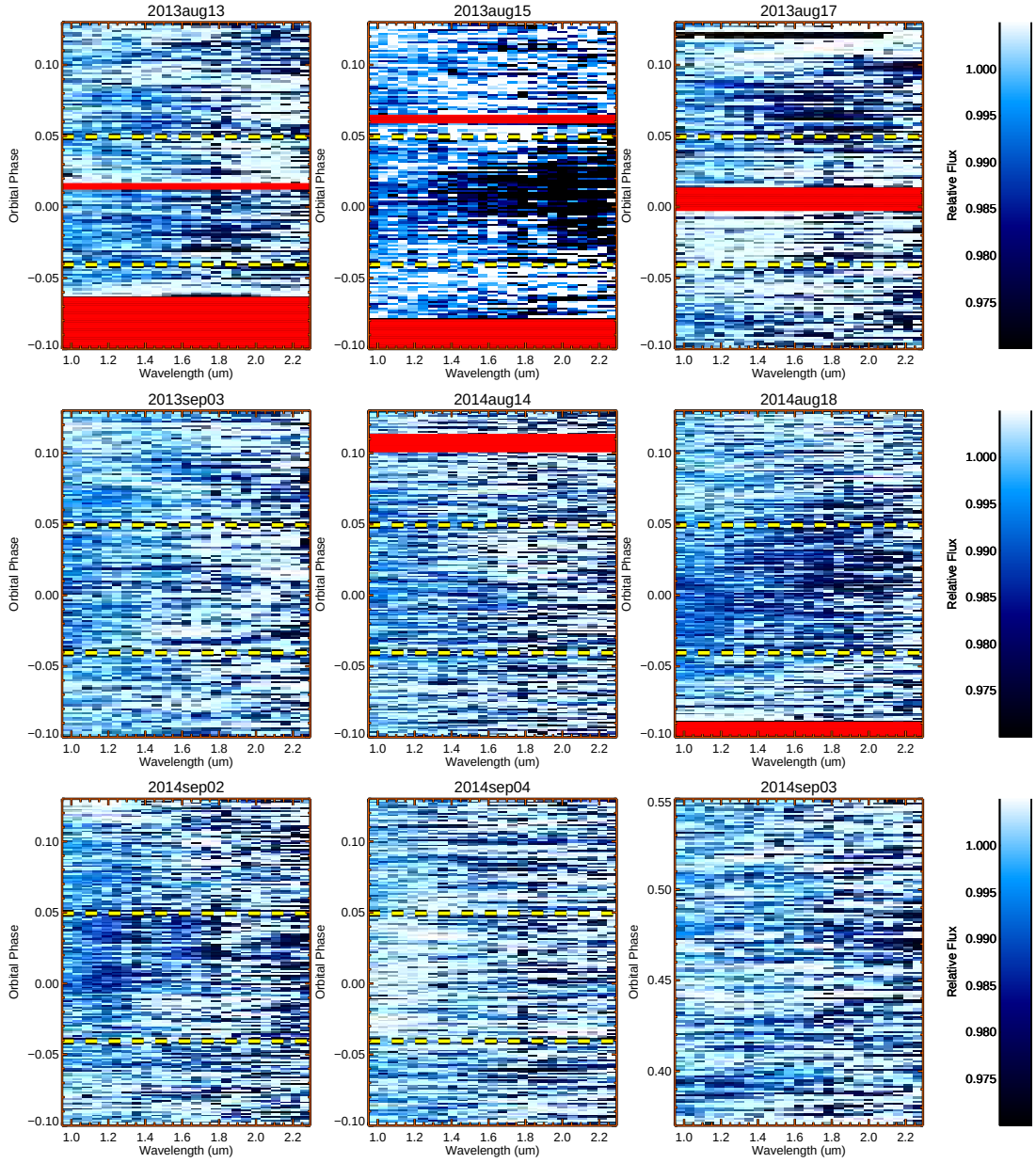

Figure 4.8: Dynamic spectrum for each of the nine partial nights of observation with the ingress and egress marked by dashed horizontal yellow lines, showing large systematic effects in the absolute time series. Missing data, marked in red, was due to daylight limits (August 13, 15, 2013), telescope guiding errors (August 13, 15, 17, 2013 and August 18, 2014) and human error (August 14, 2014). 8 of the observations took place during transit while September 3, 2014 was used as a control for understanding systematics.

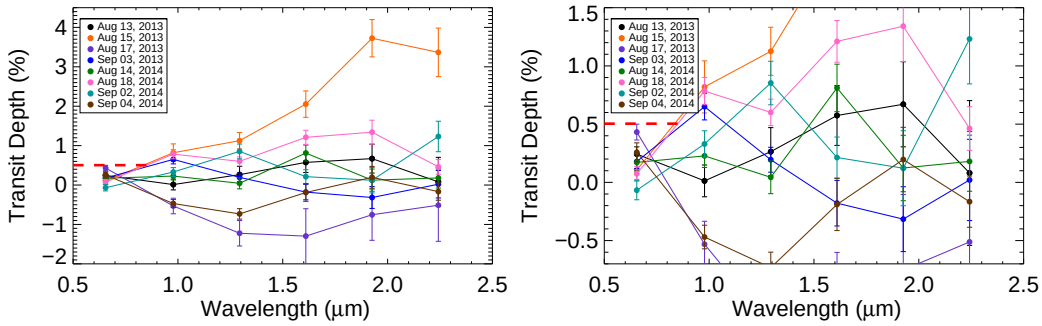

Figure 4.9: *Left* Transmission spectra for all 8 nights individually, showing large variations far above the error bars estimated from out-of-transit errors propagated to transit depth. In all plots, the horizontal dashed line is the average transit depth measured by the Kepler observatory. *Right* Same plot, but zooming in.

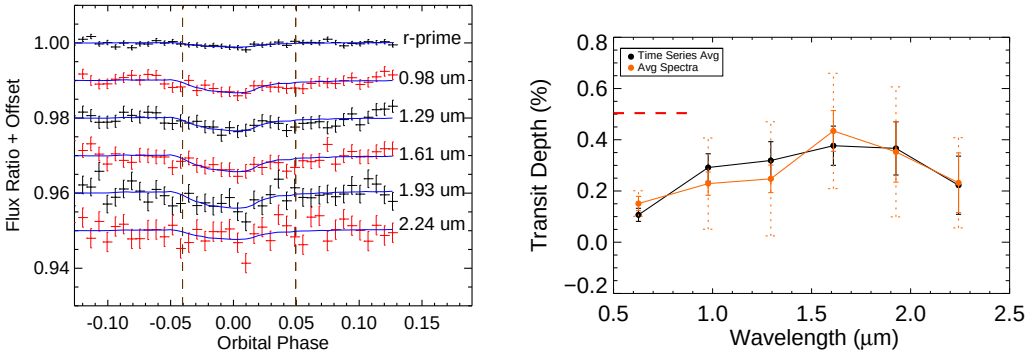

Figure 4.10: *Left* The average time series for all 6 of the 8 nights fit with the KSC curve by scaling the transit depth as a free parameter. We exclude the nights of August 15, 2013 and August 17, 2013, which were affected by background fluctuations. *Right* The fit to the average time series and alternatively the average of individual nights' spectra, show a rising spectrum from the optical to infrared, likely to to common-mode systematic errors.

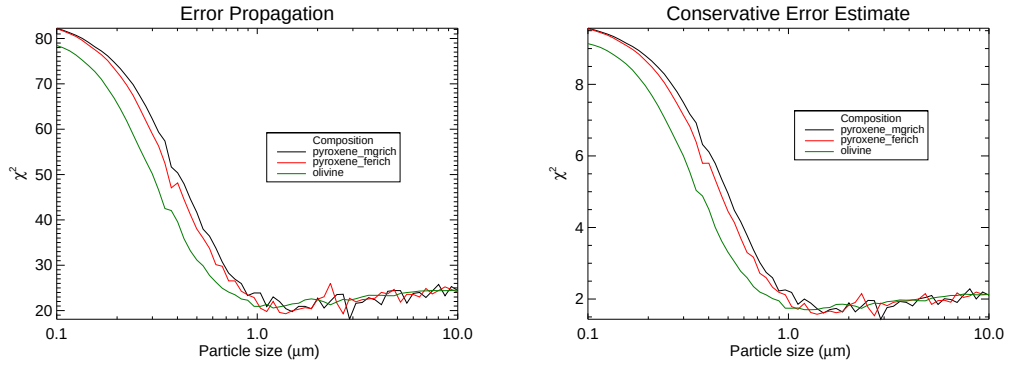

Figure 4.11: *Left* Chi-Squared statistic as a function of particle size for the measured 6 night time series average in Figure 4.10 and a log-normal distribution of particle size. The data favor large particle size models, but none can explain the the rise in transit depth with wavelength. *Right* Same statistic, but this time using a average of the 6 spectra and the scatter amongst the nights as a conservative error estimate. The particle size is only weakly constrained.

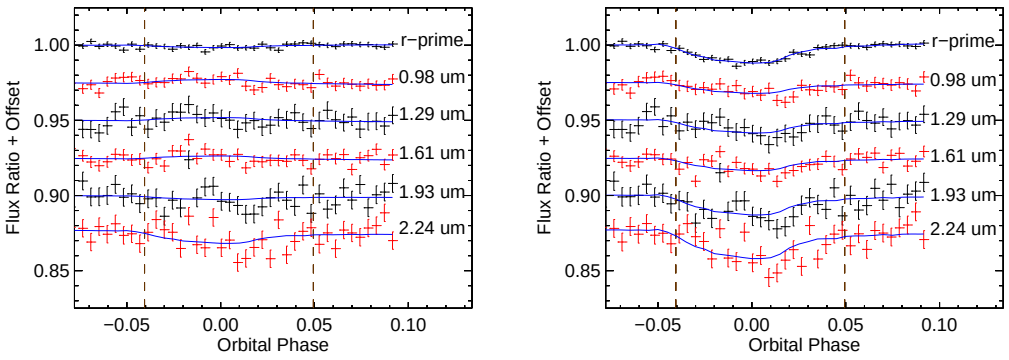

Figure 4.12: *Left* The control night of September 3, 2013 where the orbital phase has been shifted to estimate the errors in the fitting process. The control night is fit with the KSC light curve scaled to best fit the transit depth and does give deviations from the expected value of zero. *Right* If we artificially inject a 1% wavelength independent transit into the control night (a typical strong Kepler transit depth), it is recovered, though the fitted transit depths deviate from a flat spectrum.

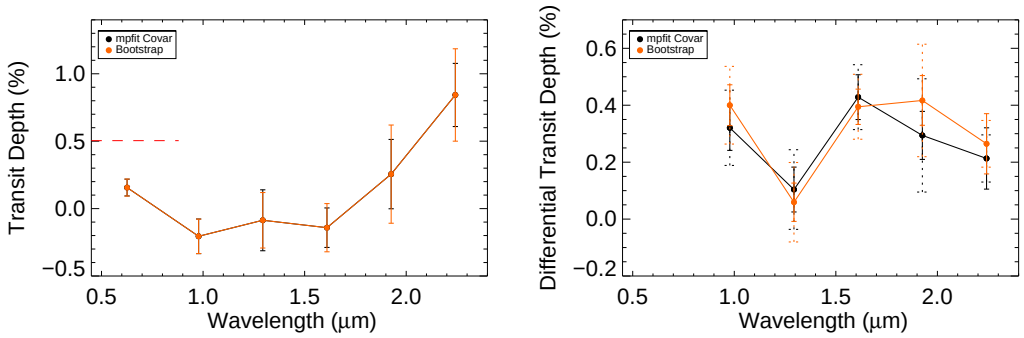

Figure 4.13: *Left* The spectrum of the control night of September 3, 2013 with two estimates for error bars. Bootstrap resampling gives comparable errors (though larger at long wavelengths) than propagating the out-of-transit standard deviation error estimates in the time series to the transit depth with a covariance matrix within `mpfit` *Right* The same two methods are used to estimate the uncertainty in transit depth for individual nights' differential transmission spectra. We combine the nights with weighted average and show that the final differential transmission spectrum is relatively unchanged, favoring large particles ($\gtrsim 0.5\mu$m) in the escaping winds from KIC 12557548b. As in the other plots, the dashed error bars are for errors estimated from the scatter in the individual nights' spectra.

BIBLIOGRAPHY

Bochinski, J. J., Haswell, C. A., Marsh, T. R., Dhillon, V. S., & Littlefair, S. P. 2015, ApJ, 800, L21, 1502.04612

Borucki, W. J. et al. 2010, Science, 327, 977

Brogi, M., Keller, C. U., de Juan Ovelar, M., Kenworthy, M. A., de Kok, R. J., Min, M., & Snellen, I. A. G. 2012, A&A , 545, L5, 1208.2988

Budaj, J. 2013, A&A , 557, A72, 1208.3693

Croll, B. et al. 2014a, ApJ, 786, 100, 1403.1879

Croll, B., Rappaport, S., & Levine, A. M. 2014b, ArXiv e-prints, 1410.4289

Crossfield, I. J. M., Hansen, B. M. S., & Barman, T. 2012a, ApJ, 746, 46, 1201.1023

Crossfield, I. J. M., Knutson, H., Fortney, J., Showman, A. P., Cowan, N. B., & Deming, D. 2012b, ApJ, 752, 81, 1202.1562

Dorschner, J., Begemann, B., Henning, T., Jaeger, C., & Mutschke, H. 1995, A&A , 300, 503

Draine, B. T. 2011, Physics of the Interstellar and Intergalactic Medium (Princeton University Press)

Freedman, D. A. 1981, Ann. Statist., 9, 1218

Gibson, N. P. et al. 2012, MNRAS , 422, 753, 1201.6573

Grainger, R. G., Lucas, J., Thomas, G. E., & Ewen, G. B. L. 2004, Appl. Opt., 43, 5386

Gulbis, A. A. S. et al. 2011, PASP , 123, 461, 1102.5248

Horne, K. 1986, PASP , 98, 609

Jura, M. 2003, ApJ, 584, L91, astro-ph/0301411

Kawahara, H., Hirano, T., Kurosaki, K., Ito, Y., & Ikoma, M. 2013, ApJ, 776, L6, 1308.1585

Koch, D. G. et al. 2010, ApJ, 713, L79, 1001.0268

Markwardt, C. B. 2009, in Astronomical Society of the Pacific Conference Series, Vol. 411, Astronomical Data Analysis Software and Systems XVIII, ed. D. A. Bohlender, D. Durand, & P. Dowler, 251, 0902.2850

Perez-Becker, D., & Chiang, E. 2013, MNRAS , 433, 2294, 1302.2147

Rappaport, S., Barclay, T., DeVore, J., Rowe, J., Sanchis-Ojeda, R., & Still, M. 2014, ApJ, 784, 40, 1312.2054

Rappaport, S. et al. 2012, ApJ, 752, 1, 1201.2662

Sanchis-Ojeda, R. et al. 2015, ArXiv e-prints, 1504.04379

Schlawin, E., Zhao, M., Teske, J. K., & Herter, T. 2014, ApJ, 783, 5, 1401.3337

Sing, D. K. et al. 2012, MNRAS , 426, 1663, 1208.4982

Skrutskie, M. F. et al. 2006, AJ, 131, 1163

Southworth, J. et al. 2009, MNRAS , 396, 1023, 0903.2139

van Lieshout, R., Min, M., & Dominik, C. 2014, A&A , 572, A76, 1410.3494

van Werkhoven, T. I. M., Brogi, M., Snellen, I. A. G., & Keller, C. U. 2014, A&A , 561, A3, 1311.5688

Vidal-Madjar, A., Lecavelier des Etangs, A., Désert, J.-M., Ballester, G. E., Ferlet, R., Hébrard, G., & Mayor, M. 2003, Nature , 422, 143

Wilson, J. C. et al. 2003, in Society of Photo-Optical Instrumentation Engineers (SPIE) Conference Series, Vol. 4841, Instrument Design and Performance for Optical/Infrared Ground-based Telescopes, ed. M. Iye & A. F. M. Moorwood, 451–458

Zhao, M., Monnier, J. D., Swain, M. R., Barman, T., & Hinkley, S. 2012, ApJ, 744, 122, 1109.5179

Zhao, M. et al. 2014, ApJ, 796, 115, 1410.0968

This Chapter submitted to the Astrophysical Journal as (Schlawin, Herter, Zhao, Teske and Chen, 2015)

CHAPTER 5

CONCLUSION

5.1 Hot Jupiter Transmission Spectroscopy

An important consideration when observing exoplanet transits, especially in low signal to noise cases, is to know the limb darkening and brightening of its host star. For most broadband wavelengths observed in the optical through infrared, the stellar surface is limb darkening because of the temperature structure of its atmosphere. Ultraviolet observations, on the other hand, come from the chromosphere, where the surface is optically thin. We calculate the limb brightening effect, discussed in Schlawin et al. (2010), which has the bonus of increasing the transit depth for a fixed planet size. We evaluate the limb brightened light curve for archival Hubble Space Telescope Imaging Spectrograph (STIS) data on the exoplanet HD 209458b to determine if Si IV is absorbed in the planet's atmosphere. We find tentative absorption from HD 209458b's winds. Additional observations with Cosmic Origins Spectrograph (COS) indicate that Si IV absorption is small mid-transit, but followup at the stellar limb will be critical to determining if this highly ionized Silicon is present in hot Jupiter winds.

We have observed the near infrared transmission spectrum of the hot Jupiter CoRoT-1b in order to constrain the composition of its atmosphere, discussed in Schlawin et al. (2014). Over the wavelengths we measure from 0.8μm to 2.4μm we have no statistical significant detections of molecules. The null detection is useful, however for diagnosing the composition and temperature structure of the planet. The molecules TiO and VO were hypothesized to be in hot Jupiter atmospheres like CoRoT-1b and their high ultraviolet and optical opacity can

absorb energy at high altitudes to create an inverted temperature profile. Previous predictions from CoRoT-1b's emission spectrum of the planet favored an inverted or isothermal profile (Rogers et al., 2009; Gillon et al., 2009; Zhao et al., 2012). We find no evidence for TiO or VO molecules when combining our measured spectrum with a space-based CoRoT-1b optical radius, suggesting that the atmosphere has a temperature inversion due to other molecules like sulfur-containing compounds or that a haze/dust layer obscures the molecular features both in transmission and emission and produce a black-body like emission spectrum (Deming et al., 2011).

5.2 The Disintegrating Planet, KIC 12557548

The same observational instrument, telescope and technique used to achieve 300ppm to 900ppm precision for CoRoT-1 opened the door to studying the fascinating disintegrating planet candidate KIC 12557548b. This system did, however, present new observing challenges due to its intrinsic variability and faintness. We observed 8 transits to improve the measurement precision of the system. Previous estimates of the particle size distribution from the planetary debris' forward scattering pointed to particle sizes of ~0.1μm (Brogi et al., 2012; Budaj, 2013). These small particle sizes would produce a very large disparity between the optical and infrared transit depths. Unlike hot Jupiters which have tiny atmospheric signatures (~.04%) on top of their top of their (~ 1%) transit depths, KIC 12557548 is essentially all atmosphere (~0.5% to 1% transit depth) with almost no planet ($\lesssim$ 0.05% transit depth) so it should have much larger wavelength dependence to its transit depth. We found the opposite from our predictions, which is that the infrared transmission is just as large as the optical

transit depths. Our large infrared opacity suggests that the debris particles must be $\gtrsim 0.5\mu$m. The consequence of large particles is that KIC 12557548b must have a vigorous mass loss rate, and could be destroyed entirely in less than 10^7 yr and is the final stages of its destruction. More will be learned about these exoplanets with the followup of nearer disintegrating systems such as EPIC 201637175b (Sanchis-Ojeda et al., 2015).

BIBLIOGRAPHY

Brogi, M., Keller, C. U., de Juan Ovelar, M., Kenworthy, M. A., de Kok, R. J., Min, M., & Snellen, I. A. G. 2012, A&A , 545, L5, 1208.2988

Budaj, J. 2013, A&A , 557, A72, 1208.3693

Deming, D. et al. 2011, ApJ, 726, 95, 1011.1019

Gillon, M. et al. 2009, A&A , 506, 359, 0905.4571

Rogers, J. C., Apai, D., López-Morales, M., Sing, D. K., & Burrows, A. 2009, ApJ, 707, 1707, 0910.1257

Sanchis-Ojeda, R. et al. 2015, ArXiv e-prints, 1504.04379

Schlawin, E., Agol, E., Walkowicz, L. M., Covey, K., & Lloyd, J. P. 2010, ApJ, 722, L75, 1008.1073

Schlawin, E., Zhao, M., Teske, J. K., & Herter, T. 2014, ApJ, 783, 5, 1401.3337

Zhao, M., Monnier, J. D., Swain, M. R., Barman, T., & Hinkley, S. 2012, ApJ, 744, 122, 1109.5179

APPENDIX A

DESIGN UPDATES AND STATUS OF THE FOURTH GENERATION TRIPLESPEC SPECTROGRAPH [1]

A.0.1 Abstract

TripleSpec 4 (TS4) is a near-infrared (0.8um to 2.45um) moderate resolution (R ~ 3200) cross-dispersed spectrograph for the 4m Blanco Telescope that simultaneously measures the Y, J, H and K bands for objects reimaged within its slit. TS4 is being built by Cornell University and National Optical Astronomy Observatory (NOAO) with scheduled commissioning in 2015. TS4 is a near replica of the previous TripleSpec designs for Apache Point Observatory's ARC 3.5m, Palomar 5m and Keck 10m telescopes, but includes adjustments and improvements to the slit, fore-optics, coatings and the detector. We discuss the changes to the TripleSpec design as well as the fabrication status and expected sensitivity of TS4.

A.1 INTRODUCTION

Medium resolution infrared spectrographs are invaluable instruments for characterizing asteroids, high red shift galaxies, cool stars and brown dwarfs. The TripleSpec design uses a grating (operating in multiple orders) with a cross-dispersing prism so that the Y, J, H and K bands can be measured simultaneously covering the wavelengths from 0.8μm to 2.4μm. This versatile approach

[1] THIS CHAPTER IS PUBLISHED AS Schlawin et al. (2014)

is easy to replicate (Wilson et al., 2004) and is now employed on the Palomar 5-m (Herter et al., 2008), Apache Point Observatory (APO) 3.5-m[2] telescopes and will soon be commissioned on the Keck[3] 10-m telescopes. The Fourth generation TripleSpec (TS4) will be a NOAO facility instrument on the Victor M. Blanco Telescope at Cerro Tololo Inter-American Observatory (CTIO) in Chile.

A.1.1 TripleSpec Science

The Palomar TripleSpec, in service since 2008, has been used for a variety of science applications. For instance, it was successfully used to measure stellar metallicities (stellar abundances of heavy elements) in cool (3000K to 4250 K) stars (Rojas-Ayala et al., 2010, 2012). The Ca I doublet and Ka I triplet equivalent widths and water vapor features (2.07-2.09μm, 2.235-2.255μm and 2.36-2.380μm) (Covey et al., 2010) present in M dwarf stars correlate with their metallicity as measured by iron ([Fe/H]) and with effective temperature. These stellar features are all simultaneously accessible with the TripleSpec spectrograph and were calibrated against known standards to create a metallicity indicator accurate to within 0.14 dex (Rojas-Ayala et al., 2012). Since the method was calibrated on TripleSpec, a clone of the same spectrograph on a telescope in the Southern hemisphere will allow for reliable estimates of M dwarf metallicities with minimal systematic differences in data sets.

Using similar methods, an observation campaign with the Palomar TripleSpec was conducted to characterize the stellar abundances, radii and effective temperatures of the Kepler field's cool ($T_{\rm eff}$ < 4400 K) planet-hosting stars

[2]PI John Wilson
[3]PI Keith Matthews

(Muirhead et al., 2012). High precision Kepler time series of transiting candidates gives the planet properties in terms of stellar radius, so improving the stellar properties over photometric colors with TripleSpec in turn improves the measured parameters of the planets that orbit them. A giant star was identified in this campaign, helping distinguish real planets from false positives.

In addition to cool star science, the TripleSpec instruments have been used to characterize objects from near-earth asteroids to high redshift quasars. When the asteroid 2005 YU55 passed within the orbital radius of the Moon, Palomar TripleSpec spectra were used to constrain its thermal emission and compositional class (Moskovitz et al., 2012). Followup spectroscopy of a brown dwarf discovered in the ξ Ursa Majoris system with a Palomar TripleSpec spectrum revealed it is an ultra cool T8.5 class from the strength of its water vapor and methane features (Wright et al., 2013). For extragalactic science, TripleSpec instruments are sensitive to rest-frame optical and ultraviolet emission from quasars including the Balmer Hydrogen and C IV lines, which were used on the APO TripleSpec to estimate black hole masses in high redshift lensed systems (Greene et al., 2010).

A.2 Summary of the TripleSpec Design

The TripleSpec design covers the wavelengths from ~0.8μm to 2.45μm simultaneously at a spectral resolution of R ~3200. This is accomplished with a prism that cross-disperses the light from a grating, separating the multiple orders and allowing for simultaneous measurement of this wide wavelength regime without the need to adjust any internal changeable mechanisms – see Figure

A.1. Two off axis parabolas (OAPs) convert the telescope's input beam (F/8 at Blanco to F/16 at Palomar) to f/10.7 at the slit substrate, allowing identical downstream spectrograph optics on all telescopes. Grating orders 3 through 7 are imaged onto a 2048x1024 region of a near infrared array. Separately, the slit viewing optics (Figure A.2) image a 4′ × 4′ field surrounding the slit for orienting and aligning the slit and also guiding the telescope on a 1024x1024 near infrared array.

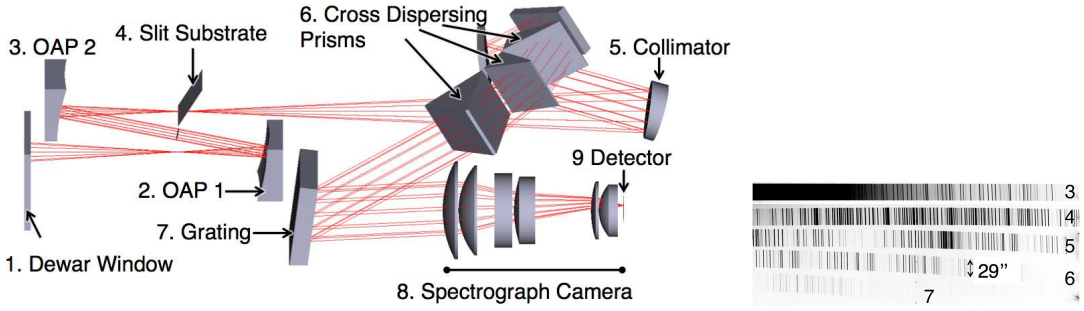

Figure A.1: *Left* TripleSpec spectrograph ray trace. Light enters the dewar window and is converted to a f/10.7 beam by two off axis parabolas OAPs. The slit substrate permits a 1×29″ region to enter the spectrograph and reflects the rest of the field to the slit viewing optics (Figure A.2). The rest of the optics are the same for all four TripleSpec designs. After reflecting off a collimator and fold mirrors, the beam passes through three cross-dispersing prisms that separate the orders of the diffraction pattern. A grating disperses the light to a resolution $R \sim 3200$ spectrum which is focused on the detector with a seven element camera (the fourth optic after the grating is actually two close lenses). *Right* A schematic of sky background emission focused on the detector for wavelengths from 0.8μm to 2.45μm with each of grating orders labeled. Blanco's nominal 28.7″ slit length is described in Section A.3.1.

An outer clamshell and 120 liter crescent shaped liquid nitrogen tank shown in Figure A.3 cools the optics to <80K to reduce the thermal background. A two liter internal auxiliary tank (not shown) further maintains the detector's tem-

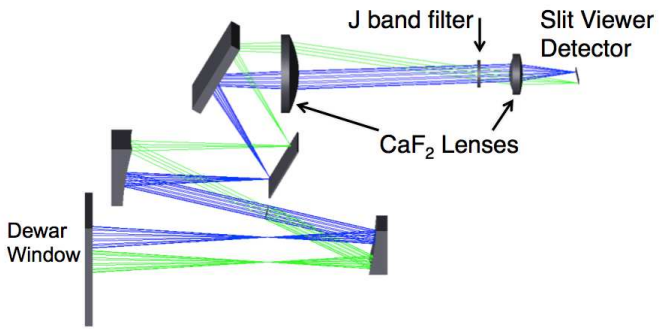

Figure A.2: TripleSpec slit viewer layout. A 4′ by 4′ field containing the 1×29″ slit) is reflected by the slit substrate and focused by the slit viewing optics. The slit viewer allows telescope users to align and orient the slit on astronomical sources and reference stars. Unlike previous K_S band guiders on the TripleSpec instruments, TS4 will operate in the J band to minimize thermal instruments, TS4 will operate in the J band to minimize thermal background. The optics illuminate a 1024×1024 section of a Hawaii-II RG engineering grade detector. "Full frame" and windowing modes (for rapid readout) are both available.

perature without active thermal control. The main tank is half filled and the tank fill and exhaust piping is positioned so that there is no spillage at any dewar + telescope orientation and the dewar will keep cold without refilling for more than 3 days. Three parallel inner bulkheads maintain a rigid reference for optical components in a variety of orientations. The Blanco design will have a single slit option and thus no moving parts for long-lasting and stable performance. The cold volume containing all optical components and crescent tank is suspended from the outer vacuum vessel by fiberglass S2 radial straps and G10 axial plates to minimize thermal conduction to the room temperature exterior.

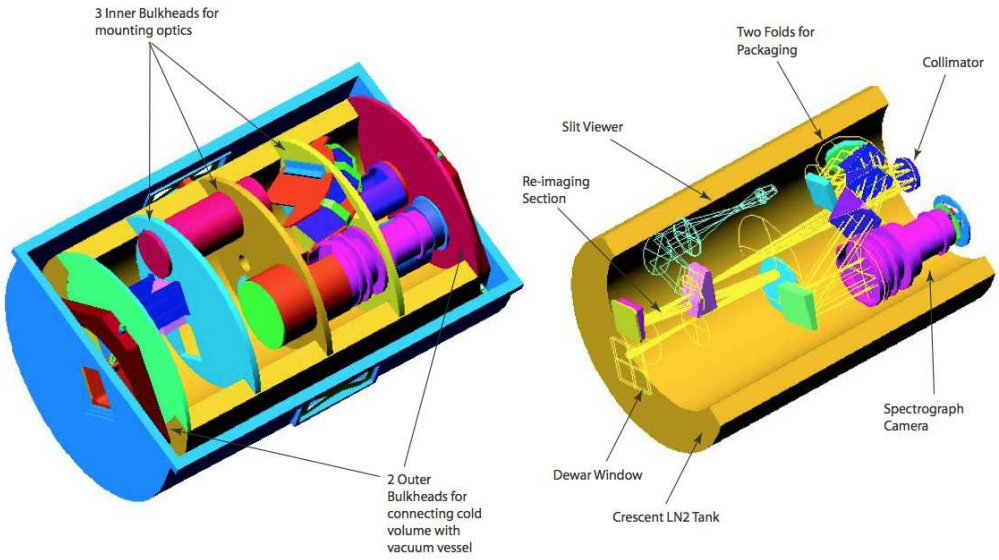

Figure A.3: Cryogenic dewar design (Wilson et al., 2004). A crescent shaped region of the dewar holds the liquid nitrogen cryogen with an expected hold time of over 3 days. Three internal parallel bulkheads serve as optical mounting platforms for the lenses, reflectors, grating and detector that also maintain a rigid structure for a variety of orientations.

A.3 Updates and Changes from Previous TripleSpec Designs

All TripleSpec instruments must include adjustments to fore-optics and slit viewer to accommodate the telescope's f/#. TS4 will be mounted at the 4m Blanco telescope's f/8 Ritchey-Chretién focus. A Lyot mask is placed at the image of the primary mask formed by the first OAP to minimize the thermal emission from the telescope supports and central obscuration (which is set by the DECam instrument). Additionally, we will be adding some new features to the slit substrate, improving the short wavelength performance of the optical coatings and changing the slit viewer to J band.

A.3.1 Slit Substrate Changes

The TripleSpec spectrograph will contain a cold slit that accepts a small area of the sky for spatially isolating a science target, minimizing the amount of background radiation and increasing the spectrograph's resolution. The rest of the 4'×4' field is reflected to the slit viewing optics, shown in Figure A.2. As with the Palomar and APO TripleSpec instruments, TS4 will have an etched silicon wafer coated with a gold that results in a very low surface roughness surface ($<$ 2nm) (Vandervelde et al., 2006). The slit substrate, fabricated by Michael Cabral (Virginia Commonwealth University), is produced by wet etching the substrate from the front and rear surface and removing the remaining silicon with a dry etch.

A nominal slit width of 1.1" was chosen as an optimal trade off between high spectral resolution and high slit throughput. Wide slits have higher through-

put and thus increase the instrument's sensitivity but have lower resolution. Narrow slits have lower throughput but their higher resolution improves radial velocity precision and resolves individual telluric (Earth's atmospheric) airglow lines for easier background subtraction. For the seeing conditions at CTIO (with a median of 0.9" Full Width at Half Maximum (FWHM) and the science needs of the spectrograph, 1.1" is the optimal width.

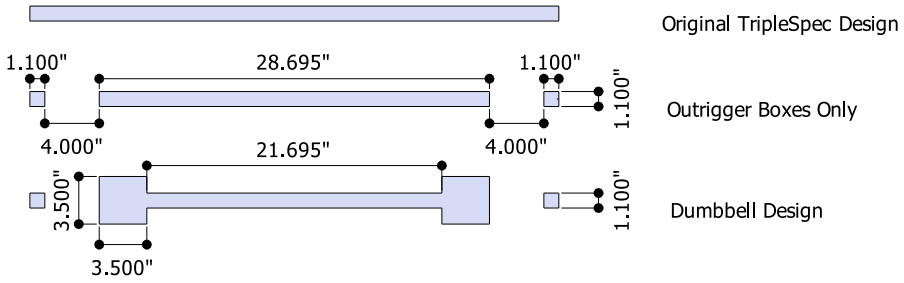

Figure A.4: Previous slit design compared with two different slits being fabricated for TS4. The silicon slit substrate (pictured in Figures A.1 and A.2) accepts a small region to the spectrograph and reflects the rest of the 4' ×4' field to the slit viewer. TS4 will have 1.1" × 1.1" outrigger boxes for easy identification of airglow OH lines, which are used for wavelength calibration. Additionally, a "Dumbbell" option includes two 3.5"×3.5" boxes for high throughput, lower resolution observations of exoplanets and asteroids. One of the two slit options shown here will be chosen after testing.

Previous slit designs were rectangular in shape, seen in Figure A.4, but TS4 will have added features. Two outrigger boxes are placed on the ends of the slit which will make square-like sources of the telluric OH airglow lines on the detector for easy identification and location. These airglow lines can be used for wavelength calibration and tracing the spatial and spectral directions on the spectrograph.

In addition to the outrigger boxes, we will be testing a "dumbbell" slit op-

tion. The dumbbell slit contains two boxes 3.5″ each towards the ends of the slit. Point sources such as exoplanets and asteroids placed in these boxes will have minimal slit losses, but with lower resolution spectra. The large slit widths within the boxes reduce the spectral slopes created by differential slit loss, such as caused by the variation of stellar FWHM with wavelength due to seeing and position due to refraction. Two boxes are used to enable sky subtraction when nodding the 25.2″ distance between the box centers. The remaining 21.7″ portion of the slit can be used in the conventional TripleSpec observing mode with sufficient spatial room remaining to nod point sources or extended sources along the slit and obtain higher resolution $R \sim 3200$ spectra. In all, four orthogonal slits are cut into the substrate, with the final choice selected by the orientation of the substrate. The three unused slits are outside the 4′×4′ field of view so they do not appear on the slit viewer detector.

A.3.2 Improved Coatings

The Palomar and APO TripleSpec instruments had about half the expected transmission for wavelengths 1.0μm and shorter because the coatings' short wavelength cutoff was mistakenly specified to be 1.0 μm. As seen in Figure A.5 *Top*, the ZnSe prism transmission drops off sharply at these wavelengths. The new ZnSe TS4 coating shown in Figure A.5 *Bottom* has less than 1.5% reflectance across the entire 0.8μm to 2.45μm wavelength range. The new coatings are expected to improve the short wavelength sensitivity of TS4 because they are correctly extended to 0.8μm.

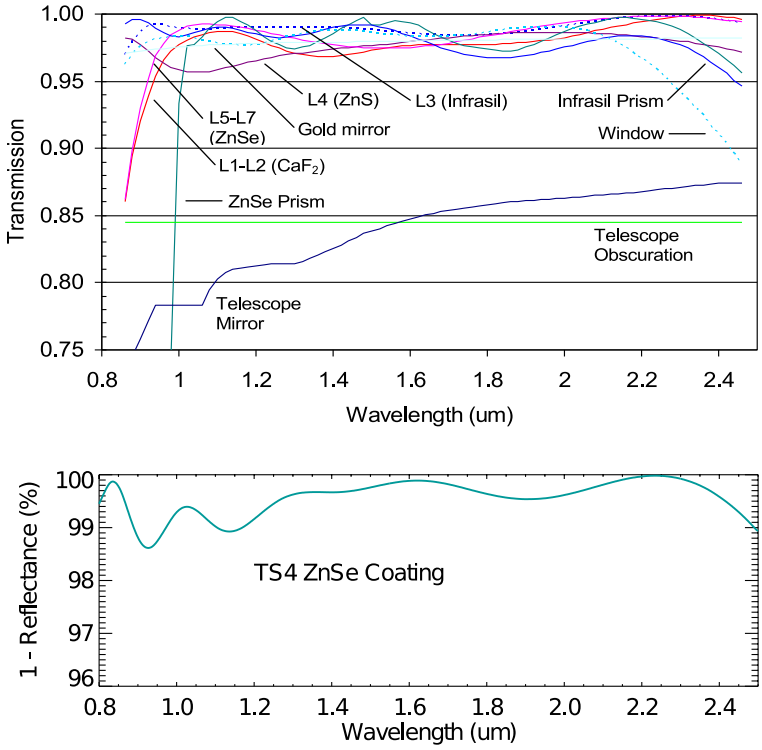

Figure A.5: *Top* Transmission of various components of the Palomar TripleSpec system suggests that the ZnSe prism coatings may be responsible for the lower than expected sensitivity at short wavelengths. *Bottom* Reflectance for the new coatings from II-IV, which may improve the overall short wavelength performance.

A.3.3 J Band Slit Viewer

TS4 will have a J band slit viewer for imaging the field and aligning a science target on the spectrograph slit. The *J* band slit viewer will have lower thermal backgrounds than the APO and Palomar K_S band imagers, which require sky subtraction for all but the brightest guide stars. As with the Palomar TripleSpec, an imaging solution was found with two aspherical lenses, shown in Figure A.2.[4] Due to their gradual slope of index of refraction as a function of wave-

[4]The slit viewer must be modified for each telescope (despite working to the same f/#) because, in part, off-axis aberrations introduced by reimaging optics are corrected by having a

length across the J band, CaF_2 lenses were found to have the best performance. The smaller downstream surface has two curved surfaces and was constructed with a flat ring surrounding the clear aperture on the upstream surface for simpler mounting. The ray-traced spot size FWHM of 0.48″ is well below the median CTIO seeing of 0.9″. The filter's transmission is above 50% from 1.17μm to 1.33μm.

A.3.4 Detector Upgrade

Previous TripleSpec instruments had Hawaii I and Hawaii II Teledyne arrays which will be replaced in TS4 by Hawaii-II RG HgCdTe arrays, also from Teledyne. The Hawaii-II RG detectors have reference columns, which allow one to subtract and reject common-mode noise sources. The substrate-removed HgCdTe sensors also have enhanced J-band quantum efficiency. The array mounts and cabling were re-designed to accommodate the new arrays, but their mounting schemes are similar.

The slit viewer detector is an engineering-grade array for the purposes of aligning and orienting the slit and guiding. Only a 1024×1024 portion of the 2048×2048 array will be read out for a field size of 907× 926 pixels. A 1024×2048 portion of the spectrograph detector (science-grade) will be used for science exposures.

Both the slit viewer and spectrograph arrays will be read out with the current generation Leach controllers. The user interface will be written in ArcVIEW for commonality with other CTIO instruments. The slit viewer array will have

translational offset of the beam entering the first lens.

the option to read out a small sub-array window at a faster cadence (a few Hz frame rates) for guiding or monitoring of the sources on the spectrograph slit while simultaneously acquiring data on the full array. The fastest expected full frame rate for the guider will be ~1Hz. The slow read out mode is selected over the fast mode to minimize read noise, which is important for faint astronomical sources.

Initial tests of the slit engineering grade viewer detector indicate performance within manufacturer specifications. The read noise for correlated double sampling was 14e^-/px with a noise floor of 4.5e^-/px for Fowler 16 sampling. Inter-pixel capacitance was measured to be ~3% and 95% of the pixels are linear to within 5% up to counts of 90,000 e^-. The spatial and temporal gain were analyzed independently and converge on a value of ~1.8 e^-/ADU (analog digital unit). The science grade detector for the spectrograph is expected to have better performance.

A.4 Status and Expected Performance

TS4 is scheduled for commissioning during the first half of 2015. The arrays have passed initial tests, all major optical components are in hand for assembly in the dewar. Main items to be completed are the integration of components, alignment and testing. Previous TripleSpec experience has expedited the design, purchase orders and fabrication of the instrument. The detector electronics testing and optimization is being performed at CTIO. The optical and cryo-mechanical fabrication is occurring at Cornell and The University of Virginia with instrument integration and lab testing at Cornell.

A.4.1 Expected Sensitivity

Figure 6 shows the expected fluxes for 4 pixel long detector columns (1×4 pixel regions) as a function of wavelength for TS4. Since TS4 is a near-replica of previous designs, its sensitivity can be estimated by scaling the measured fluxes at Palomar by the relative collecting areas of Blanco and Palomar. The Blanco's collecting area is reduced by the Lyot stop central obscuration to account for the outer diameter of the DECAM instrument rotated 360° to allow for all orientations of TripleSpec.

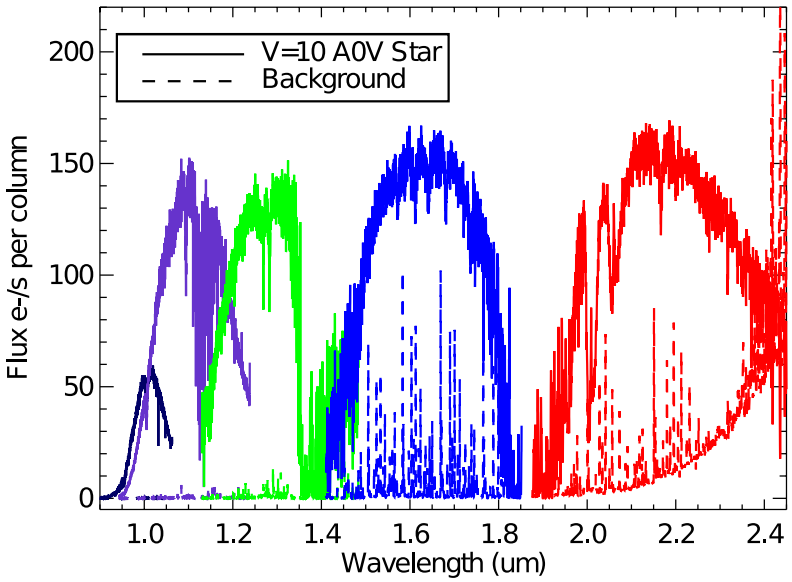

Figure A.6: The estimated background and source fluxes for an A0V star by scaling the performance at Palomar by the fractional collecting area at the Blanco telescope. Grating order 3 through 7 are color-coded to illustrate the wavelength coverage and overlap.

For targets with a magnitude m, the signal to noise ratio per column is:

$$\frac{S}{N} = \frac{10^{-\frac{2}{5}(m-10)} F_\nu t}{\sqrt{10^{-\frac{2}{5}(m-10)} F_\nu t + b_\nu \frac{N_{\rm pix}}{4} t + N_{\rm pix} R^2 N_{\rm coadds}}} \tag{A.1}$$

where m is the a target's Vega magnitude in a given band, F_ν is the reference A0 V star flux in Figure A.6 in e^-/s, t is the combined integration time of all frames in seconds, b_ν is the background emission as a function of wavelength in Figure A.6 in e^-/s, N_{pix} is the number of pixels extracted and $R \approx 4.5\ e^-$ is the read noise per pixel and N_{coadds} is the number of coadded frames.

Figure A.7 shows the expected signal to noise ratio per column for a 17th magnitude A0V point source observed by TS4. 12 coadds (such as would be observed in three ABBA nod sequences) of 5 minute exposures achieve a S/N ratio per column from 3 to 18 for most of the wavelength coverage. The S/N can be further increased by $\sim \sqrt{3}$ by combining the $\sim$ 3 pixels per resolution element.

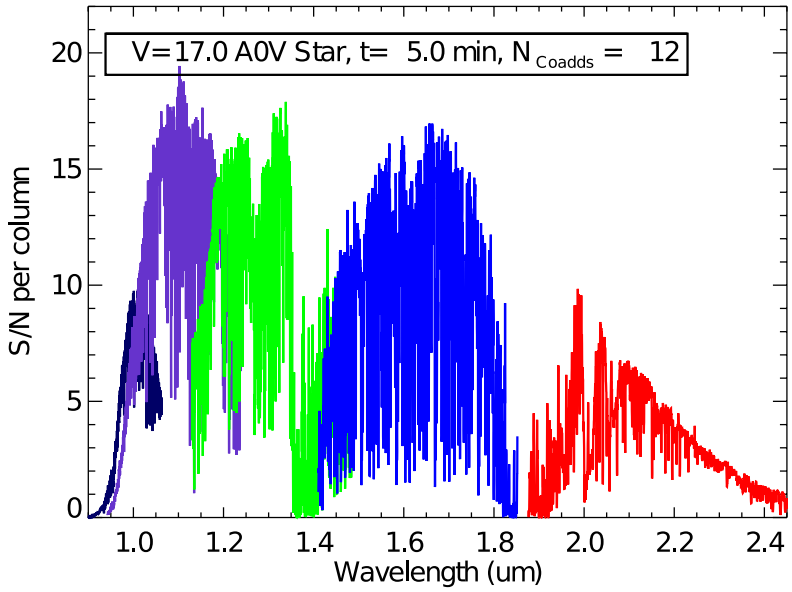

Figure A.7: The estimated S/N for an A0V-type source with a Vega visual magnitude of 17. Each column in this case is a 1×4 pixel region of the detector array. Grating order 3 through 7 are color-coded to illustrate the wavelength coverage and overlap.

Spectrograph	
Wavelength coverage	0.8-2.4μm
Resolution	$\sim$ 3200
Plate Scale	0.36″/px (20″/mm)
Slit Size	1.1″ × 29.7″[a]
Detector	Science Hawaii-II RG, 1024×2048 used

Slit Viewer	
Slit Viewer Band	J 1.17μm to 1.33 μm
Spot FWHM without seeing	0.48″
Plate Scale	0.27″/px (15″/mm)
Slit Viewer FOV	4′ × 4′
Detector	Engineering Hawaii-II RG, 1024×1024 used
Read Noise	4.5e$^-$ for Fowler 16 sampling

Table A.1: Summary of the expected properties for TS4.*a* The slit length may include two larger 3.5″×3.5″ boxes shown in Figure A.4.

A.5 Conclusions

TS4 is the 4th of a line of "mass produced" medium resolution $R \sim 3200$ spectrographs. These spectrographs are valuable tools to characterize high redshift galaxies, cool stars, brown dwarfs and asteroids. TS4 is a near clone of previous TripleSpec instruments on Palomar, APO and Keck but with some additional improvements. As compared to previous designs, it will have a slit that is easier to calibrate and may include lower slit losses, new coatings to improve the short wavelength performance, a J band slit viewer optimized for Blanco and a detector upgrade to a Hawaii-II RG. TS4's expected properties are summarized in Table A.1.

BIBLIOGRAPHY

Covey, K. R., Lada, C. J., Román-Zúñiga, C., Muench, A. A., Forbrich, J., & Ascenso, J. 2010, ApJ, 722, 971, 1007.2192

Greene, J. E., Peng, C. Y., & Ludwig, R. R. 2010, ApJ, 709, 937, 0911.0685

Herter, T. L. et al. 2008, in Society of Photo-Optical Instrumentation Engineers (SPIE) Conference Series, Vol. 7014, Society of Photo-Optical Instrumentation Engineers (SPIE) Conference Series

Moskovitz, N. A., Yang, B., Lim, L. F., Emery, J. P., Granvik, M., Sheppard, S. S., Willman, M., & McMillan, M. 2012, in Lunar and Planetary Inst. Technical Report, Vol. 43, Lunar and Planetary Science Conference, 2080

Muirhead, P. S., Hamren, K., Schlawin, E., Rojas-Ayala, B., Covey, K. R., & Lloyd, J. P. 2012, ApJ, 750, L37, 1109.1819

Rojas-Ayala, B., Covey, K. R., Muirhead, P. S., & Lloyd, J. P. 2010, ApJ, 720, L113, 1007.4593

——. 2012, ApJ, 748, 93, 1112.4567

Schlawin, E. et al. 2014, in SPIE Conf Series, Vol. 9147, SPIE Conf Series, 2

Vandervelde, T. E., Cabral, M. J., Wilson, J., & Skrutskie, M. 2006, in Society of Photo-Optical Instrumentation Engineers (SPIE) Conference Series, Vol. 6273, Society of Photo-Optical Instrumentation Engineers (SPIE) Conference Series

Wilson, J. C. et al. 2004, in Society of Photo-Optical Instrumentation Engineers (SPIE) Conference Series, Vol. 5492, Ground-based Instrumentation for Astronomy, ed. A. F. M. Moorwood & M. Iye, 1295–1305

Wright, E. L. et al. 2013, AJ, 145, 84, 1203.5764

GLOSSARY

amu atomic mass unit.]page4

APO Apache Point Observatory.]page117,]page122,]page130

COS Cosmic Origins Spectrograph.]page35,]page112

CTIO Cerro Tololo Inter-American Observatory.]page117,]page123,]page126, 127

DN Data numbers.]page15

FWHM Full Width at Half Maximum.]page9,]page11, 12,]page123, 124,]page126,]page130

IRTF Infrared Telescope Facility.]pagev,]page8, 9,]page12,]page15, 16

MOS Multi-Object Spectroscopy.]page13,]page40,]page44, 45,]page67

NOAO National Optical Astronomy Observatory.]page116

OAP off axis parabola.]page119,]page122

primary transit when a planet goes in front of its host star, scattering and absorbing light.]page2

PSF Point Spread Function.]page6–9,]page12,]page15, 16

secondary eclipse when a planet goes behind its host star.]page2

STIS Hubble Space Telescope Imaging Spectrograph.]page31, 32,]page112

telluric due to Earth's atmosphere, usually meaning the absorption due to gases such as water vapor that attenuate the flux of astronomical sources.]page12, 13

TS4 TripleSpec 4.]page116, 117,]page120,]page122–130